Analyzing the Stability and Kinetics of Ceramic Electrolyte/Organic Electrolyte Interfaces for Li Metal Batteries

by

Arushi Gupta

A dissertation submitted in partial fulfillment
of the requirements for the degree of
Doctor of Philosophy
(Macromolecular Science and Engineering)
in the University of Michigan
2020

Doctoral Committee:

Associate Professor Jeff S. Sakamoto, Chair
Assistant Professor Neil P. Dasgupta
Professor Jinsang Kim
Professor Donald J. Siegel

Arushi Gupta

arushig@umich.edu

ORCID iD: 0000-0002-9788-8274

Dedication

This dissertation is dedicated to the women in my life - my mom Neelam, my sister Vijeta, my sister-in-law Surekha and my sweetest little niece Anika for their unconditional love, faith and support throughout this journey.

Acknowledgements

I sincerely believe that only with the valuable experiences, immense support, and unwavering faith of all the people who have been a part of my journey, this thesis has taken form. Thus, I would like to extend my gratitude towards each and every person who has helped me progress in my life.

First and foremost, I would like to sincerely thank and express my gratitude to my research advisor, Professor Jeff Sakamoto. This journey only started, because he gave me the opportunity to be a part of his research laboratory. I still remember the day when I went up to his office as a Master's student to talk about my interest in the energy field and instantaneously we connected on our vision of bringing positive environmental change in the world. By no means has my Ph.D. been easy and there were numerous hurdles and challenges which I had to overcome both personally and professionally, however, it would not have been possible without Professor Sakamoto keeping faith in me and being patient throughout. The last five years, he has fostered my intellectual and professional growth and has taught me to be more courageous and confident. I also want to thank all the present and past members of Professor Sakamoto's group. From the insightful technical discussions, to the fun times, to our lab organization sessions, to sharing each other's victories and standing by each other in the tough times, I've gone through it all with them. For all the experiences in Professor Sakamoto's lab, I will forever be grateful.

I would also like to thank my committee members, Professor Neil P. Dasgupta, Professor Donald J. Siegel, and Professor Jinsang Kim for their support, their valuable insight towards of thesis and serving in my committee. Professor Kim has not only guided me as my committee member but also as a great teacher for my favorite course I've taken in graduate school (Advanced functional polymers), as the director of Macro attending to and giving great advice and support on all the problems I faced during my graduate school, and most importantly for always reminding me to be a good human being. Over the years I have gotten the opportunity to work with professor Dasgupta and his group member Dr. Eric Kazyak through our collaborations. Professor Dasgupta has always taken the time and immense interest to give me valuable feedback and advice which

has resulted in two manuscripts; I would also like to thank Eric for always being enthusiastic about working together and providing great insight in our work and advice as a friend.

One of the most valuable experiences I've had in graduate school was working as a graduate student instructor under Dr. Tim Chambers. Only after working with Tim, I realized how much I enjoy teaching and care about communicating science. Tim always created an environment of equality where there was space for everyone to express their opinions and grow together as a collective. I want to thank him for being a great mentor and always being there for us. Through this experience not only did I learn about teaching, but I also became better at communicating ideas. Of course, this experience would not be the same if I didn't work with my students and my wonderful fellow GSIs Keara and Kathleen.

Now I want to thank the people who've played a part in making me the person I am today, who motivate me to become better each day, who've stood by my side through the toughest times in my life and have been my cheerleaders for the happy ones.

Starting with my childhood friends who have always taught me to be stronger and have always made me laugh. Particularly I want to thank Supriya for always having faith and confidence in me, even when I didn't have it in myself. I want to thank Naved for changing my outlook in life, restoring my confidence and my strength. If I didn't meet you then I probably wouldn't have realized my potential and wouldn't have fought as hard as I have in life. I want to thank my high school teachers - Dr. Sonal Rajora, who is behind my deep interest in organic chemistry and why I pursued polymers and Sameer sir for always pushing me to do better. I also want to thank all my friends back in India from different walks of my life, who have always wished the best for me and have always been my cheerleaders. Particularly, I want to thank Aaku, Aashna and Debayan for loving me unconditionally and always looking out.

Then I want to thank all my fellow wolverines and honorary wolverines. I don't know how I would have survived without my friends in Michigan. Starting with Vishi, who I've known for over a decade now and is a part of my family. Thanks for being there with me for all these years and just being a person, I can trust and always count on. You are the reason I joined Umich in the first place, so a part of thesis is for you. Then I want to thank Dhanvin, who helped me take the decision of continuing with the PhD after my Master's. Thank you for introducing me to music, for always reminding me of my potential and teaching me to always fight for what I deserve and

never settle. My Michigan memories would not be the same without you in it. I want to thank my roommate Raveena, who was there with me, supporting me through the last steps of this journey. I also want to thank Omkar, Uthara, Ameya and Saurabh for always listening to me and cheering me up. I want to express my gratitude towards my music teacher, Bidisha, for creating my space of peace and tranquility for me in Ann Arbor. I appreciate my friends Simran, Priyanka, Derek, Asma, Joey, Pallavi, Shweta, Niel, Yudha, Sourabh, Roma, Prahlad and Anurag for always showing up for me, no matter the time or distance. Lastly, I want to acknowledge my family far from home - Dr. Regina, Angelica and Mike. In Regina I found a sister, without whom I know I wouldn't have crossed the finish line. The unconditional love and support you've given is beyond what I could have ever asked for. I know I always say this to you, but you are the best human being I know, and I will ever know. Thank you for being you and being a part of my life. I love and respect you very much. In Angelica I found this kid who spreads her joy and enthusiasm wherever she walks and so she did for me as well. When I was at my lowest point, you made sure you didn't leave my sight, and did everything you could to see me smile. And although it is generally me giving you advice, you are someone who has always reminded me of what I deserve, what I want to achieve and what I'm capable of. Thank you for doing that. In Mike, I found a friend in whom I can always confide in. I still feel amazed that you always knew when I needed to talk so thank you for listening to me all these years. And thank you for always giving me work advice and being there with me in all the adventures. Our endless work discussions sitting in front of the oxide box, or at our desk is something I will always miss. Working with you was always fun. Having the three of you in my life is a blessing which I will always be grateful for. I look forward to our future adventures!

I also want to express my sincere gratitude for my counsellors Danielle, Aysha, and Quinn and my wellness coach Janet. Without your compassion, empathy, hard work and commitment towards making the life of other people better, it would not have been possible for me to navigate through this journey. The resources I have discovered during my time with each one of you, the skills I've learned and the growth I've had, is more than I could have ever imagined. I will always be thankful for all of you in my life and your time.

Above all, I want to acknowledge that without my family's support and sacrifices, none of this would have been possible. I want to thank my entire family, my aunts and uncles and cousins

for their unconditional love. My parents, Neelam and Pramod, have always supported me with my decisions in my life, even if they didn't agree and even if they had to make sacrifices for me. My sister, Vijeta, is my armor, she keeps me guarded and is always fighting for me. Thank you for being my pillar of strength and support. I also want to thank my brothers Sharad, who always does anything thing I ask for, and Shashank, who is my best friend at home, and he understands me the way nobody does. I appreciate my sister in law Surekha, who has been a mother to me and has always given me great advice for my life and well-being. I want to thank my cousin, Vikrant, who has been my mentor guiding me with my academic pursuits ever since I was in high school. I want to acknowledge my lovely niece, Anika – you are the reason behind most of my happiness and I am thankful to you for granting me so much love ever since the day you were born.

Finally, I would like to acknowledge the financial support I have received over the years without which it would not be possible for me to pursue my research goals. The work presented in Chapter 4 and Chapter 5 of this thesis was funded by Robert Bosch LLC, Research and Technology Center, Sunnyvale, California, USA. The work presented in Chapter 6 was funded by LG Chem, N025470, and ARPA-E, DE-AR0000653. The preliminary data in Chapter 7 has been supported by ARPA-E, DE-AR0000653. This dissertation comprises of results and conclusion based on the following papers:

Chapter 4. Gupta, A., E. Kazyak, N. Craig, J. Christensen, N. P. Dasgupta, and J. Sakamoto. "Evaluating the effects of temperature and pressure on Li/PEO-LiTFSI interfacial stability and kinetics." *Journal of The Electrochemical Society* 165, no. 11 (2018): A2801-A2806.

Chapter 5. Gupta, Arushi, and Jeff Sakamoto. "Controlling ionic transport through the PEO-LiTFSI/LLZTO interface." *The Electrochemical Society Interface* 28, no. 2 (2019): 63-69.

Chapter 6. Gupta, A.; Kazyak, E.; Dasgupta, N. P.; Sakamoto, J. Electrochemical and Surface Chemistry Analysis of Lithium Lanthanum Zirconium Tantalum Oxide (LLZTO)/ Liquid Electrolyte (LE) Interfaces. *J. Power Sources* 2020, 474 (May), 228598.

Table of Contents

List of Tables

List of Figures

Abstract

The need for high-energy-density Li-ion batteries has provided the impetus to replace graphite anodes with Li metal anodes. Unfortunately, the liquid electrolytes (LEs) used in state-of-the-art (SOA) Li-ion batteries are unstable with Li metal. Owing to its high ionic conductivity, stability against Li and safety, Lithium Lanthanum Zirconium Tantalum Oxide (LLZTO), a solid ceramic electrolyte (SE), has been suggested as a promising alternative. However, the implementation of the SE in an all-solid-state battery could lead to cycling instabilities due to the formation of a resistive, electrochemically, and mechanically unstable cathode/SE interface. One potential approach to overcome the challenges is by introducing a gel polymer electrolyte (GPE) as a catholyte. In this hybrid electrolyte scheme, the LLZTO protects Li metal and a GPE improves the LLZTO/cathode interfacial stability and kinetics. The success of this approach, however, is reliant on two main assumptions – a) electrochemical properties of the GPE would not be affected by volumetric changes in the cathode during operation and b) the polymer and liquid electrolyte in the GPE will be (electro)chemically stable against LLZTO. The overarching goal of this thesis was to identify potential shortcomings of these assumptions and provide solutions to address them.

To achieve this goal, the thesis was subdivided into three studies - 1) studying the effects of temperature and pressure on electrochemical performance of a model polymer electrolyte 2) understanding the factors controlling the polymer/LLZTO interfacial kinetics 3) evaluating the stability of LLZTO with potential LEs used in the GPE. With the aid of various characterization techniques including SEM, XRD, Raman Spectroscopy, XPS, electrochemical impedance

spectroscopy, and galvanostatic cycling and unique experimental designs, several important implications were derived from each study.

First, the roles of temperature and pressure on the electrochemical properties of the PEO-LiTFSI model system were evaluated. The results indicate that both, the bulk ionic conductivity and electrode/electrolyte charge transfer kinetics, are affected by temperature and stack pressure. It was observed that activation energy for Li-ion conduction shows a sharper transition at the melting point of the polymer for bulk conduction than for the electrode/electrolyte interface. It was also observed that a critical stack pressure was required to form an optimized electrode/electrolyte interface.

Second, the factors controlling the kinetics and stability of LLZTO with both constituents of the GPE were analyzed. First, using PEO-LiTFSI the underlying factors that control the LLZTO/polymer interfacial kinetics were studied. It was found that the LLZTO surface impurities and Li-ion concentration gradient between the two electrolytes were responsible for the high interfacial resistance ($R_{interface}$). The fundamental knowledge gained in this study enabled a reduction in the $R_{interface}$ from ~95 kOhms.cm^2 down to 180 Ohms.cm^2.

Lastly, the stability of LLZTO was evaluated with different organic solvents and Li salts present in LEs. It was found that $LiPF_6$-containing LE reacts with LLZTO to form LiF, LaF_3, and ZrF_4 at the interface leading to an increased SE/LE $R_{interface}$. It was concluded that the chemical instability at LLZTO/LE interface was specific to the Li salt used. Thus, by selecting Li salts that exhibit stable behavior with LLZTO, the potential chemical instabilities can be avoided. Further, the optimization of Li salt concentration resulted in a low $R_{interface}$ (~30 Ohms.cm^2).

The culmination of the knowledge gained from the studies can be used for the development of hybrid electrolytes for enabling Li metal anodes.

Chapter 1 Introduction

1.1 Motivation

The globally increasing energy demand[1,2] and its dependence on the depleting fossil fuels has had calamitous environmental implications. In the last 40 years the average global surface temperature has risen by 1°C leading to severe and abrupt weather patterns, receding glaciers, extinction of several species of flora and fauna and rising sea levels. There is scientific consensus that the main cause for the rise in temperature is the increasing anthropogenic CO_2 emissions (82% of the greenhouse gases), Figure 1.1 a, in the atmosphere. United States, along with China and India accounted for 85% of net increase in the emissions, where the transportation sector was the largest contributor as shown in Figure 1.1 b[1,3].

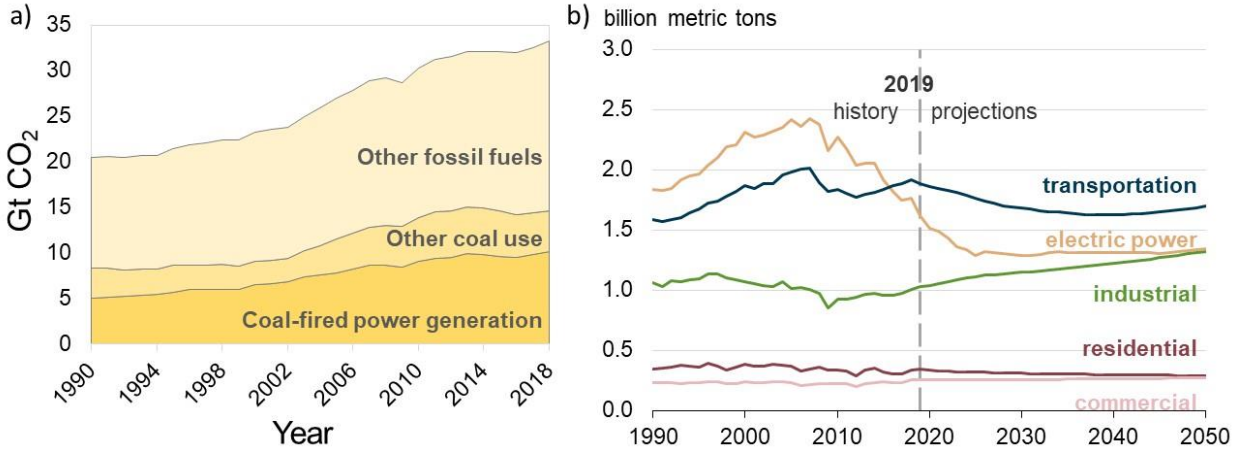

Figure 1.1 *a) Global energy-related carbon dioxide emissions by source.* Based on IEA data from the IEA (2018) Global Energy & CO_2 Status Report 2019, www.iea.org/data-and-statistics. All rights reserved; as modified by [Arushi Gupta][2] *b) U.S. carbon dioxide emissions based on end-use sector.* Source: U.S. Energy Information Administration. Annual Energy Outlook (Jan 2020).[3]

The transportation sector has the highest emissions since it is mainly powered by petroleum-based fuels as shown in Figure 1.2[4]. This has created the impetus for shifting from conventional vehicles, primarily dependent of petroleum, to electric vehicles (EVs) for transportation. Unlike the conventional vehicles, electric vehicles can be powered by cleaner sources of energy (solar, wind, hydro, etc.), thus making them an environmentally safer option.

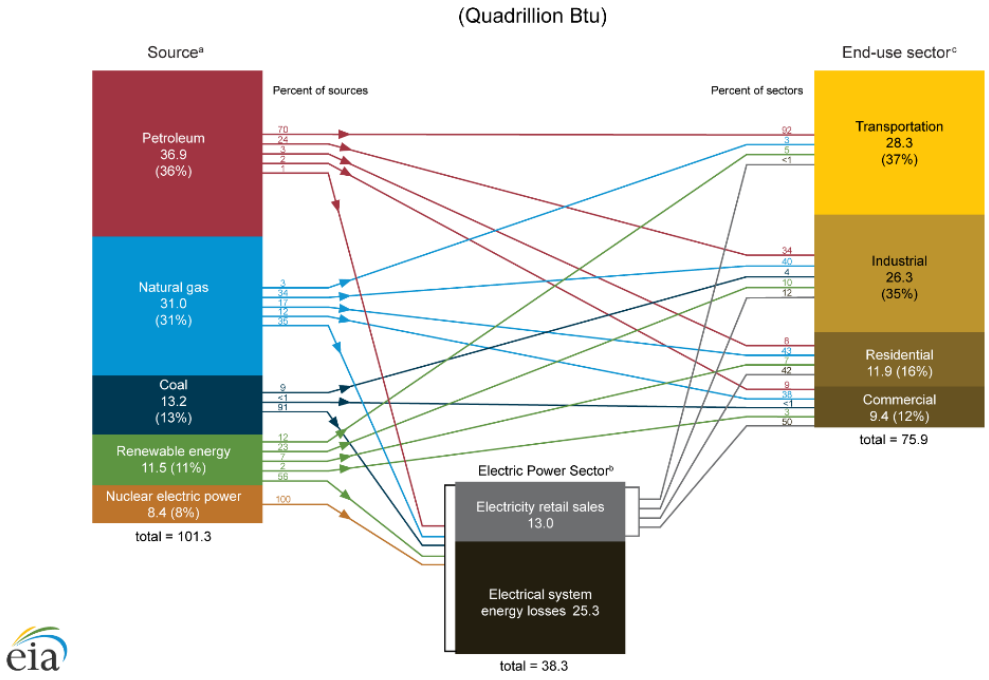

Figure 1.2 *U.S. energy consumption by source and sector, 2018.* Source: U.S. Energy Information Administration., Monthly Energy Review[4]

The push for EVs is reflected by the sharp increase in their development and distribution over the last decade.[5] However, development of energy storage devices (ESDs) which can compete with petroleum-based fuels is a requirement for EVs to largely replace conventional vehicles. ESDs must compete with petroleum-based fuels in terms of cost, driving range (energy density, $Wh.l^{-1}$), rate of vehicular acceleration (power density - $W.l^{-1}$), infrastructure and safety. The cost

reduction and infrastructural development are critical to the widespread utilization of EVs. However, the performance (energy density and power density) of the ESDs itself is not yet comparable to that of internal combustion (IC) engines as shown in the Ragone plot[6] (Figure 1.3). Looking at the two extremes in the Ragone plot, fuel cells provide the highest energy density and capacitors provide the highest power density. None of the two, however, meet the DOE requirements for EVs for both, energy density and power density.[7] On the contrary, Li-ion batteries provide a conciliation between the energy density and power density, making them the current dominating technology in the market for EVs.

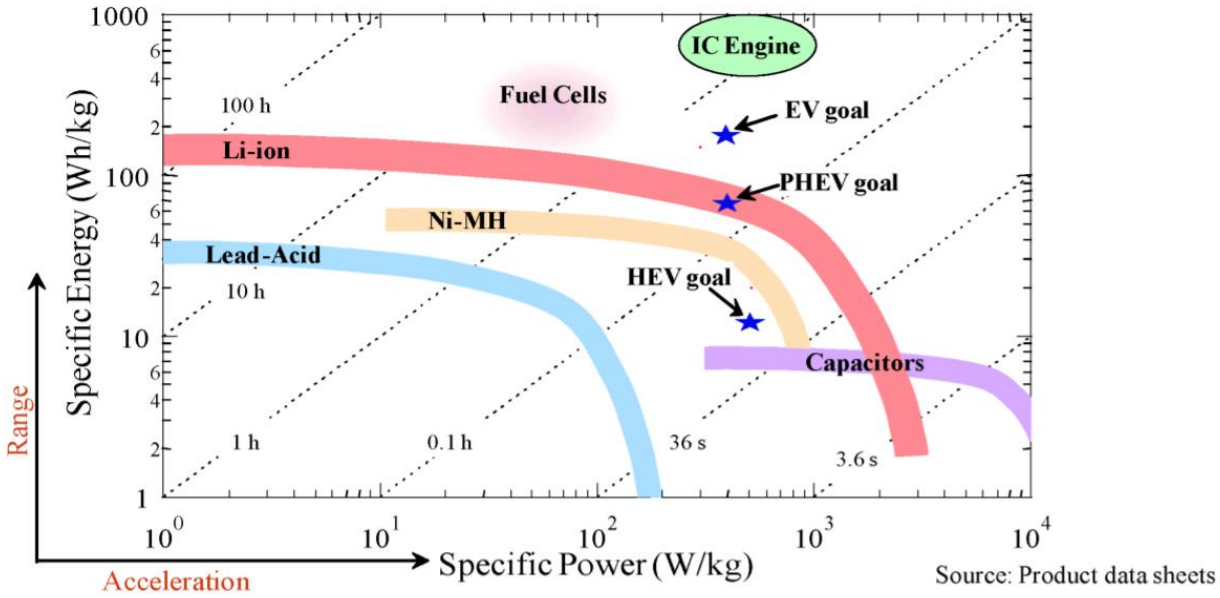

Figure 1.3 *Ragone plot: Specific energy against specific power for various electrochemical energy storage technologies.* Reprinted from [Srinivasan, V. Batteries for Vehicular Applications. *Batter. Manuf. Electr. Hybrid Veh.* 2011, *283* (September 2008), 135–152], with the permission of AIP Publishing. [6]

1.2. State-of-the-art (SOA) Li-ion battery

Batteries are energy storage devices (ESDs) where the energy stored as chemical energy is converted in electrical energy by undergoing an electrochemical reaction. Based on the battery

chemistry and construction there are two types of batteries – primary and secondary batteries.[8] The batteries where electrochemical reaction is irreversible are non-rechargeable. This means that once the battery is completely discharged, it cannot be recharged. Such batteries are known as primary batteries. The batteries where the electrochemical reaction is reversible, i.e., the battery can be repeatedly discharged/charged are rechargeable batteries or secondary batteries. Upon discharge, an external energy is applied to the battery for the reverse reaction to occur in order to charge the battery.

State-of-the-art Li-ion batteries fall under the category of rechargeable/secondary batteries, where the battery is charged/discharged hundred to thousands of times.[9] Akira Yoshino, (at Asahi Kasei Corporation) was the first to make lithium-ion rechargeable battery with LiCoO2 (LCO) cathode and graphite anode.[10] The battery is comprised of three main components – an anode (negative electrode), a cathode (positive electrode) and an ionically conducting electrolyte which separates the two electrodes (Figure 1.4).[9]

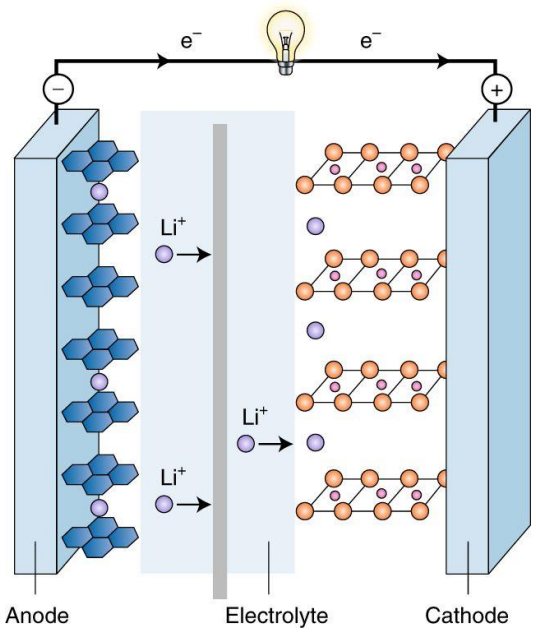

Figure 1.4 *Schematic of a Li-ion battery.*[10]

The typical anode used in Li-ion batteries is graphite. Conventional cathode materials are layered transition metal oxides such as $LiCoO_2$ (LCO), $LiNi_{1-x-y}Co_xMn_yO_2$ (NCM) and $LiNi_{1-x-y}Co_xAl_yO_2$ (NCA). Typically, organic solvent-based liquid electrolytes (LEs) are utilized in Li-ion batteries, like 1M $LiPF_6$ in a mixture of ethylene carbonate (EC) and dimethyl carbonate (DMC) (50:50 vol%). Organic electrolytes are used over aqueous electrolytes (stable up to 1.5 V) due to larger electrochemical stability window. Additionally, a separator (porous polymer infiltrated with the LE) in the electrolyte is used to avoid any physical contact between the two electrodes which could cause a short-circuit. The electrolyte is responsible for the selective transport of Li ions between the two electrodes, blocking any electronic transport. Once at the electrode/electrolyte interface, the Li ions are reversibly inserted/extracted from the electrodes causing reduction/oxidation (redox) reaction of the electrode species. In response to the transfer of ions, electronic transport occurs in the external circuit. This has been illustrated in Figure 1.4. During discharge Li loses an electron to form a Li ion which deintercalates or extracts out of the graphene layer (anode). Then it diffuses through the electrolyte and intercalates into the cathode. Simultaneously the electron from the anode travels through the external circuit to the cathode and causes the reduction of the transition metal. During charge an external electrical energy is applied which causes the Li ion to deintercalate from the cathode with the simultaneous oxidation of the transition metal with the loss of an electron which moves through the external circuit to the anode. The Li ion from the cathode diffuses through the electrolyte, intercalates into graphite and gains an electron to form LiC_6. Thus, the redox reaction causes the electronic transport which then powers a load such as an electric vehicle (EV). The driving force behind this chemical reaction is the chemical potential difference between the two electrodes which is represented by the equation

–

$$\Delta G_r^o = -zFE \quad (1.1)$$

where ΔG_r^o is the standard Gibbs free energy change of the reaction, E is the voltage difference between the electrodes, z is the number of electrons associated with charge transfer and F is Faraday's constant (96,486 coulombs). ΔG_r^o is given by Joules per mole of reaction; 1 Joule is the product of one Coulomb and one Volt.[11]

Although Li-ion batteries have been the leading battery technology, they still do not meet the DOE VTO requirements (driving range ~300 miles) for EVs[7]. Thus, advanced batteries with higher energy densities are required to meet the goals for the widespread adoption of EVs.

1.3. Solid state batteries with Li metal anodes

As discussed, there is still progress needed for Li-ion battery technology to meet the DOE targets for EVs. With the demand for reducing cost (~$100/kWh[7]), increasing performance (500 Wh/l, 235 Wh/kg at systems level[7]) there is a need to develop advanced batteries. Since the energy density and power density is dependent on the energy packed in the electrodes, the common approach employed to the improve the performance characteristics is to replace the anodes and cathodes. Particularly, in graphite anodes Li is the only active species and the graphite just adds to the dead weight to the battery. Thus, one promising approach is the replacement of the graphitic anodes in conventional Li-ion batteries with Li metal anodes which would lead to a 50% increase in energy density.[12] However, one caveat with this approach is that the organic solvent-based liquid electrolyte used with graphitic anodes are unstable with Li metal.[13–17] The conventional liquid electrolytes react with Li to form an unstable solid electrolyte interphase (SEI), leading to cycling instabilities and safety concerns. A promising approach to overcome the challenges of conventional LEs is the use of solid-state electrolytes (SSEs).[18] There is a plethora of solid-state

electrolytes which have been investigated to use with Li metal anodes.[19–22] Ideally for the SSE to be considered promising it should fulfill the following requirements – [23,24]

a) High Li ion conductivity; $>10^{-4}$ S cm^{-1} at 298 K.
b) Transference number for electronic conduction should be nearly 0 to avoid any self-discharge; $t_e \sim 0$.[25]
c) Electrochemical stability window 0 to ≥ 5V; The large electrochemical window of the SSE allows using high voltages cathodes without the degradation of the electrolyte.[26]
d) Physically and chemically stable against the anode and the cathode. Any instability of the SSE with either of the electrodes would lead poor cycling performance characteristics.
e) Thermodynamic stability for a wide operating temperature range; The temperature range for operation of EVs is -30ºC to 52ºC.[27]
f) Ease of processability; Low cost of manufacturing robust thin films.
g) High resistance to Li metal penetration during cycling
h) Low interfacial resistance with both the electrodes[28]

Considering the above criteria there have been substantial efforts made in the last decade towards the successful development of SSEs for implementation in a Li metal battery. Even after significant progress there has been no solid electrolyte which satisfies all the above criteria. To understand the advantages and limitations of different solid electrolytes, they have been reviewed below. Based on the Li ion transport there are two main categories of electrolytes which are studied extensively – a) organic or polymer electrolytes and b) inorganic electrolytes.

1.3.1. Polymer electrolytes

Polymer electrolytes have been around for almost half a century. Fenton *et al* in 1973 reported the idea of the dissolution of alkali metal salts in polyethylene oxide (PEO) making it

ionically conducting.[29] Soon after, in 1978, Armand *et al* proposed a PEO-Li salt solid polymer electrolyte (SPE) with Li ion conductivity of 10^{-4} S/cm at 40-60°C.[30] The low flammability, ease of processability, low cost, mechanical compliance and high shock tolerance are a few properties of polymer electrolytes which make them an appealing solid electrolyte candidate for Li-based batteries and are responsible for their rapid development.[23] However, there are properties of polymer electrolytes which inhibit their commercial application, two important ones being ionic conductivity and Li ion transference number (t_{Li+}).[31–33] Ideally, the t_{Li+} for a solid electrolyte should be close to unity, however, since in a polymer electrolyte both the cation and the anion of the Li salt are mobile species the t_{Li+} is much lower than that.[33] The ionic conductivity of semi-crystalline polymer is described by the Arrhenius equation[34] –

$$\sigma = \sigma_0 \exp\left(-\frac{E_A}{RT}\right) \tag{1.2}$$

where σ is the ionic conductivity, E_A is the activation energy, T is the temperature of measurement and R is the universal gas constant. Fully amorphous polymer electrolytes follow the temperature dependence according to the Vogel–Tammann–Fulcher VTF equation[34] –

$$\sigma = AT^{\frac{1}{2}} \exp[E_A/(T - T_g)] \tag{1.3}$$

where, σ is the ionic conductivity, *A* is the pre-exponential factor, T is the temperature of measurement, T_g is the glass transition temperature of the polymer electrolyte and E_A is the activation energy.

Polymer electrolytes can be further subdivided into three different categories – solid polymer electrolytes (SPEs) also known as dry polymer electrolytes, gel polymer electrolytes (GPEs) and composite polymer electrolytes (CPEs).[35]

1.3.1.1. Solid polymer electrolytes (SPEs) – SPEs are polymer electrolytes with a polymer host matrix and a Li salt being the main constituents. The Li salt is responsible for an increase in Li ion conductivity in the polymer and the polymer matrix is responsible for the Li ion transport. An ideal polymer matrix should have high solubility of the Li salt through cation solvation, high chain mobility for effective charge transport, high dielectric constant for effective Li salt cation and anion separation and high molecular weight for suitable mechanical properties.[36] SPEs can be easily processed by solution casting or molding.[37] There are different SPEs which have been studied including PEO-based SPEs[30], polycarbonate-based SPEs[38], polyester-based SPEs[39], and polysiloxane-based SPEs[40]. Polysiloxane-based SPE is an example of an inorganic polymer electrolyte.

Polyethylene-based SPEs are the most common and well-studied SPE. Polyethylene oxide is a semi crystalline polymer with a melting point (m.p.) above 60^{o}C.[41] The mechanism of Li ion transport in a PEO-based SPE is shown in figure 1.5. As discussed, due to the high solvation and dielectric constant of PEO the Li ion are dissociated from the counter ions. The dissociated Li ion are coordinated to the oxygen atoms in the PEO backbone. On application of an electric field the Li ions break their coordination from an oxygen in the PEO electrolyte and hop on to another oxygen atom either on the same chain (intrachain hoping) or on a different chain (interchain hoping). The continuous rearrangement and movement of the Li ion results in long-range transport of the Li ions.[41,42] Since the ionic transport is dependent on the segmental motion of the polymer it is thus dependent on the mobility of the polymer chains. Since the crystalline domain in the polymer has limited mobility, the amorphous domain is mainly where ionic conduction occurs. Thus, the ionic conductivity of the PEO-based electrolytes is dependent of temperature and molecular weight.[43] As mentioned above, the m.p. of PEO is above 60^{o}C, thus PEO-based SPEs

have a limited room temperature ionic conductivity (10^{-8} – 10^{-6} S cm^{-1}).[42] The low room temperature conductivity and high resistance against Li has limited the practical application of PEO-based electrolytes.

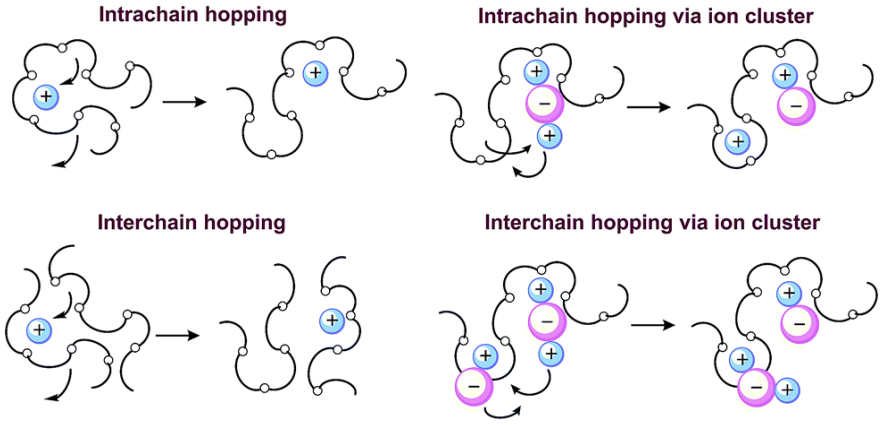

Figure 1.5 *Mechanism of ionic transport in PEO-based electrolytes. J. Mater. Chem. A*, 2015,3, 19218-19253 - Reproduced by permission of The Royal Society of Chemistry [41]

1.3.1.2. Gel polymer electrolytes (GPEs) – GPEs are a quasi-solid electrolyte in which a liquid electrolyte is trapped in a polymer matrix. GPEs are mainly constituted of a polymer matrix, organic solvents as plasticizers and Li salts. Examples of common polymer matrices are polyacrylonitrile (PAN), polyethylene oxide (PEO), poly(vinylidene fluoride-co-hexafluoropropylene) (PVDF-HFP), poly(methyl methacrylate) (PMMA), and polyvinylidene fluoride (PVDF). Examples of organic solvents are carbonates (propylene carbonate (PC), ethylene carbonate (EC), etc.), ethers (1,2-dioxolane (DOL), dimethoxymethane (DME), etc.) and ionic liquids.[23] The ionic conduction in GPEs is mainly through the liquid electrolyte (Li salts dissolved in organic solvent) which is contained in the polymer matrix giving it mechanical strength, enhanced safety and reduced risk of leakage.[44] Since the main ionic conduction is through the liquid electrolyte, GPEs have a high ionic conductivity in comparison to SPEs (>10^{-4} S cm^{-4} at 25°C). One major limitation of GPEs is

that the liquid electrolyte not only decreases the mechanical strength but also reduces the thermal stability. This is what prevents the GPEs to be commercially used.

1.3.1.3. Composite polymer electrolytes (CPEs) – CPEs are solid polymer electrolytes with inorganic fillers added in polymer electrolyte to improve their ionic conductivity and mechanical strength. There are two types of filler which can be added to the SPE – a) inactive filler: where the filler is non-ionically conductive b) active filler: where the filler is ionically conductive.[35] The inactive inorganic fillers in CPEs serve two purposes – a) they act to disrupt the crystallinity of the SPE and thus, enhancing its ionic conductivity[45] b) they enhance the mechanical strength of the SPE. Examples of inactive filler used in SPEs are nanoparticles like Al_2O_3, SiO_2, etc.[46,47] The active inorganic fillers used in CPEs are generally fast ion conductors where the goal of adding them to the SPE is for mixed ionic conduction from both the SPE and the active filler. This will ideally significantly improve the ionic conductivity of the SPE and improve its mechanical properties. There are CPEs with active fillers that have a high room temperature ionic conductivity of 10^{-2} S cm^{-1}.[48] These electrolytes however, either have poor interfacial contact with the electrodes or do not show a significant enhancement in ionic conductivity.[49] Examples of active filler used in SPEs are fast ion conductors like garnet-type, NASICON-type, sulfides, etc.[50,51]

Even with the rapid development of polymer electrolytes their low room temperature conductivity, poor thermal stability, low Li ion transference number due to the presence of mobile anions and high interfacial resistance against Li metal still restricts their practical application in Li metal batteries.

1.3.2. Inorganic Electrolytes

The different types of inorganic solid electrolyte which are widely studied can be divided into two categories sulfides and oxides.

1.3.2.1. Sulfide-based SSE – Sulfide-based electrolytes gained a lot of traction as promising candidates for SSEs due to their high room temperature conductivity and low activation barrier for Li ion conduction and low charge transfer resistance with Li metal.[52] The room temperature ionic conductivity of sulfides can be as high as 10^{-2} S cm^{-1}. The high ionic conductivity is due to the larger size and higher polarization of the sulfide ions over oxide ions, forming a weaker bond with Li ions and hence, a higher Li ion mobility.[53] They also provide a lower processing temperature and pressure in comparison with oxide-based electrolytes.[54] However, the moisture sensitivity, low oxidation stability, chemical stability against Li and fragility of sulfide electrolytes are their major limitations.[24]

The sulfide electrolytes are further subdivided into categories – amorphous, crystalline and glass ceramic sulfide electrolytes, where glass ceramics possess the highest conductivity. Examples of sulfide electrolytes include $Li_7P_3S_{11}$ (17 $mS \cdot cm^{-1}$)[55], $Li_{10}GeP_2S_{12}$ (12 $mS \cdot cm^{-1}$)[53], and thio-LISICON conductor $Li_{3.25}Ge_{0.25}P_{0.75}S_4$ (2.2 $mS \cdot cm^{-1}$)[56].

1.3.2.2. Oxide-based electrolytes – Generally, oxide-based electrolytes provide high oxidation stability, chemical stability, and an ionic conductivity between polymers and sulfides.[57] However, different oxide-based electrolytes have different advantages and limitations. The oxide-based electrolytes which have been studied extensively include perovskite-type, NASICON-type and garnet-type.

An example of the perovskite-type electrolyte is lithium lanthanum titanate (LLTO) which can have a high intragranular Li-ion conductivity (>10^{-3} S cm^{-1}) depending upon the stoichiometric composition.[58] However, the grain boundary resistance of LLTO is inherently high (~10^{-5} S cm^{-1}). LLTO also reduces in contact with Li metal where the t_{Li+} for reduced state is 0.0095 thus limiting its application as an SSE for Li metal anodes.

Lithium aluminum titanium phosphate (LATP) is a widely studied NASICON-type oxide electrolyte with a high ionic conductivity of 4*10^{-3} S cm^{-1} where the Li ions move between sites in an interconnected channel.[59] However, like LLTO, LATP has a high grain boundary resistance and is chemically unstable against Li metal and thus has limited application as an SSE for Li metal batteries.[59,60]

Garnet-type oxide electrolytes – Garnet-type Li ion conducting SSE were first discovered in 1988 as promising electrolytes with an ionic conductivity of 4*10^{-5} S cm^{-1}.[61] They had a general formula of $Li_5La_3M_2O_{12}$ where M was either Ta^{5+} and Nb^{5+}. Following that there have been various formulations of the garnet electrolyte which have been studied, one of which is $Li_7La_3Zr_2O_{12}$ (LLZO). This formulation of LLZO was reported, by Murugan *et al.* in 2007, to have a high room temperature ionic conductivity of 10^{-4} S cm^{-1}.[62] LLZO SSE exists is two polymorphs – tetragonal (*t*-LLZO) and cubic (*c*-LLZO). Cubic LLZO has an ionic conductivity two order of magnitude higher than tetragonal LLZO and hence *c*-LLZO is the preferred polymorph. The *c*-LLZO is stabilized by partially substituting the Li or Zr sites with a higher valent atom like Al or Ta respectively.[63] To balance the charge imbalance, more Li vacancies are created reaching in the optimal range more stabilization of the *c*-LLZO resulting in high conductivities (10^{-4} to 10^{-3} S cm^{-1}).

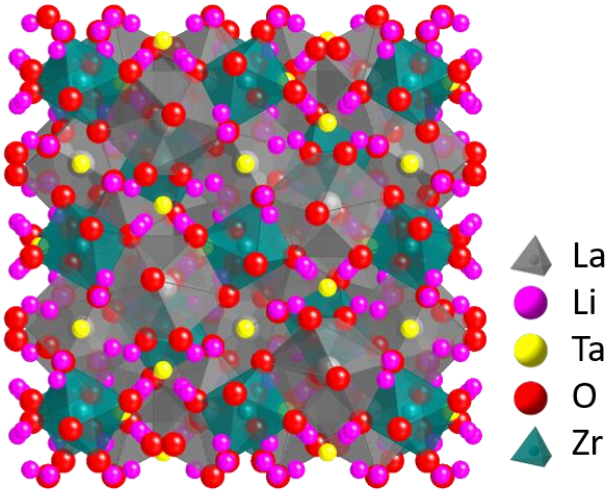

Figure 1.6 *Crystallographic structure of Ta-doped LLZO*

The properties of all the solid electrolytes have been summarized in table 1. Amongst all the electrolytes LLZO is considered as the most promising SSE for enabling Li metal anodes. Besides its high ionic conductivity, it is also chemically stable against Li metal[57], has an ultra-low interfacial resistance with Li metal (<10 Ohms.cm^2)[28], has a large electrochemical stability[26] window and it can be processed in air. Although LLZO has features which makes it very compatible with Li metal there are still technical challenges to be met for the application of LLZO in a Li metal battery. One important consideration with the implementation of LLZO in all-solid Li metal battery is the possible challenges with the formation of solid-solid interfaces within the composite cathodes (between the cathode particles and LLZO particles in the cathode) and at the composite cathode and solid electrolyte interface.[64,65]

Table 1. 1 *Summary of properties Li-ion conducting solid electrolytes*

Electrolyte Type	Conductivity (S cm-1)	Advantages	Disadvantages
SPEs (polyethylene oxide)[41]	10^{-8} to 10^{-6}	• Stable with Li metal • Flexible • Easy to production and scalability • Low cost	• Limited thermal stability • Low room temperature ionic conductivity • Low oxidation voltage
Gel polymer electrolyte[23,44]	10^{-4} to 10^{-3}	• High room temperature ionic conductivity • Higher Li ion transference number than SPEs	• Limited thermal stability • Poor mechanical strength • Low oxidation voltage
Composite polymer electrolyte[35,46,47]	10^{-5} to 10^{-2}	• Higher room temperature ionic conductivity than SPEs • Better mechanical strength than other organic electrolytes	• Limited thermal stability • Low room temperature ionic conductivity • Low Li ion transference number
Thio-LISICON[56]	10^{-4} to 10^{-3}	• Low grain-boundary resistance • High Li ion conductivity • Low processing temperature than oxide-based ceramic electrolytes	• Low oxidation stability • Sensitive to moisture • Poor compatibility with cathode materials • Chemically unstable against Li metal
Perovskite[58]	$>10^{-3}$	• High electrochemical stability • High Li ion conductivity	• Not stable against Li metal • Brittle • High grain boundary resistance
NaSICON[59]	$>10^{-3}$	• High electrochemical stability • High Li ion conductivity	• Not stable against Li metal • Brittle • High grain boundary resistance
Garnet[62,63]	10^{-4} to 10^{-3}	• Stable with Li metal • Low grain-boundary resistance • Can be synthesized in air • High electrochemical stability • High Li ion conductivity	• High temperature processing required • Brittle • High interface resistance against cathode materials

1.4. Problem Statement

For the successful implementation of LLZO in all-solid-state Li metal batteries, LLZO needs to be chemically and mechanically stable with the layered transition metal cathode materials utilized for Li metal. However, previous studies have reported these solid-solid interfaces can lead to rapid capacity fade and high resistance due to chemical instabilites, contact loss, and uncompensated volumetric changes in the cathode.[64,65]

1.4.1. Chemical instability of LLZO with cathode materials

There have been several reports of chemical reaction of LLZO with different cathode materials.[66] Kim *et al*. reported the formation of La_2CoO_4 intermediate layer of ~50 nm at the LCO/LLZO interface.[67] The La_2CoO_4 intermediate layer formed is relatively thick and causes retardation of Li ion insertion and extraction from the cathode, negatively impacting the cycling performance. It was also found that when processed at high temperatures cubic Al-doped LLZO reacts with LCO to form a low ionic conductivity tetragonal LLZO interphase. It was reported that the Al ions diffuse out of the LLZO towards LCO destablizing the cubic phase and causing it to transform to tetragonal LLZO.[68] Further Miara *et al.* have reported theoretical calculation indicating decomposition of LLZO at 3.8 V in contact with cathodes, higher reactivity with LiMnO2 and LiFePO4 than LCO.[69] The reaction between LLZO and LFP leads to formation of Li_3PO_4, $La_2Zr_2O_7$, $LaFeO_3$, $LaFeO_3$, and Fe_2O_3 decomposition products. The reaction of LLZO with different cathodes leads to polarization due to highly resistive interfaces and cycling instabilities.

1.4.2. Mechanical degradation due to volumetric changes in the cathode

It is well known that the insertion/extraction of Li ions in the anode/cathode causes volumetric changes in the electrodes.[70,71] Figure 1.7 shows the volumetric changes in varied electrodes as a function of state of lithiation. It can be observed from the figure that there is a significant change (2-4 %) in the volume of most electrodes which should be equivalent to the partial molar volume of Li, $\bar{V}_m$(Li).[72–74]

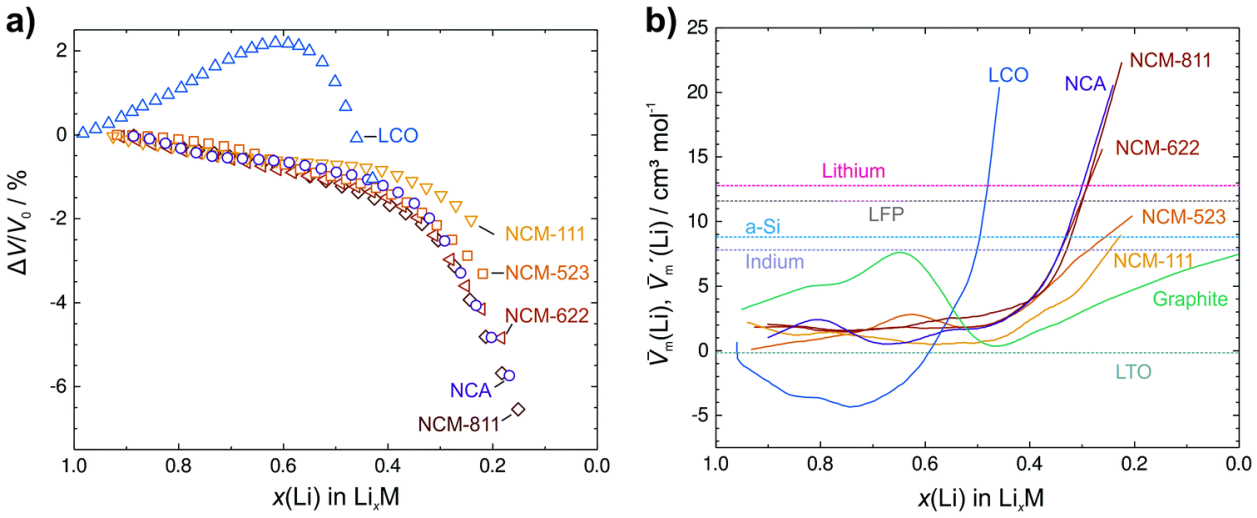

Figure 1.7 *a) The unit cell volume obtained from crystallographic data vs the state of lithiation of positive electrode materials b) Available data for the partial molar volume $\bar{V}_m$(Li) of Li*[72–74]

In Li-ion batteries with LEs a) these volumetric changes in the anode materials cause the deterioration of the solid electrolyte interface during charge/discharge cycling[75,76] b) these volumetric changes in the cathode primary particles causes fracture in the agglomerates/secondary particles.[64,76] Both the situations cause cycling instabilities and capacity fade. In Li-ion batteries employing LEs the stresses generated are much more localized and the LE does not transfer the stress over. Similar behavior can be expected from soft elastic polymer electrolyte due to their compliant nature.[72]

However, in case of inorganic SE in an all-solid state Li metal battery, the impact of volumetric changes in the cathode will be significant.[77] Due to the volumetric changes in the cathode there is a possibility of fracturing the SE membrane. The volumetric changes of the cathode particles would also create stress on the SE particles in the composite cathode which may cause local volume changes.[64,78] If the SE exhibits a substantially higher elastic modulus than the cathode, it is also possible that the SE furthers the stress on the cathode causing fracture. Overall, solid-state batteries can undergo severe mechanical degradation due to volumetric changes in the cathode. The stress caused due to lithiation/delithiation is called lithium induced stress.[72] This compressive stress can influence the reaction itself, for example it can cause a decrease in lithium solubility in the electrode material which would lead to a loss in capacity.[79]

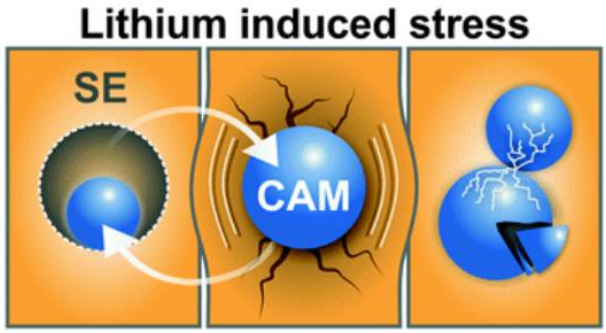

Figure 1.8 *Schematic illustrating the fracture of SE due to the volume changes in the cathode.*[72]

Thus, it can be concluded that without a liquid or a soft elastic polymer these volumetric changes can cause delamination of the electrodes from the SE. Further repeated charging and discharging can cause fracture for both the cathode and the SE leading to high resistances and unstable cycling and eventually causing cell failure.[64,80,81]

1.5. The hybrid electrolyte approach

After understanding the chemical and mechanical challenges with the implementation of LLZO SE in a solid-state battery, a hybrid electrolyte approach has been discussed as a potential solution to overcome these challenges.[82–84] The hybrid electrolyte approach allows for the elimination of LLZO/rigid cathodes interfaces by the introduction of a Li ion conductor in the cathode like an LE, SPE or a GPE.[84] Knowing the limitations of LEs and SPEs – the properties of a GPEs are well suited for this approach. Unlike SPEs, GPEs have a high room temperature ionic conductivity, and would likely comply with the volumetric changes in the cathode at room temperature. However, it is important to study the effects of thermal transitions and external pressure on the electrochemical performance of the GPE. Similarly, unlike LEs there are no challenges due to leakage since the LE in a GPE is trapped in the structure of the GPE. Figure 1.8 shows the schematic of a bilaminar hybrid electrolyte scheme, where LLZO serve to protect the anode and a GPE overcomes the challenges of solid-solid interfaces.

Although after the addition of the GPE the battery is not a true solid-state battery, it does reduce the safety concerns of LE since the quantity of the LE used in the GPE is significantly lower, the LE is entrapped in the polymer matrix thus leakage related problems are mitigated and the elimination of the LE/Li metal unstable SEI. Even though this approach provides a plausible solution to overcome the challenges of the LLZO and cathode interfaces, the approach introduces new interfaces which warrant inspection. The focus of this thesis is to investigate and resolve the possible challenges which might arise with this battery architecture employing the hybrid electrolyte approach.

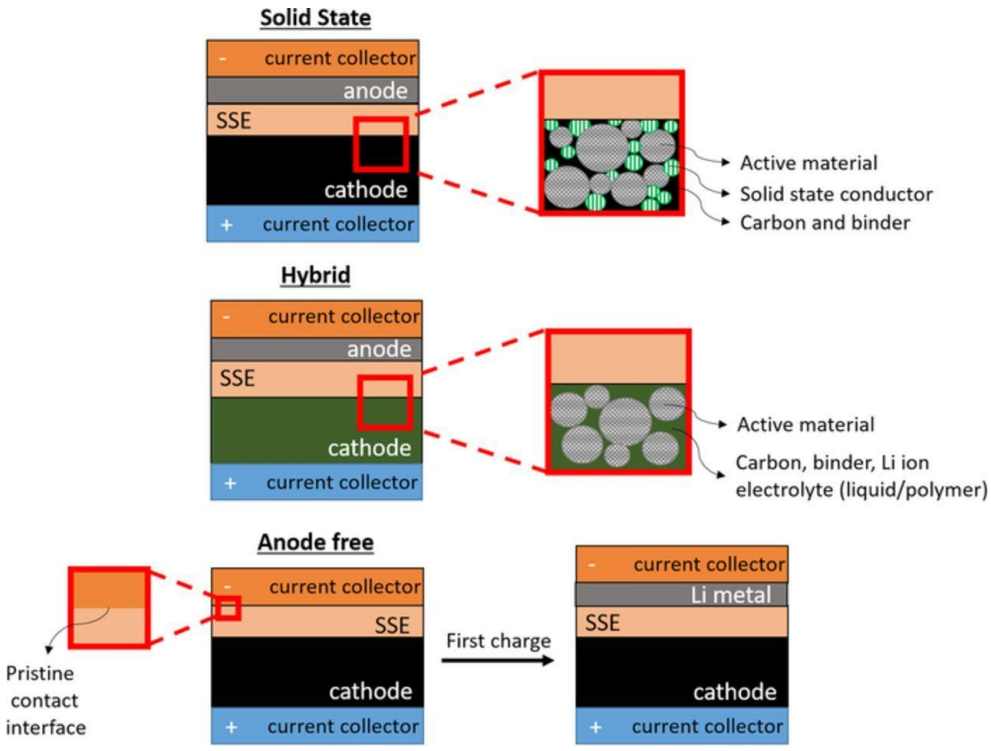

Figure 1.9 *Schematic of a Li metal battery employing a hybrid electrolyte approach.*[82] This figure is reproduced from - Kian Kerman *et al* 2017 *J. Electrochem. Soc.* 164 A1731

The next chapter of this work is dedicated to identifying the possible challenges with the hybrid electrolyte approach and lay out the specific aims and objectives of this thesis.

Chapter 2 Aims and Objectives

2.1. Research Objectives

LLZO used in combination with a GPE infiltrated composite cathode (a hybrid electrolyte approach) is a promising cell design to overcome the challenges with the LLZO and rigid cathode interfaces while enabling Li metal anodes.[82] This argument is however based on two important underlying assumption – a) The electrochemical properties of the GPE comply well with the volumetric changes in the cathode and the temperature dependence of the properties has been neglected. b) The electrochemical stability of the LLZO/GPE interface is assumed, which has not been very well understood. Thus, there is a need to first systematically understand the effects of external factors on the electrochemical performance of a model polymer electrolyte and then an investigation of the chemical interactions and the electrochemical performance of the new interfaces that arise in this scheme is required. This work is focused on developing a fundamental understanding of the effects of external variables, surface treatment, carrier concentration, chemical reactions on the electrochemical performance of the interfaces in the cell. From the knowledge gained from studying the various parameters, it would enable us to provide guidelines for the successful implementation of this approach.

The overarching objective of this work is mainly divided into two parts – a) studying the dependence of the electrochemical performance of a model polymer electrolyte on external variables. b) studying the kinetics, chemical and electrochemical stability of the LLZO/GPE interface. Since the GPE electrolyte is composed of a polymer matrix, Li salt and organic solvents,

it was important to study the interactions between the individual constituents and LLZO SE. The knowledge gained of the factors that control the interaction between LLZO and the different constituents, can enable us to improve the LLZO/GPE charge transfer kinetics.

2.2. Specific aims

To achieve overarching objective of the thesis, there are specific aims which need to be accomplished (illustrated in figure 2.1) – 1) studying the external factors that impact the electrochemical performance of a polymer electrolyte 2) understanding the factors controlling the polymer/LLZO interfacial kinetics 3) evaluating the stability of LLZO with potential liquid electrolytes used in the gel polymer electrolyte. The specific aims are explored in the subsequent chapters of this thesis.

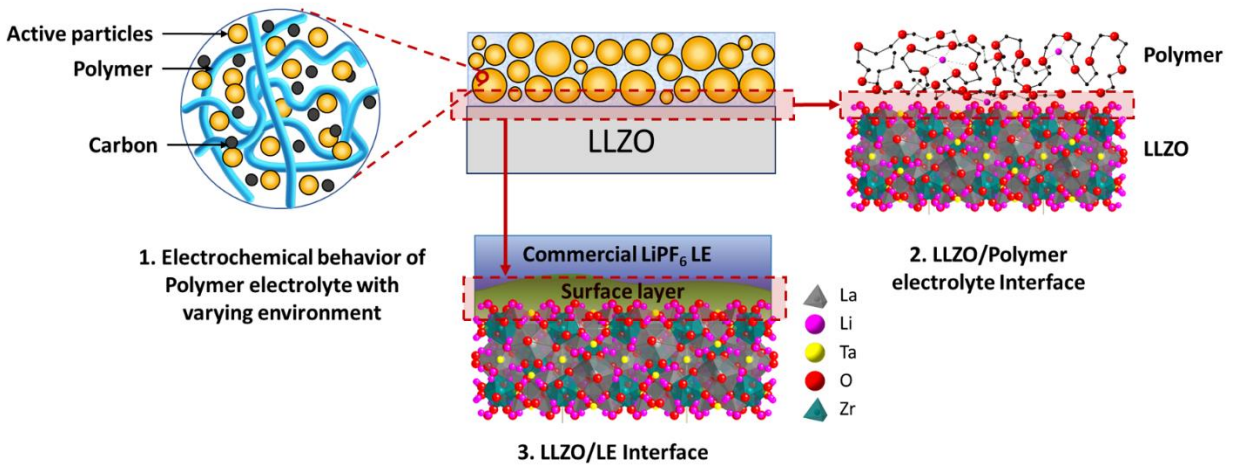

Figure 2.1 *Schematic of a Li metal battery showing the specific aims which need to be accomplished for the successful implementation of the hybrid electrolyte approach*

A brief outline of the different chapters in this thesis is presented as under:

Chapter 3 discusses the experimental methods used for the synthesis and processing of the electrolytes relevant to this work. It also discusses the chemical and electrochemical

characterization techniques and experimental designs used to investigate and evaluate the electrochemical performance of the different electrolyte systems.

Chapter 4 is focused on studying the effects of temperature and stack pressure on the electrochemical performance of a polymer electrolyte. We chose polyethylene oxide (PEO) as our model polymer electrolyte since PEO is a very well-studied polymer. Thus, the goal of this work was to understand the effects of temperature and stack pressure on the electrochemical performance of the model polymer system. The importance of doing so is because a) GPEs have a very low tolerance to thermal transitions, thus knowing the dependence of the electrochemical properties of the polymer would enable us to predict the behavior of our GPE b) The stresses in the battery due to volumetric changes in the cathode are accompanied with external pressure applied on the batteries to maintain continuous contact between the different elements of the battery. Thus, it is important to study the effects of stack pressure on electrochemical performance of a polymer electrolyte since it would be responsible for charge transport from the cathode particles to LLZO.

Chapter 5 is focused on understanding the factors controlling the polymer/LLZO interfacial kinetics. A low interfacial resistance is necessary for facile Li ion transport across the polymer/LLZO interface boundary. However, it has been previously reported that LLZO has a high interfacial resistance with a solid polymer electrolyte.[85] In this work we first validate the high interfacial resistance between LLZO and the solid polymer electrolyte. The main goal of this work was to understand the underlying mechanisms that control the Li ion transport across a polymer electrolyte and LLZO interface and then utilize this fundamental understanding to minimize the interfacial resistance between the two electrolytes.

Chapter 6 is focused on evaluating the stability of LLZO with potential liquid electrolytes used in the gel polymer electrolyte. The stability of LLZO electrolyte in presence of liquid electrolytes is critical for the implementation of GPE as hybrid electrolytes. However, previous reports indicate that LLZO reacts with state-of-the-art (SOA) LE electrolyte to form a high resistance interphase.[86,87] The goal of this study was to identify the specific component of the LE that reacts with the SE. We believe that by understanding the reactions between the SE and LE, it is possible to develop approaches to limit or eliminate chemical side reactions at the interface. This further leads to a stable low interfacial resistance between the electrolytes.

Chapter 7 provides the conclusion which summarizes the results and outcomes of the previous chapters. From the knowledge gained in the previous chapters preliminary data is provided for LLZO/GPE hybrid electrolyte which provides motivation for the future work towards the employment of the hybrid electrolytes in Li metal batteries.

Chapter 3 Experimental Methods

This section provides the details of the synthesis and processing of the electrolytes that are an integral part of this dissertation. The characterization techniques used to study the (electro)chemical performance of the electrolytes will also be discussed.

3.1 Materials Processing

3.1.1 Polyethylene oxide (PEO)-based solid polymer electrolyte

In this dissertation, polyethylene oxide (PEO)-based electrolytes were used as the model polymer electrolyte to study the factors that affect the electrochemical properties of polymer electrolytes and their interface with LLZO SE. PEO has suitable properties for an SPE, such as high Li ion donor number, chain mobility, ease of processability and a high dielectric constant.[41] Therefore, it is the most well-studied polymer making it a relevant model system to study. In addition, for the Li salt, a salt with a larger anion was preferred. This is because a larger anion possesses a well delocalized negative charge and lower mobility than smaller anions thus increasing the Li ion conductivity and Li ion transference number of the SPE respectively.[41] Therefore, in this work, Lithium bis(trifluoromethanesulfonyl)imide (LiTFSI) Li salt was chosen in combination of PEO. The PEO-LiTFSI electrolyte membranes were fabricated using solution casting and hot-pressing. A brief overview of the fabrication methods and characterization techniques used to study the properties of the polymer are discussed below.

3.1.1.1. Solution casting

For solution casting PEO-LiTFSI electrolyte membranes Polyethylene oxide (PEO) (molecular weight 4,000,000, Polysciences, Inc.), LiTFSI (99.95%, Sigma Aldrich), and Acetonitrile, ACN (99.8%, Sigma Aldrich), were used. A high molecular weight PEO was used for better mechanical properties.[41] A higher molecular polymer also causes chain entanglement which can trap large anions further impeding anionic transport. The PEO and LiTFSI were vacuum dried at 60°C for 24 hours to eliminate any moisture. PEO and LiTFSI were weighed in an Ar-filled dry glove box (less than 0.5 ppm H_2O andO_2) to the desired [EO]:[Li] ratio. First, the LiTFSI was dissolved in acetonitrile to form a clear solution. Next, PEO was slowly added to the solution, which was stirred for 24 hours at room temperature and then at 60°C for 12 hours to assure dissolution. The electrolyte membranes were prepared by casting the PEO/LiTFSI solution into a polytetrafluoroethylene (PTFE) mold, allowed to cool to eliminate bubbles formed while stirring. The cast electrolyte membranes were dried under partial vacuum (127 Torr) for 24 hours then heated to eliminate residual solvent under high vacuum (558 Torr) for another 24 hours. The membranes ranged in thickness between 50 and 500 microns.

3.1.1.2 Hot pressing

For studying the PEO/LLZO interfacial kinetics a solvent-free hot-pressing fabrication technique was preferred to ensure that there was no remaining solvent molecule which would otherwise cause a variation in the results. For preparing PEO-LiTFSI electrolyte membranes by a solvent-free hot-pressing method PEO (molecular weight 4,000,000, Polysciences, Inc.) and LiTFSI (99.95%, Sigma Aldrich) were used. As with the previous method, both the PEO and the LiTFSI were dried under vacuum at 60°C for 24 hours to eliminate moisture. The polymer and salt were then weighed in an argon dry glove box (less than 0.5 ppm H_2O and O_2) to the desired

[EO]:[Li] ratio. PEO and LiTFSI were intimately mixed using a mortar and pestle and then hot-pressed in a ½ inch stainless-steel die at 100°C for 10 minutes under 3.5 MPa (Figure 3.1). The pressure was applied using an Instron (Instron 5944 tension/compression testing unit) inside an argon filled glove box (0.5ppm O_2 and H_2O). The temperature was tracked using two type-K thermocouples attached to the Ni pins to ensure that there was no gradient in temperature along the length of the die. A heating tape was wrapped around the die for heating the die to the hot-pressing temperature and was covered with quartz wool for insulation. Using stainless-steel spacers multiple samples were produced in one hot-press. Using this hot-pressing technique PEO-LiTFSI electrolytes of the desired [EO]:[Li] ratio were fabricated. The thickness of the membranes could be controlled between 100 microns to as thick as desired.

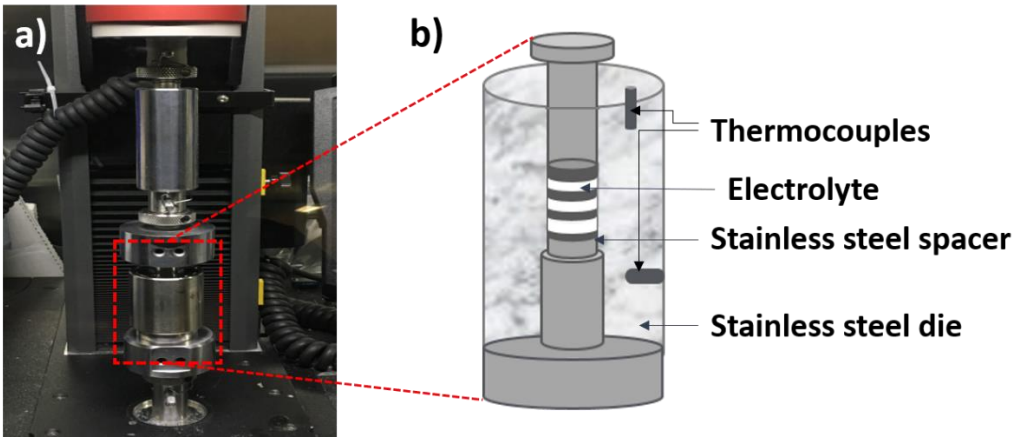

Figure 3.1 *a) Optical image of the die placed between the compression heads of an Instron; b) Schematic of the stainless-steel hot-pressing die configuration*

3.1.1.3. PEO-LiTFSI electrolyte membrane material characterization

Raman spectroscopy (Horiba Micro Raman Spectrometer housed in an argon-filled glovebox) was used to characterize the film and to determine if any residual moisture and solvent was present. Energy Dispersive Spectroscopy (EDS) (Hitachi: S3500N SEM w/ EDAX) was performed to characterize the homogeneity of the Li salt in the PEO matrix.

3.1.1.4. Thermal properties analysis

As discussed in section 1.3.1.1 the thermal transitions in a polymer significantly affect their electrochemical properties. Thus, differential scanning calorimetry (DSC) was used to correlate the thermal transitions of the PEO-LiTFSI with its electrochemical properties and to study the temperature dependence of those properties. For all the DSC measurements in this work for PEO-LiTFSI electrolyte membranes, the samples were heated from 25°C to 80°C at a constant heating rate of 2°C min^{-1}. Figure 3.2 shows the DSC thermogram for a PEO-LiTFSI electrolyte membrane with a salt concentration of [27]:[1]. Since the T_g of PEO-LiTFSI is below freezing temperature (-40°C for [20]:[1] salt concentration[88]) it cannot be observed in this thermogram. An endothermic peak at 63°C was observed, which corresponded to the melting point for the PEO-LiTFSI electrolyte membrane. Since the melting point corresponds to the melting temperature of crystalline domains in the polymer electrolyte, the ionic conductivity should be significantly higher above this temperature. Chapter 4 will discuss the temperature dependence of the electrochemical properties of polymer electrolytes in further detail.

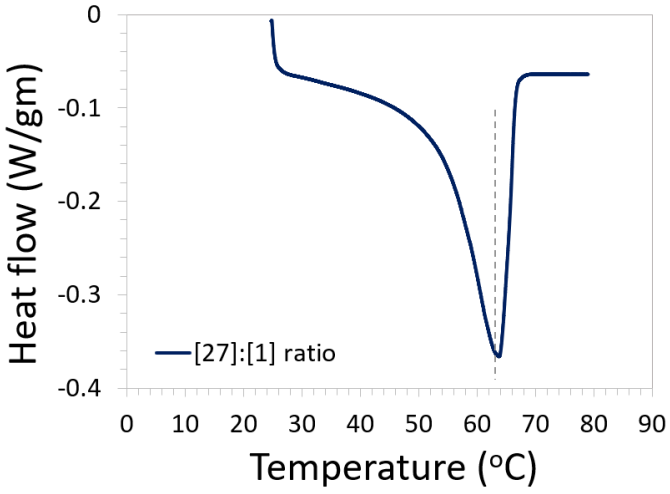

Figure 3.2 *DSC thermogram of a PEO-LiTFSI electrolyte membrane*

3.1.2 Lithium Lanthanum Zirconium Oxide (LLZO) solid ceramic electrolyte

Lithium Lanthanum Zirconium Oxide (LLZO) powder was synthesized by a solid-state synthesis method. The synthesized LLZO powder was processed into dense electrolyte membranes by rapid induction hot-pressing (RIHP). Before electrochemical characterization, the densified electrolyte membrane surface was treated to eliminate any surface impurities. The details of the synthesis, densification and surface preparation methods are discussed below.

3.1.2.1 Synthesis and powder processing

It was discussed in section 1.3.2.2 that Al and Ta aid the stabilization of higher ionic conductivity cubic phase in LLZO SE. Therefore, in this work, Ta-doped LLZO (LLZTO) was utilized with the formulation $Li_{6.5}La_3Zr_{1.5}Ta_{0.5}O_{12}$. For the synthesis of LLZTO powder Li_2CO_3 (Alfa Aesar, 99%), La_2O_3 (PIDC), ZrO_2 (Inframat Advanced Material^{TM}, 99.9%) and Ta_2O_5 (Inframat Advanced Material^{TM}, 99.9%) precursors were weighed out in stoichiometric amounts. 10 wt. % excess Li was added to compensate for Li loss during calcination and avoid formation of pyrochlore ($La_2Zr_2O_7$). The weighed precursors were wet mixed by roller milling with ethanol (solvent) and 2 mm in diameter zirconia balls (media) for 24 h. The precursor mixture was dried for 7 h under IR lamps, collected and passed through a 400 µm sieve to separate the media and avoids any agglomerates. The sieved powder was then cold-pressed into 10 g pellets of 25.4 mm diameter under a 19.61 kN force for 2 min. The cold-pressed pellets were calcined in an MgO boat at 1000°C for 4 h under flowing dry air atmosphere (1.75 $L \cdot min^{-1}$). The heating and cooling rates for calcination were 1.7 $°C \cdot min^{-1}$ and 4 $°C \cdot min^{-1}$, respectively. After calcination, the pellets were ground in an agate mortar and pestle and passed through a 75 µm sieve to obtain a uniform particle size distribution. This was followed by X-Ray Diffraction measurements for the phase purity analysis of the LLZTO powder.

3.1.2.2 Rapid Induction Hot-pressing

The calcined and sieved LLZTO powder was cold-pressed before sintering in a 12.7 mm stainless steel die under 200 MPa for ten minutes. To minimize die-wall friction effects during ejection, Li stearate was used as a lubricant. RIHP was used to densify cold-pressed LLZTO green bodies into dense LLZTO pellets (≥ 97% RD). For RIHP a copper coil (inductor) heats up the die which resides in the middle of the coil. For hot-pressing, ~5 g of cold-pressed LLZTO powder was loaded in a 12.7 mm diameter graphite die with alumina plungers under Ar atmosphere. The die is then placed in the middle of the inductor and hot-pressed at 1225 °C for 40 min at 47 MPa.[89] The hot-pressed pellets were then cut into 1.5 to 2 mm thick samples using a diamond saw with mineral oil as the cutting fluid. Samples were manually polished using a lapping fixture with 400, 600 and 1200 grit silicon carbide sandpaper to achieve parallel faces. Then the samples were wet polished to a 0.1 μm surface finish. The surface was cleaned with ethanol and acetone to remove any excess polishing fluid left on the surface after wet polishing.

3.1.2.3 Surface preparation

Sharafi *et al.*[90] demonstrated experimentally and via first-principles calculations that LLZO reacts with moisture and CO_2 on exposure to air to form a LiOH and a Li_2CO_3 interfacial layer. This interfacial layer resulted in a high Li-LLZO $R_{interface}$ due to poor Li wettability of the surface. Heat-treatment of LLZO under Ar atmosphere was suggested as a simple method to eliminate the surface impurities.[28] Immediately after wet polishing and cleaning, the LLZTO samples were heat-treated in an Ar-filled dry glove box (less than 0.5 ppm H_2O andO_2) to eliminate the surface impurities, before any electrochemical characterization.

3.1.2.4 Phase purity analysis

X-ray diffraction (XRD) (Rigaku Miniflex 600) was used to determine the crystal structure and phase purity of the LLZTO powder and hot-pressed samples. A Cu K_α X-Ray radiation source (λ=1.54 Å) operating at 40 kV and 20 mA was used. The measurements were collected between 15° to 65° 2θ angles with a step size of 0.02° and speed of 2°/min. Bragg's law was used to analyze the X-ray diffraction patterns. The Bragg's law calculates the angle where the scattered X-rays from the parallel planes of atoms of a sample constructively interfere to give a diffraction peak. It is given by the equation –

$$n\lambda = 2d\ sin\theta \tag{3.1}$$

where n is an integer (1, 2, 3, ...), λ is the wavelength of the incident beam (1.54 Å), d is the interatomic spacing, and θ is the angle of the diffracted beam. This equation is used to create an XRD pattern that plots intensity as a function of 2θ. The weight fraction of secondary phases was determined by applying Rietveld structural refinements to the XRD patterns.

3.1.2.5 Surface characterization

The surface of LLZTO was examined using Scanning electron microscopy (SEM, TESCAN RISE with a 10 kV accelerating voltage) for hot-pressed samples, polished samples, heat-treated samples and sample exposed to different liquid electrolytes. The details of the SEM will be discussed in the respective Chapters.

3.2 Electrochemical characterization

3.2.1 Electrochemical Impedance Spectroscopy

Electrochemical impedance spectroscopy (EIS) is a powerful characterization technique which can probe the physical transport phenomenon in bulk materials and interfaces in an

electrochemical cell. EIS applies a perturbation voltage over a broad range of frequencies (7 MHz to < 1 Hz) and measures the current response. A Nyquist plot is where the impedance at each frequency is plotted with its imaginary component (Capacitance and Inductance) on the y-axis and real component (Resistance) on the x-axis. Since an electrolyte in a Li metal battery blocks electronic transport, no inductance occurs in the impedance measurements under idealized conditions. The frequency response of the impedance relating to different materials or different physical transport phenomenon are dependent and thus characterized according to their electrical relaxation times or time constants. The relaxation time or time constant, τ, of each 'parallel RC (resistive/capacitive) element' in a cell is given by the product of R and C:

$$\tau = \mathrm{R} \cdot \mathrm{C} \tag{3.2}$$

In the frequency domain, RC elements are separable due to the relation shown in equation

$$\omega_{\max} \cdot \mathrm{R} \cdot \mathrm{C} = 1 \tag{3.3}$$

which holds at the frequency of maximum impedance, ω_{max}, in the impedance spectrum. Thus, it possible to relate the physical transport phenomenon with different RC elements on the Nyquist plot. The capacitance for different phenomena in an electrochemical cell such as bulk, grain boundary and electrode-electrolyte interface, surface layer formation, etc. can be found in Irvine *et al*.[91] After relating the RC element with the physical phenomenon, the ionic conductivity and area specific resistance can be commented on by using the equation

$$R = l/\sigma A \tag{3.4}$$

where R is the resistance (Ω) taken from the Nyquist plot, A is sample area (cm^2), l is the thickness of sample (cm) and σ is the conductivity of the sample (S/cm). EIS will be used to study different Li ion transport in different cell configuration throughout this thesis.

3.2.2 Trilaminar cell configuration

To decouple the $R_{interface}$ between a polymer electrolyte and LLZTO using electrochemical impedance spectroscopy (EIS) a trilaminar cell configuration using blocking electrodes was designed. The heat-treated LLZTO electrolyte was interposed between two polymer electrolyte membranes. The sandwiched structures were assembled between two 1.27 cm diameter current collectors (Au or Ni). A 100 kPa stack pressure was applied on the cells. The cells were heat conditioned to form the interface between the polymer electrolyte and LLZTO. For conditioning, the cells were heated to 80^{o}C on a hot stage and insulated using quartz wool. The temperature was tracked using two type-K thermocouples attached to the Ni pins to ensure that there was no gradient in temperature along the length of the cell. The impedance was tracked using EIS vs time until the cell impedance was stabilized. After conditioning, the cells were cooled to room temperature. Using EIS, the interfacial impedance between LLZTO and the polymer electrolyte was tracked vs temperature.

Chapter 4 Studying the Effects of Temperature and Pressure on Electrochemical Performance of a Polymer Electrolyte

4.1. Introduction

The demand for fossil fuel alternatives and increased electrification of the energy sector creates the impetus to develop higher performance energy storage systems.[92] Over the last two decades there has been a lot of improvement in Li-ion battery technology, but significant challenges remain. For example, there is an ever-increasing need to reduce cost (<$100 kWh), enhance safety, and increase performance (>1000 Wh/l, >500 Wh/kg, cycle life, and power density). One approach to improve energy density (> 1000 Wh/l) is to replace carbon-based anodes in Li-ion batteries with metallic Li.[12] However, stabilizing the Li metal/liquid electrolyte interface has proven difficult.[15,16] Currently, there are substantial efforts to develop solid-state electrolytes to physically stabilize the Li metal interface.[20,47,93] In this thesis, the promising SE $Li_{6.5}La_3Zr_{1.5}Ta_{0.5}O_{12}$ (LLZTO) was explored due to its high ionic conductivity at room temperature (RT), and its ultra-low interfacial resistance and stability with Li.[28,94] However, the implementation of SEs leads to cycling instabilities due to the formation of highly resistive solid-solid interfaces.[64,65]

The approach to overcome the incompatibility is the interposition of a GPE between the between SE and cathode or catholyte. A GPE polymer electrolyte will be comprised of a polymer matrix with entrained LE. For the hybrid approach to be effective, it is important to understand the factors that control the kinetics and stability of bulk polymer and polymer/electrode interfaces. In

this study, we hypothesize that temperature and stack pressure affect the stability and kinetics of the polymer electrolyte and electrode-polymer electrolyte interface. The effects of pressure and temperature were studied, since the physical properties of most polymer electrolytes are highly sensitive to these external variables.[95,96] However, though there are myriad SPE that are well understood in terms of their synthesis and conductivity[97–105], there have not been many studies that correlate the coupled effects of external variables (pressure, temperature, electrode type) with the electrochemical properties of the polymer and electrode-polymer interface.

Polyethylene oxide/LiTFSI was used as a model SPE, because it is well-understood and relatively easy to process. For the cell, the effects of temperature and pressure were studied on a Li/PEO-LiTFSI/Li system as the transport mechanisms in this configuration are well-studied. Previous studies discuss the cycling behavior of PEO-LiTFSI electrolyte membranes at different current densities and at 90^{o}C. They also study the Li dendrite penetration and evolution during cycling by correlating electrochemical data with in-situ optical imaging.[106,107] The goal of this work was similar to the work of Rosso *et al*., however, we combined dc cycling, electrochemical impedance spectroscopy (EIS), and optical analysis to determine how temperature and stack pressure affect the kinetics and stability of PEO-LiTFSI and Li/PEO-LiTFSI interface. As will be discussed, we believe pressure likely affects the physical contact area at the Li-polymer electrolyte interface, thereby affecting interface resistance.[108] In addition, temperature affects both kinetics and mechanical properties, as the crystallinity and stiffness of the SPE decreases with increasing temperature. Thus, it is likely that both pressure and temperature also affect the CCD (Critical Current Density) or the maximum tolerable current density subject to which Li metal dendrites do not cause failure during charging. The overarching goal of this work is to establish an

experimental platform to study the effects of stack pressure and cell temperature on the electrochemical properties of the polymer and the polymer/electrode interface.

4.2. Experimental Section

4.2.1. PEO-LiTFSI membrane fabrication and characterization

The PEO-LiTFSI membranes were fabricated using solution casting discussed in detail in Section 3.1.1.1. The electrolyte membranes were characterized using Raman spectroscopy and Energy Dispersive Spectroscopy (EDS). Raman spectroscopy was conducted to characterize the fabricated membranes and to determine if any residual moisture and solvent was present. Several observations were made from the Raman spectra for pure acetonitrile (ACN), the PEO-LiTFSI solution in ACN, and dried PEO-LiTFSI film (Figure 4.1 a). First, after drying the membrane, it was apparent that all the ACN solvent was removed as the CN peak was no longer detectable. Second, the absence of the OH stretching frequency (3100-3600 cm^{-1}, as seen in literature) peak confirms that no moisture was detected. Third, in the PEO-LiTFSI solution spectrum, no peaks were associated with pure PEO suggesting that the PEO was completely dissolved. Scanning electron microscopy (SEM) with EDS was performed to characterize chemical homogeneity (Hitachi: S3500N SEM w/ EDAX). Based on the SEM analysis (Figure 4.1 b) it was apparent that overall the membrane was uniform except for some pores that formed on the film surface. Since the electrochemical testing was done above the melting temperature under stack pressure, we believe that all the pores had been eliminated and hence the porosity did not affect the electrochemistry. Lastly, SEM/EDS compositional analysis (Figure 4.1 c), indicated the dispersion of S and F in the membrane. Since S and F were present in the salt, we can conclude that the salt distribution was relatively uniform, which avoided any local variation in ionic conductivity.

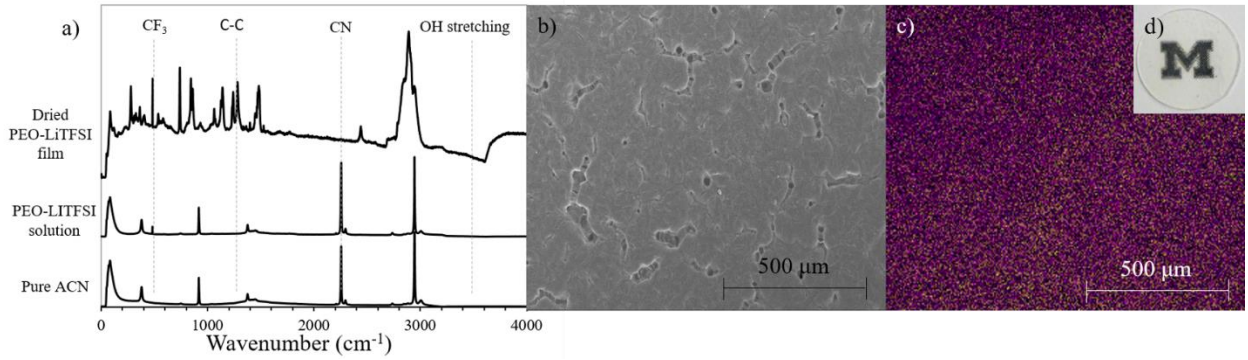

Figure 4.1 *a) Raman spectra for the polymer electrolyte membrane; b) SEM image of the polymer electrolyte membrane; c) EDS image showing the homogeneous distribution of S (pink) and F (yellow) (which comes from the salt) on the membrane; d) Optical image of the 12.7 mm diam. transparent membrane.*

4.2.2. Mechanical properties of PEO-LiTFSI

The membrane mechanical properties were characterized using acoustic impulse excitation. To measure the elastic modulus, a longitudinal wave transducer (5073PR with M110, Olympus NDT, Tokyo, Japan) was placed on a membrane using mineral oil as the coupling medium. An oscilloscope (PicoScope 2207a, Pico Technologies, Cambridgeshire, UK) was used to measure the longitudinal wave velocity by dividing the thickness of the membrane by the time taken by the wave to travel through it. With these data, the elastic modulus was determined by using equation 4.1[109] –

$$E = v_l^2 \rho \frac{(1+\nu)(1-2\nu)}{(1-\nu)} \quad (4.1)$$

where E is the elastic modulus, v_1 is the velocity of the longitudinal wave, ρ is the density and ν is the poisson's ratio. The value of poisson's ratio was taken as 0.24 from literature.[110] The Shear modulus (G) is calculated by using equation 4.2[109] –

$$G = \frac{E}{2(1+\nu)} \quad (4.2)$$

4.2.3. Electrochemical characterization of the PEO-LiTFSI

4.2.3.1. Studying the temperature dependence of PEO-LiTFSI electrochemical properties

Electrochemical impedance spectroscopy (EIS) was used to characterize the effect of temperature, pressure and electrode type on bulk and interfacial Li/PEO-LiTFSI ionic transport. The cells were assembled in an argon filled glove box (0.5ppm O2 and H2O) in a load frame fixture (Figure 4.2). The cell was prepared by sandwiching a PEO-LiTFSI electrolyte membrane between two 0.5 inch diameter 100μm thick Li foil (Alfa Aesar) disks. The Li foil was cleaned by scraping the oxide impurities from its surface immediately before cell assembly. The sandwiched structure was assembled between two 0.5 inch diameter Ni pins (current collectors) which were aligned in place using three PTFE pieces. Stack pressure was applied on the pins using a load cell (Imada Inc.). The cell was kept horizontally on a hotplate and then well insulated using quartz wool for temperature measurements. The temperature was tracked using two k-type thermocouples to ensure that there no gradient in temperature along the length of the cell. The cell impedances were calculated from the EIS data between 100mHz to 7MHz using a potentiostat/galvanostat (Bio-logic VMP300). A stack pressure of 100kPa was maintained while characterizing the effect of temperature between 30^{o}C and 100^{o}C. It should be noted that before the measurements the cells were heat-conditioned under stack pressure. This ensured that the measurements were not affected by interfacial contact.

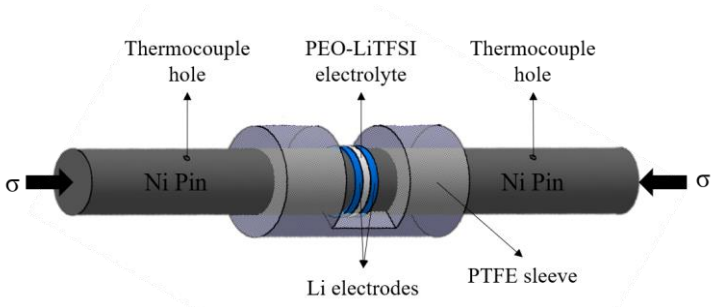

Figure 4.2 *Cell configuration used to characterize electrochemical behavior under constant stack pressure (σ = 100 kPa) at various temperatures*.

4.2.3.2. Studying the stack pressure dependence of PEO-LiTFSI electrochemical properties

The effect of stack pressure at three different temperatures (60°C, 80°C, and 100°C) on the bulk and interfacial resistance of Li/PEO-LiTFSI/Li cells was studied. Cells were assembled in a similar configuration as was used for temperature measurements but instead of a load cell, the stack pressure was applied using an Instron compression unit (Figure 4.3) where the stack pressure could be varied in steps during electrochemical testing (Instron 5944 tension/compression testing unit, inside an argon filled glove box (0.5ppm O_2 and H_2O)). A heating tape was wrapped around the cell from heating the cell to testing temperature and then it was covered by quartz wool for insulation. The cells were galvanostatically cycled at 0.1 mA/cm^2 for each temperature with varying stack pressure (between 0 to 900 kPa) and EIS measurements were taken at the end of each cycle. The contact area between Li and PEO-LiTFSI remains constant while increasing stack pressure as the Li does not creep beyond the area of the current collectors.

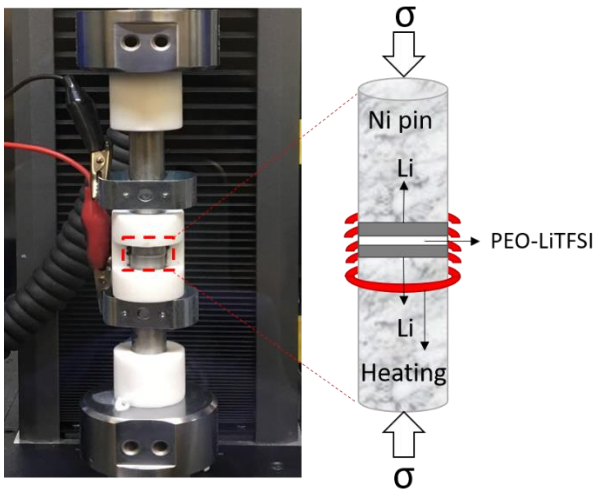

Figure 4.3 *Cell testing apparatus used to characterize electrochemical behavior under constant temperature at varying stack pressure using an Instron housed in an Ar-filled glovebox.*

4.2.3.3. Studying the temperature dependence of PEO-LiTFSI critical current density (CCD)

To study the effect of temperature on CCD, direct current (DC) cycling on Li/PEO-LiTFSI/Li cells was conducted for three different temperatures; 60°C, 80°C, and 100°C. The cells were first preconditioned by cycling at ±0.01 mA cm^{-2} for 30 minutes to condition the interface[111] between the Li electrode and the polymer at the respective test temperature (60°C, 80°C, or 100°C). The cells were galvanostatically cycled symmetrically at varying current densities between ±0.01 mA cm^{-2} and ±10 mA cm^{-2}. EIS data was collected after each step to calculate the bulk and interfacial resistances.

4.2.3.4. Studying the electrode type dependence of PEO-LiTFSI electrochemical properties

Vapor deposited Li was used to minimize the contamination of the Li metal/polymer electrolyte interfacial resistance. The change in Li/PEO-LiTFSI interfacial resistance as a function

of temperature (with negligible stack pressure) and pressure (at 80°C) was studied for cells assembled with Li foil and vapor deposited Li as electrodes.

4.2.3.5. Visualization cell configuration

For *operando* visualization, an in-plane sample geometry was used. Two 8.0 mm long parallel Li electrodes (5 µm thick) separated by 1 mm were vapor-deposited in a glovebox-integrated thermal evaporation chamber (Angstrom Engineering), onto the same side of a 500 µm thick PEO film by shadow masking. Inside of an Ar glovebox, this film was placed onto a thin PTFE film with no stack pressure and heated until the temperature of the film reached 80 ℃. The electrodes were contacted using tungsten microprobes connected to a Bio-logic SP-200 potentiostat. The cell was then cycled at increasing current density from 0.1 mA/cm^2 to 5.0 mA/cm^2. Current density was defined by the current divided by the cross-sectional area of the electrolyte film between the two electrodes. Images were captured using a 75 mm c-mount lens (Fujinon), 100 mm extension tube, and 5 Megapixel camera (Amscope).

4.3 Results and Discussion

4.3.1. Mechanical properties characterization of PEO-LiTFSI membranes

Figure 4.4 shows the longitudinal wave propagation data captured during the acoustic analysis on the PEO-LiTFSI membranes at 40°C. By using equations 4.1 and 4.2, the elastic and shear moduli were determined to be 0.5 GPa and 0.2 GPa, respectively at 40°C. There are two implications drawn from these results. First, when used as a catholyte, a higher elasticity of the polymer in the GPE would be advantageous in maintaining intimate contact with the cathode. This can be evaluated by measuring the elastic modulus of the polymer. Second, according to the Newman and Monroe criterion, an isotropic electrolyte should suppress Li dendrite initiation[112] if

the shear modulus is at least twice that of metallic Li (G_{Li} = 4.2 GPa[113]). Since the shear modulus of PEO-LiTFSI electrolyte is less than that of Li, the electrolyte should not exhibit resistance to dendritic initiation according to this criterion.

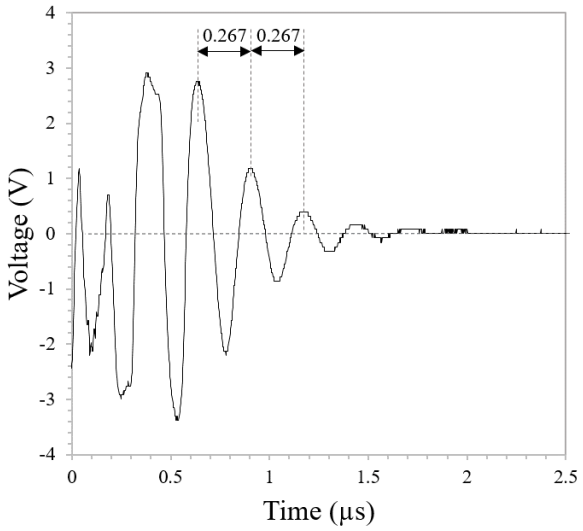

Figure 4.4 *Longitudinal acoustic spectrum of the PEO-LiTFSI membranes at 40°C. The time between reflections was 0.267μs, which was used to determine the wave velocity and the elastic properties.*

4.3.2. Effect of Temperature on Li/PEO-LiTFSI/Li symmetric cell impedance

The electrochemical transport properties of symmetric Li-PEO/LiTFSI-Li cells were characterized using EIS between 30 and 80°C (Figure 4.5). From Figure 4.5, several observations can be made. First, the EIS data at 30°C (Figure 4.5 a) presents two distinct impedance components (represented by the two semi circles), one in the higher frequency range corresponding to the bulk impedance and the other in the lower frequency range corresponding to the interfacial impedance. The Nyquist plot was modeled using an equivalent circuit (Figure 4.5 a) to determine the separate impedance elements where R_{bulk} is the resistive component and CPE is the constant phase element. The fitted capacitance value for bulk impedance was $1.3*10^{-9}$F and for interfacial impedance

$0.78*10^{-6}$F, which is in accordance with the values reported in literature for these physical phenomena.[91]

At 80°C (above the melting point of the polymer) it is known that crystalline domains no longer remain, thus the semi-circle for bulk resistance decreases to an undetectable value as shown in Figure 4.5 b.[114] The sum of the bulk and uncompensated resistance was given by point X (Figure 4.5 b). The capacitance calculated for the lower frequency semi-circle was $0.78*10^{-6}$F, confirming that it corresponded to interfacial impedance. The bulk conductivity of the membranes was measured to be on the order of 10^{-4} S/cm at 60°C and 10^{-3} S/cm at 80°C and 100°C. Figure 4.5 c shows the variation of conductivity (σ) of the PEO-LiTFSI electrolyte between 30 to 100°C. It was observed that conductivity exhibits two temperature regimes for which the activation energies were calculated using the Arrhenius equation equation 4.3 –

$$\ln(\sigma T) = \ln(\sigma_0) - (E_a/kT) \quad (4.3)$$

where T is the absolute temperature, E_a is the activation energy, and k is Boltzmann's constant. By fitting this equation to the two regimes, the activation energy was calculated for the lower temperature range to be 1.26 eV and for the higher temperature range to be 0.37eV. Liu *et al.*[47] reported the activation energy in the lower temperature range to be 1.195 eV and in the higher temperature range to be 0.385 eV, and the conductivity at 60°C to be in the order of 10^{-4}. Thus, we believe that the values measured in this study are in accordance with previously reported values. This transition in regimes occurs around the melting temperature of the polymer membrane due to the melting of the crystalline domains, which increases chain mobility and thus bulk conductivity.[115] Similar to bulk resistance, the interfacial resistance decreases with increasing temperature, which may be attributed to better wetting of the polymer film by Li and improved

kinetics. However, unlike bulk transport, there is a single activation energy associated with interfacial Li-ion transport in the temperature range of 30 to 80°C. This implies that Li/PEO-LiTFSI interfacial charge transport does not depend on the bulk charge transport mechanism.

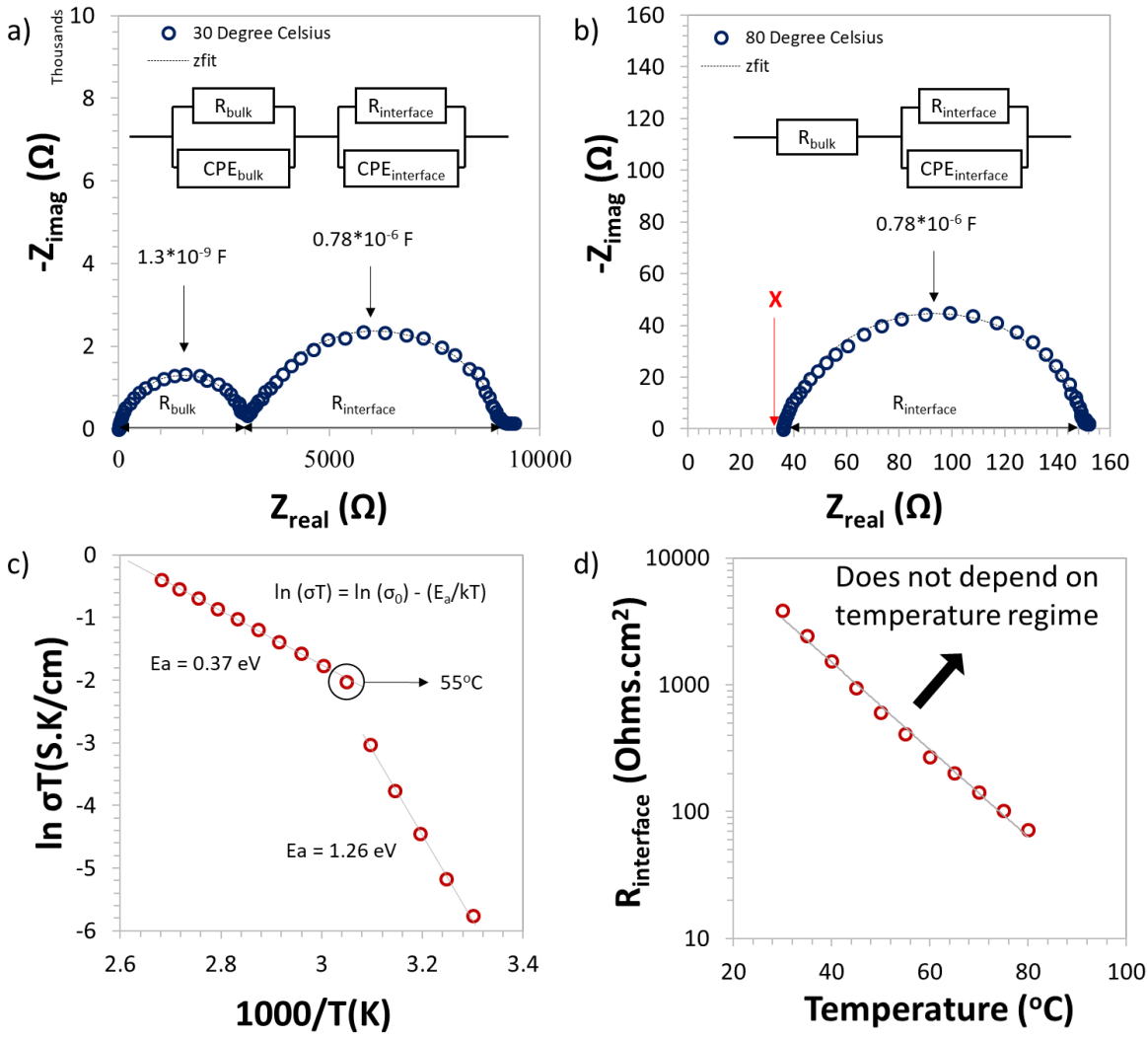

Figure 4.5 *a) Representative Nyquist plot of a Li/PEO-LiTFSI/Li cell at 30°C b) Representative Nyquist plot of a Li/PEO-LiTFSI/Li cell at 80°C; The marker (o) represents the experimental data in a) and b) and the dotted line (···) represents the equivalent circuit modeling data of Li/PEO-LiTFSI/Li cells c) Arrhenius plot of a polymer membrane indicating a dramatic change in transport at approximately 55°C. d) Temperature dependence of Li/PEO-LiTFSI interfacial resistance*

4.3.3 Effect of Stack Pressure in a Li/PEO-LiTFSI/Li symmetric cell on interfacial kinetics

The effect of stack pressure on bulk and interfacial resistance was characterized on Li/PEO-LiTFSI/Li cells (Figure 4.6). Several observations can be made from Figure 4.6. From Figures 4.6 a and 4.6 b it was apparent that the interfacial resistance exponentially decreased with increasing stack pressure approaching an asymptote at 400 kPa and 200 kPa, respectively. We believe that stack pressure plays an important role during DC cycling as it helps facilitate an increase in electrochemically active contact area, which leads to a reduction in electrode/electrolyte interface resistance. The minimum stack pressure required to establish an optimized interface is defined as the critical stack pressure, at and above which interfacial resistance no longer varies with increasing pressure as the electrode makes maximum active interfacial contact with the electrolyte. The critical stack pressure would also be dependent on operating cell temperature since the viscosity of the polymer and Li are temperature dependent. Hence, based on the asymptotic behavior in Figure 4.6 a and 4.6 b, 400 kPa and 200 kPa were determined to be the critical stack pressure for the Li/PEO-LiTFSI interface at 60 and 80°C, respectively. Unlike at 60 and 80^{o}C, at 100^{o}C (Figure 4.6 c), initially the interfacial resistance exponentially decreased with increasing stack pressure approaching an asymptotic value. However, at approximately 550 kPa at 100^{o}C, a sudden drop in cell resistance was observed. There can be two possible reasons behind the sudden drop: 1) At 100^{o}C and 550 kPa stack pressure Li metal dendrites start growing exponentially, increasing the surface area and hence the interfacial resistance drops. 2) At 100^{o}C and 550 kPa stack pressure it is possible that the surface layer between Li and PEO mechanically fails, exposing Li metal to the PEO surface and hence decreasing the resistance.[115] Therefore, it is critical not to exceed the stack pressure where any of the above failures occur, especially at elevated temperature.

This would be true for any polymer/electrode system. It was also observed that the bulk resistance decreased with increasing stack pressure, consistent with an increase in interfacial contact and decrease in membrane thickness.

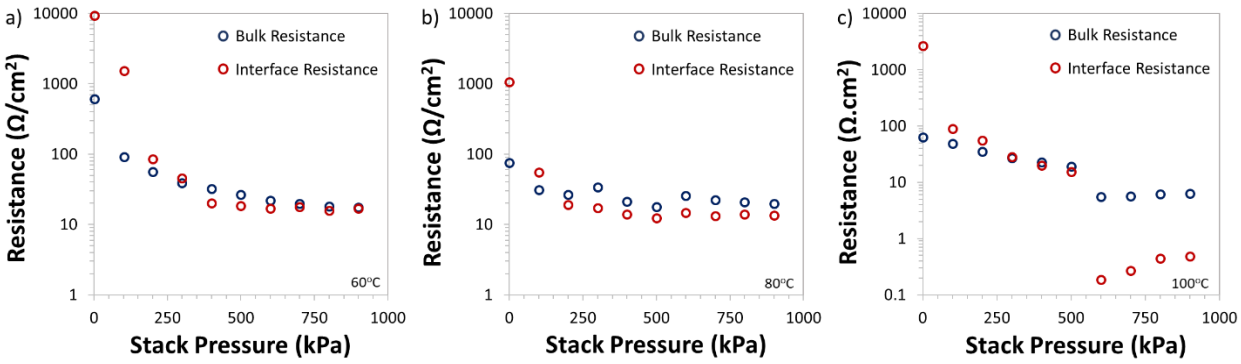

Figure 4.6 *Variation of bulk and interfacial resistance with stack pressure of a typical Li/PEO-LiTFSI/Li cell during cycling at 0.1mA/cm^2 at a) 60^{o}C b) 80^{o}C c) 100^{o}C.*

Similar to the interfacial resistance, the capacitance associated with the Li/PEO-LiTFSI interface should also be affected by the changing active contact area with increasing stack pressure. Thus, the effect of stack pressure on the Li/PEO-LiTFSI interface capacitance was evaluated at the three different temperatures (60, 80 and 100°C). It was expected that with the increasing contact area with stack pressure, the capacitance should also increase. It can be observed from Figure 4.7, that the capacitance for Li/PEO-LiTFSI does increase with stack pressure for all three temperatures, however, the change is not dramatic. It is possible that the change in capacitance is compensated by a changing frequency dependence with temperature.

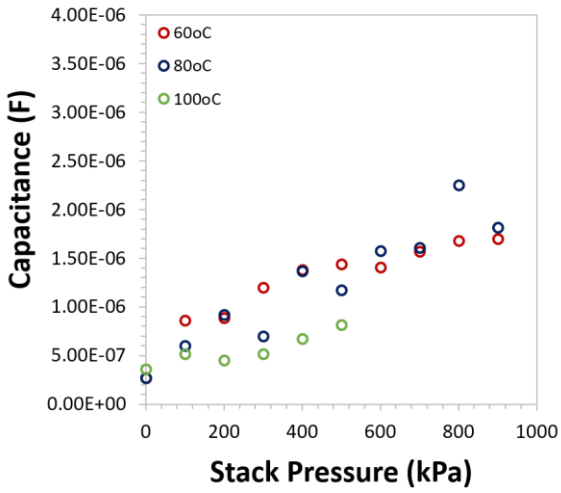

Figure 4. 7 *Variation in capacitance of the Li/PEO-LiTFSI interface with increasing stack pressure at 60°C, 80°C and 100°C.*

4.3.4. Effect of temperature on the critical current density (CCD)

The maximum tolerable current density of the Li-PEO/LiTFSI interface (CCD) was measured as a function of temperature. We have observed that the CCD of a Li metal interface against ceramic $Li_7La_3Zr_2O_{12}$ electrolytes increases with temperature[116], thus we hypothesized that the same will hold true for the Li-PEO/LiTFSI interface. First, in Figures 4.8 a, b, and c the voltage profiles followed Ohmic behavior ($V=iR_{cell}$) below 0.5 mA/cm^2 for each temperature, indicating the interface resistance was relatively unchanged during DC cycling. However, at $\geq$ 0.5 mA/cm^2, the profiles then deviated from Ohmic behavior at each temperature, possibly indicating the onset of dendritic growth. We believe, that current density for onset of dendritic growth is invariant of temperature (above the T_m) because of its lack of resistance to dendritic growth owing to its low shear modulus. Second, in Figure 4.8 d, the cell resistance suddenly dropped at 0.5mA/cm^2 for all the three temperatures. We believe that the drop in resistance occurs under conditions that lead to dendrite growth, thus decreasing the effective distance between the two electrodes decreasing the bulk resistance, and hence decreasing the voltage.[106] Even though the dendrite growth initiated at 0.5 mA/cm^2, no hard short was observed up to 10 mA/cm^2. Rosso *et al.* observed similar behavior

referring to 'burning' of the polymer around the surface of the dendrites.[107] There it was shown that the presence of the burnt polymer increases resistance between the dendritic and the Li electrodes, which prevents the potential from dropping to zero. To further investigate and better understand the Li metal propagation in PEO-LiTFSI, *Operando* optical imaging was conducted (discussed in Section 4.3.6) using a customized visualization cell. Clearly, the dramatic drop in potential at $\geq$ 0.5 mA/cm^2 was indicative of the onset of dendritic growth.

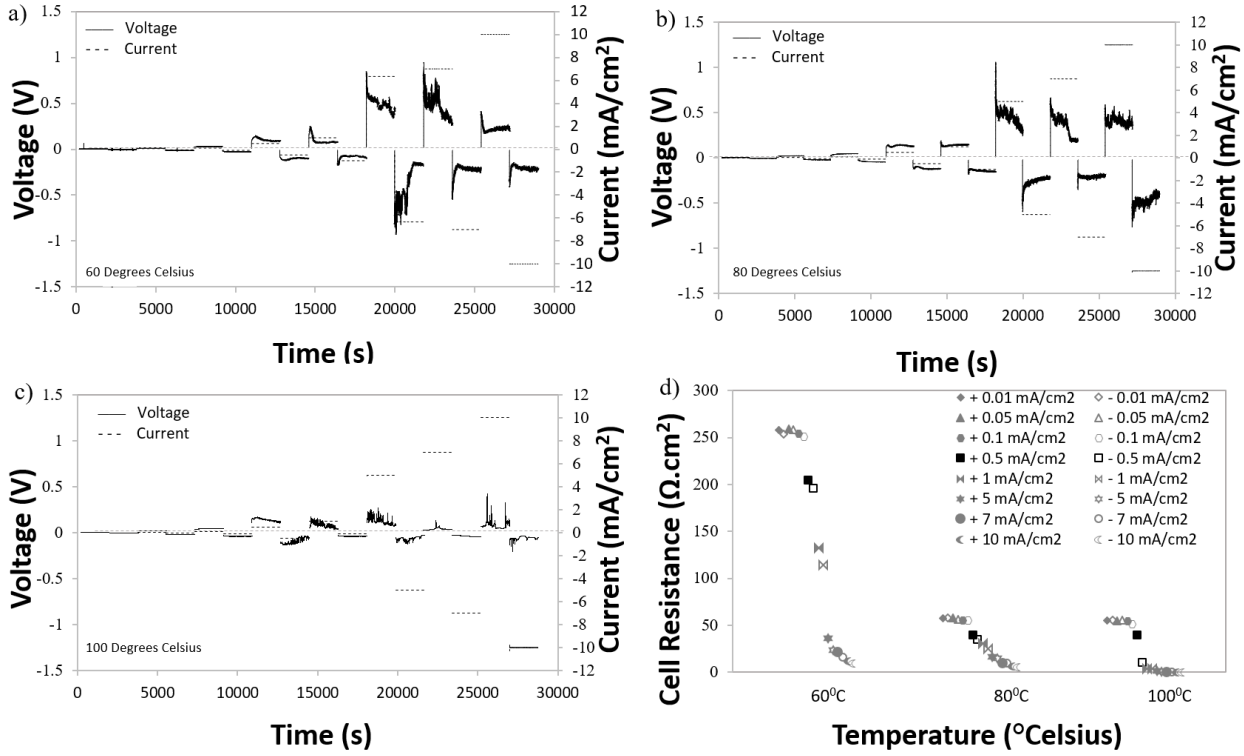

Figure 4.8 *Galvanostatic cycling of Li/PEO-LiTFSI/Li cells from ± 0.01 mA/cm^2 to ± 10 mA/cm^2 at: a) 60^{o}C, b) 80^{o}C, and c) 100^{o}C. d) Variation of total cell resistance in Li/PEO-LiTFSI/Li cells with current density at 60^{o}C, 80^{o}C, and 100^{o}C*

4.3.5. Effect of the electrode type on electrode/electrolyte interfacial properties

To enable consistent and low interfacial resistance, vapor deposited Li anodes were compared to Li foil electrodes. Figure 4.9 shows the variation in Li/PEO-LiTFSI interfacial resistance with temperature and stack pressure, which was measured using EIS. The resistances

were calculated by fitting an equivalent circuit model to the complex impedance plots. Figure 4.9 a shows the representative Nyquist plots at 80^{o}C for both vapor deposited Li and Li foil electrodes. A decrease of 67% in interfacial resistance was observed at 80^{o}C with Li vapor deposited electrodes as compared to Li foil electrodes (Figure 4.9 a) and the same drop was observed for every other temperature (Figure 4.9 b). The decrease in interfacial resistance for the vapor deposited Li was likely due to improved wetting[28,108] of the polymer electrolyte by the Li. We would expect the current density for the onset of dendritic growth to increase, which would affect the CCD, as a more uniform interface and increased contact reduces hot spots (centers for dendrite nucleation) for dendritic growth and is likely to have more uniform current density. From Figure 4.9 b it can be observed that interfacial resistance did not vary with stack pressure when vapor deposited Li was used as the electrode. Hence, the critical stack pressure with vapor deposited lithium was much lower in comparison to Li foil. Due to the precisely controlled nature of thin film deposition, we hypothesize that vapor deposition will result in increased contact area compared to Li foil even at low values of stack pressure.

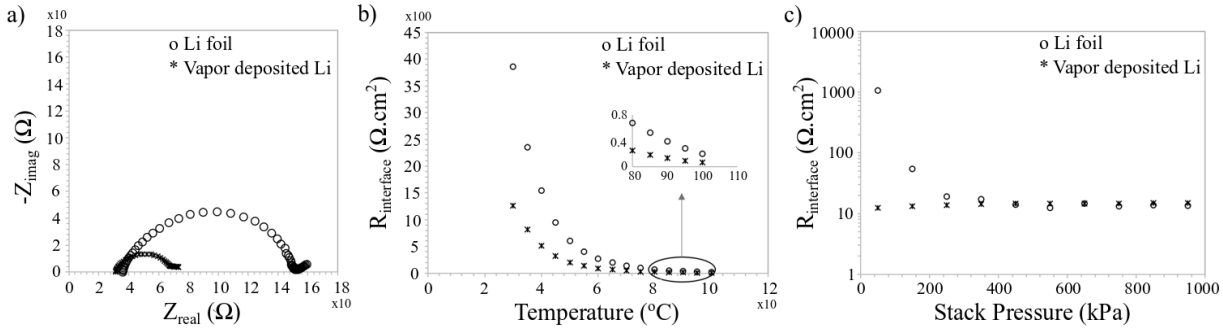

Figure 4.9 *a) Representative Nyquist plot of a Li/PEO-LiTFSI/Li cell at 80^{o}C for lithium foil electrodes (o) and for vapor deposited lithium (*); b) Variation of Li/PEO-LiTFSI interfacial resistance with temperature for lithium foil electrodes (o) and for vapor deposited lithium (*); c) Variation of Li/PEO-LiTFSI interfacial resistance with pressure (at 80^{o}C) for lithium foil electrodes (o) and for vapor deposited lithium (*).*

4.3.6. Visualization of dendritic growth

To better understand how Li metal penetrated the polymer electrolyte membrane during shorting, a customized *operando* visualization cell[117] was used to capture optical images during dc cycling (Figure 4.10).[106,107] From Figure 4.10, several observations were made. Compared to Li foil electrodes (0.5 mA/cm^2 at 80^{o}C), the onset of dendritic growth was observed at a higher current density (Figure 4.10 a) using vapor deposited Li electrodes (1 mA/cm^2 at 80^{o}C). This supported the hypothesis that increased contact and a more uniform interface would result in increased current density for Li metal penetration. The initiation of dendrite growth was observed in the *operando* visualization cell with vapor deposited Li at 1 mA/cm^2 (Figure 4.10 c). The dendrites resembled fractal morphology as was observed in literature.[106] No visible Li dendrites were observed at current densities < 0.5 mA/cm^2, which corresponded to Ohmic and consistent voltage behavior in the polarization curve (Figure 4.10 a). However, at 5 mA/cm^2, the rate of growth of dendrites was much higher (Figure 4.10 d) in comparison with 1mA/cm^2 (Figure 4.10 c). In Figure 4.10 a it was also observed that the cell reached the cut-off voltage (5V) quickly at 5 mA/cm^2. We believe that the cell reached the upper bound cut-off voltage as a result of Li depletion on the electrode undergoing stripping/oxidation, since no stack pressure was applied.

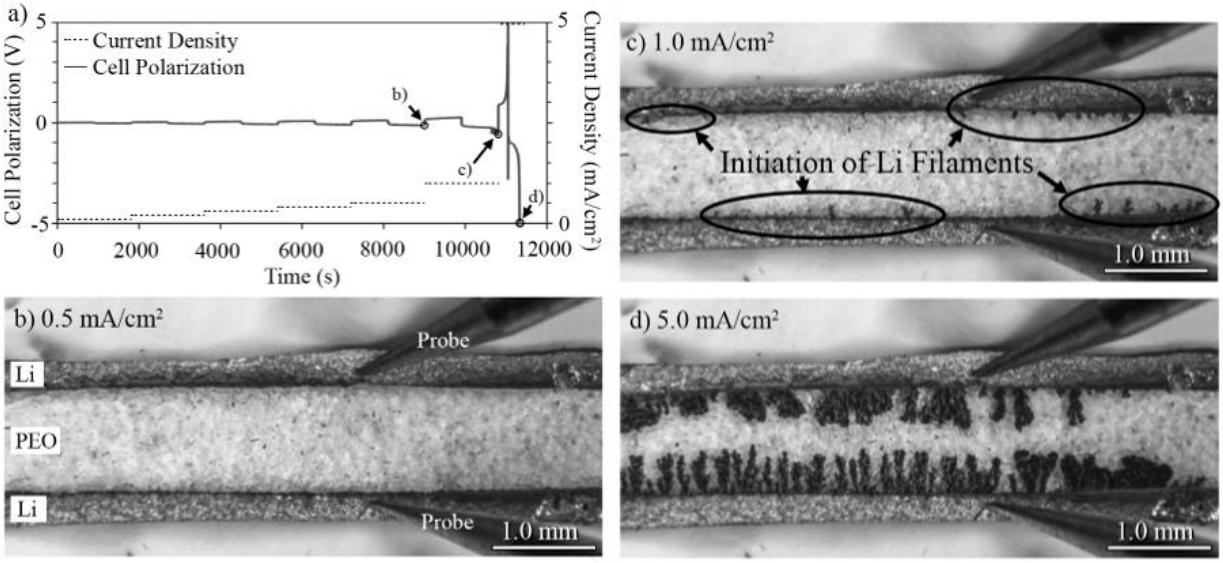

Figure 4.10 *a) Galvanostatic cycling of Li/PEO-LiTFSI/Li cells from 0.01 mA/cm^2 to 5 mA/cm^2 at 80^{o}C; b) Vis cell image of the cell at the end of 0.5 mA/cm^2 cycling step showing no signs of dendritic growth; c) Vis cell image of the cell at the end of 1 mA/cm^2 cycling step showing initiation of dendritic growth and d) Vis cell image of the cell at the end of 5 mA/cm^2 cycling step showing the structure of dendrites.*

4.4. Implications

Observations from this study could have implications for the successful implementation of GPEs as catholytes. First, temperature affects both kinetics and mechanical properties of the polymer electrolyte, as its crystallinity and stiffness decrease with increasing temperature. However, the activation energy for the bulk Li-ion transport changes above the melting temperature of the polymer which is not the case for interfacial transport. It is important to remember that with a GPE the polymer matrix holds the liquid electrolyte, which is responsible for the Li-ion transport. The closer the temperature is to the melting temperature of the polymer the lower is the liquid electrolyte retention capacity of the polymer. Thus, the thermal properties of the polymer would play an important role while selecting the polymer for the GPE. Second, the elastic modulus of the GPE would be important to maintain interfacial contact between the

polymer and the cathode during charging/discharging related volumetric changes. Third, it was shown that stack pressure plays an important role for the interfacial kinetics and cell polarization, as it helps to maintain an intimate contact between the electrode and the electrolyte. The minimum stack pressure required to establish an optimized uniform interface is defined as the critical stack pressure. Lastly, it is critical not to exceed the stack pressure where a mechanical failure of any electrode/electrolyte interfacial layer can occur.

4.5. Conclusions

In this study we evaluated the effects of external variables on kinetics and stability of the solid polymer electrolyte and its interface with Li metal. From the observations made it was concluded that kinetics of bulk polymer was majorly dependent on temperature. The conductivity of the polymer increased with temperature, with 10^{-4} S/cm at 60°C and 10^{-3} at 80 and 100°C, however, it there was a sharp transition near the melting temperature of the polymer. The kinetics of the electrode/electrolyte interface were strongly dependent on temperature, pressure and electrode type while the stability was independent of temperature. First, we observed that with an increase in temperature the interfacial resistance was reduced from 3000 Ohm.cm^2 to 30 Ohms.cm^2 (100 kPa stack pressure) indicating improvement in interfacial kinetics, however, there was no sharp transition observed for Li-ion at the electrode/electrolyte interface. Second, it was shown that a critical stack pressure (pressure at and above which the interfacial resistance is invariant with increasing pressure) was required to establish an optimized interface between an electrode and PEO-LiTFSI electrolyte. The critical stack pressure evaluated at 60 and 80^{o}C, was 400 kPa and 200 kPa respectively where the interfacial resistance was reduced to 20 Ω.cm^2. Third, we observed a 67% drop in interfacial resistance and double current density for onset of Li metal penetration (1mA/cm^2) while exploring the method of incorporation of Li (vapor deposition vs Li foil

adhesion). We believe that method of incorporation likely affected wetting and contact between the electrode and electrolyte, which significantly improved cell performance.[28,108] Fourth, a non-ohmic behavior was observed to start at 0.5 mA/cm^2 for 60, 80 and 100^{o}C. Later, with the assistance of a novel *operando* visualization cell it was shown that the non-ohmic behavior observed in the electrochemical data was indicative of Li dendrite initiation and propagation. We believe that temperature independence of the current density for Li metal initiation could be due to the low shear strength of PEO-LiTFSI membranes which cannot resist dendritic growth. Overall, the correlations and observations made in this study are useful in understanding factors that affect the kinetics and stability of solid-state electrolytes. We believe the findings will help maximize the rate at which solid-state batteries incorporating SPEs can be safely charged and discharged.

4.6. Acknowledgments

We would like to acknowledge the support from Robert Bosch LLC, Research and Technology Center, Sunnyvale, California, USA for this project. Arushi Gupta synthesized and characterized the PEO-LiTFSI electrolyte and fabricated and tested the electrochemical and mechanical properties of the solid-state cells. Nathan Craig and Jake Christensen provided insight in the analysis and interpretation of electrochemical data. Eric Kazyak and Neil Dasgupta performed the vis cell experiments and helped interpret the DC electrochemical data. Jeff Sakamoto assisted in the design of experiments, interpretation of data, and manuscript preparation.

Chapter 5 Understanding the Factors Controlling the Polymer/LLZTO Interfacial Kinetics

5.1. Introduction

The interest in increasing battery energy density has created the impetus to supplant carbon-based anodes in Li-ion batteries with metallic Li.[12] However, side reactions and morphological instability that occur during cycling Li in liquid electrolyte has impeded progress to this end.[13,17,118] One approach to enable this transition is to physically stabilize Li using a solid-electrolyte.[16] Most promising candidates actively researched for solid-electrolytes are sulfides[119,120], ceramic oxides[20,62,121] and polymers.[122,123]

LLZO, a ceramic oxide consisting of the garnet crystal structure, has shown great potential as a solid-electrolyte owing to its high ionic conductivity (1 mS/cm) and stability against lithium; however, difficulty in fabricating LLZO membranes and there incompatibility with cathodes has slowed maturation.[24] On the other hand, polymer electrolytes are relatively easy to process, but have an inherently low ionic conductivity at room temperature. Thus, there is interest in combining the two electrolytes in the form of LLZO-polymer composites (CPE) and/or LLZO-polymer bilaminar layers where the polymer is used as a catholyte. PEO/Lithium bis(triflouromethanesulfonyl)imide (PEO-LiTFSI)[98–102] is a good model system to be used as the polymer electrolyte as it is well researched and has desirable properties. Even though there are few examples of studies using the bilaminar configuration, there have been several reports on the development of LLZO-PEO composites (CPE). In the CPE, LLZO with higher ionic conductivity, acts as the primary conductive phase and PEO acts as the percolative network connecting LLZO particles and adding benefit of ease of fabrication.[124–130] Table 5.1 reports the CPE ionic

conductivity of varying concentration from literature. It was observed that the conductivity of PEO did increase with the addition of LLZO. However, contrary to the rule of mixtures, the CPE with lower volume fraction of LLZO had a higher ionic conductivity than compositions with higher fraction of LLZO. Hence, it was inferred that contribution from Li-ion conductivity of LLZO to the total conductivity of CPE was negligible. The increase in conductivity at lower volume fractions was due to LLZO particles disrupting PEO crystallinity. The goal of this study was to understand the transport mechanism(s) that govern the transport of Li ions between LLZO and PEO. To investigate this, we started with a CPE and considered the possible ionic pathways at high fractions of LLZO.[126] There are three possible ionic pathways as illustrated in Figure 5.1 a: (1) through PEO-LiTFSI, (2) through PEO-LiTFSI and LLZO or/and (3) through LLZO.[131] Considering that typical composite studies consist of relatively low volume fractions of LLZO, pathway 3 cannot be the lowest resistance path. Next, if pathway 2 was predominant, the conductivity would increase with increasing fraction of LLZO, but based on the findings in Figure 5.1 b, this is typically not the case. We believe that the ionic transport across the PEO-LiTFSI/LLZO interface was significantly more resistive than the resistance through PEO-LiTFSI and the dominant ionic conduction pathway was pathway (1). Thus, we believe there is a need to understand the factors that control ionic transport across polymer-ceramic interfaces to enable Li-ion transport between LLZO and a polymer electrolyte. If successful in improving the ionic transport at the LLZO-polymer interface, it is possible to enable pathways 2 in a CPE and/or introduce a polymer catholyte in combination with LLZO solid electrolyte.

While there have been studies of the interface between LLTO and PEO-$LiCF_3SO_3$,[132] polymer electrolyte and glass,[133] and LLZO and liquid electrolyte,[134] there have been relatively few investigations of the PEO-LiTFSI/LLZO interface. Langer *et al*. was the first to study this

interface[85] and determined the resistance was relatively high. However, their study focused on the effects of surface irregularities rather than the origins of high $R_{interface}$. The objective of this work was to 1) understand the underpinning mechanisms that control ionic transport between the model polymer PEO-LiTFSI and LLZO and 2) develop a systematic approach to extend the fundamental understanding of this interface transport for CPEs and polymer catholytes used in combination with LLZO. Achievement of these goals could result in a significant step forward for the developments of high conductivity CPEs and batteries employing polymer catholyte and LLZO protecting Li metal anodes.

To analyze the interfacial kinetics, a trilaminar cell configuration was designed to accurately de-convolute and measure PEO/LLZO interfacial resistance, $R_{interface}$. Electrochemical impedance spectroscopy (EIS) was used to determine $R_{interface}$ between the two electrolytes. It was shown that the $R_{interface}$ between PEO-LiTFSI and as-densified LLZO is too high for facile charge transport at that interface. We believe the two factors that primarily limit interfacial kinetics are surface impurities on the LLZO and the abrupt change in Li-ion concentration between the electrolytes. Thus, effects of the two factors on $R_{interface}$ and methods to control and minimize the impedance were studied. We believe the results of this study could guide future efforts to develop systems requiring facile charge transport across ceramic/polymer interfaces.

Table 5. 1 *The ionic conductivity of CPE with varying LLZO fractions; Molecular weights of the PEO were excluded since they were in the range where ionic conductivity of PEO was independent of molecular weight.*[128]

Solid Electrolyte	Temperature (ºC)	σ (mS/cm)
PEO-LiTFSI (8:1)/*c*-LLZO (7.5 wt %)[124]	30	0.55
PEO-LiTFSI (8:1)/*c*-LLZO (10 wt %)[125]	30	0.18
PEO-LiTFSI (15:1)/*c*-LLZO (70 wt %)[126]	30	0.01
PEO-$LiClO_4$ (8:1)/*c*-LLZO (15 wt %)[127]	20	$0.95x10^{-2}$
PEO-$LiClO_4$ (8:1)/*c*-LLZO (20 wt %)[128]	30	0.44
PEO-$LiClO_4$ (20:1)/*c*-LLZO (40 vol %)[129]	20	$0.7x10^{-5}$
PEO-$LiClO_4$ (15:1)/*t*-LLZO (52.5 wt %)[130]	35	0.01

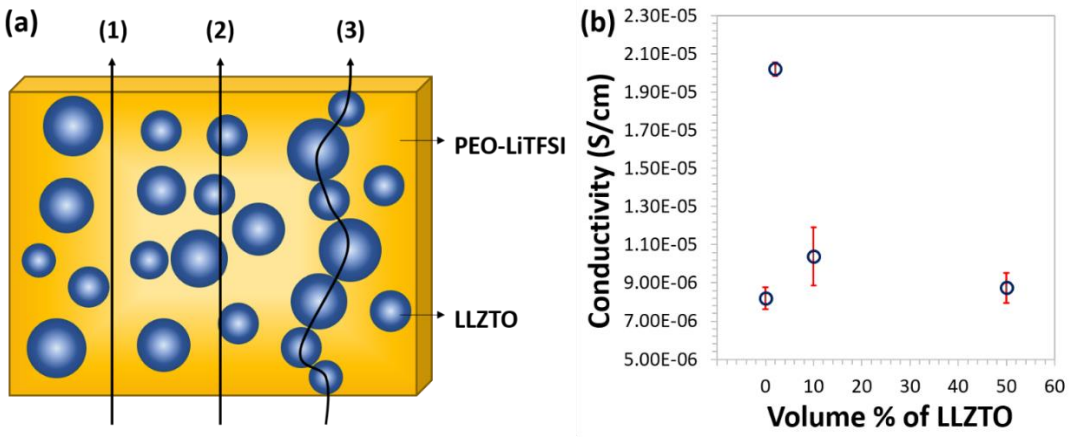

Figure 5.1 *(a) Possible ionic pathways in a PEO-LiTFSI/Ta-doped LLZO (LLZTO) composite electrolyte – Through (1) PEO-LiTFSI matrix (2) both the electrolytes (3) LLZO; (b) Effect of the volume percentage of LLZO on the ionic conductivity of CPE.*

5.2. Experimental Section

5.2.1.Materials synthesis and processing

5.2.1.1.Synthesis procedure for hot-pressed LLZTO (Ta-doped LLZO) and PEO-LiTFSI electrolytes

LLZTO powder was synthesized by a solid-state synthesis method. The details of the method are described in the section 3.1.2.1. The LLZTO powder received from synthesis was sintered to provide high density pellets using rapid induction hot-pressing at 1225^{o}C for 40min at 47 MPa.[89] Samples were cut using a diamond saw and then wet polished to 0.1 µm surface finish.

A solvent-free hot-pressing method was used to fabricate the PEO-LiTFSI electrolytes of desired [EO]:[Li] ratio, to ensure that residual solvent does not affect the electrochemical behavior. The details of the method are described in the section 3.1.1.2.

5.2.1.2. Li-ion Density Calculations

The Li-ion mass density was calculated for LLZTO and PEO-LiTFSI electrolyte membranes. There were three main assumptions made for the density calculations – 1) The theoretical density of the electrolytes was used for the electrolytes. Thus, the porosity was neglected; 2) The effect of chemical interactions between the Li salt and PEO on the density of the electrolyte were neglected; 3) It is important to remember that at higher Li salt concentrations the salt starts to precipitate in the polymer and does not participate in the Li-ion conduction. This is not reflected in the calculated density since it does include the precipitated Li.

The Rule of Mixtures was used to calculate the density of the PEO-LiTFSI electrolyte membranes. The calculated Li-ion mass densities are reported in Table 5.2.

5.2.1.3. Solid-state cell assembly and electrochemical testing procedure

To decouple the PEO-LiTFSI/LLZTO $R_{interface}$, a trilaminar cell configuration using blocking electrodes was used (Figure 5.4). The LLZTO electrolyte was interposed between two PEO-LiTFSI electrolytes. The sandwiched structure was assembled between two 1.27 cm diameter Au-coated Ni pins (current collectors) and heat-conditioned at 80^{o}C under a 100kPa pressure to form the PEO-LiTFSI/LLZTO interface. After conditioning, the cells were brought back to RT. Then, using EIS PEO-LiTFSI/LLZTO $R_{interface}$ was tracked at the desired temperature. A detailed description of cell assembly has been discussed in section 3.2.2.

For the heat-treatment study, LLZTO was heat-treated in argon at temperatures between 100 and 800^{o}C, in 100^{o}C increments, for 3 hours at each temperature. The [EO]:[Li] ratio in PEO was fixed to avoid any variability in the results due to the salt concentration of PEO. 27:1 [EO]:[Li] ratio was selected because it was the lowest salt concentration in the concentration range studied for this work. Thus, the concentration gradient would be the largest, resulting in the highest $R_{interface}$, between PEO and LLZTO for the 27:1 ratio.

For the salt concentration study, PEO-LiTFSI with different salt concentrations, were prepared via a solvent-free hot-pressing process. The cells were integrated in a trilaminar configuration and were conditioned as described above. The LLZTO pellets for this study were heat-treated at 400^{o}C. 400^{o}C was selected based of on previous study where, the lowest Li-LLZTO impedance was observed for 400 HT LLZTO.[28]

5.2.2. Materials Characterization techniques

The purity of LLZTO was confirmed with X-ray diffraction (XRD) (Rigaku Miniflex 600) using Cu Kα radiation (Figure 5.2). Figure 5.2 a shows XRD data for representative cubic LLZTO

and an untreated densified LLZTO disk. The absence of any impurity peaks in the XRD pattern for untreated LLZTO indicated that it was pure cubic-LLZTO. Scanning electron microscopy (TESCAN MIRA3) was used to characterize the surface of LLZO. Figure 5.2 b shows the SEM image of an untreated LLZTO disk. The untreated sample had a few pores, but overall the surface was smooth and dense.

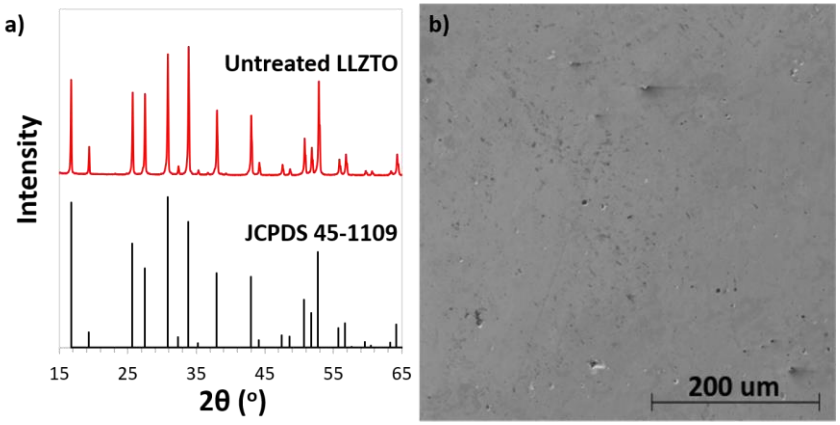

Figure 5.2 *a) X-ray diffraction (XRD) of cubic-LLZTO (JCPDS 45-1109) and Untreated LLZTO b) Scanning electron microscopy (SEM) image of polished untreated LLZTO sample*

Raman spectroscopy (Horiba Micro Raman Spectrometer housed in an argon-filled glovebox) was used to confirm the purity of PEO-LITFSI. The presence of peaks (Figure 5.3) which only corresponded to PEO-LiTFSI confirmed the purity of the electrolyte membrane. The absence of the OH stretching frequency (3100-3600 cm^{-1}, as seen in literature) peak confirms that no moisture was detected, which if present would affect the electrochemical behavior. Electrochemical Impedance Spectroscopy (EIS: Biologic VMP-300 galvanostat/potentiostat) was used to track impedance between 30-80^{o}C from 100 mHz to 7 MHz frequency with a perturbation voltage of 100mV.

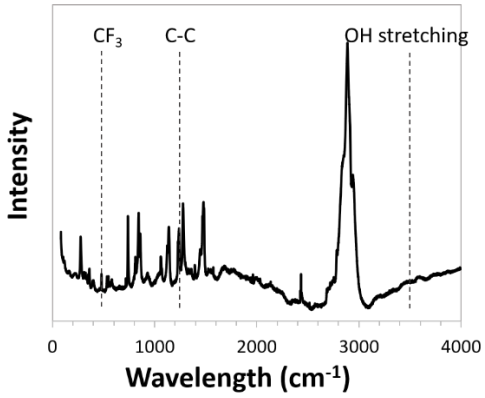

Figure 5.3 *Raman spectra for the PEO-LiTFSI membrane (27:1 [EO]:[Li] ratio)*

5.3. Results and discussion

5.3.1. Interfacial impedance analysis using a trilaminar cell configuration

To study the PEO-LiTFSI and LLZTO interface, a trilaminar cell was used (Figure 5.4). The frequency-dependent transport phenomena were characterized using EIS at 30^{o}C (Figure 5.4a). From Figure 5.4a, it can be observed that the EIS data consist of two distinct frequency-dependent phenomena represented by the two semi-circles and a capacitive tail representing the blocking behavior of the Au electrodes. An equivalent circuit (Figure 5.4b) consisting of three elements - R_{bulk}, (total of PEO-LiTFSI and LLZTO), $R_{interface}$ and M_{Au} was used to analyze the impedance plots. The grain boundary resistance of the LLZTO was excluded since its contribution to LLZTO bulk resistance was negligible (2.5%). By comparing these values with literature, it was confirmed that the higher frequency semi-circle corresponded to the bulk resistance (~$0.71*10^{-9}$ F/cm^2) from PEO and LLZTO while the lower frequency semi-circle corresponded to the $R_{interface}$ ($0.55x10^{-6}$ F/cm^2).[91] The magnitude of the average $R_{interface}$ from the impedance spectra was measured to be 96 kOhms.cm^2 which is high for facile charge transport.

For facile ionic transport across the PEO-LiTFSI/LLZTO interface, the $R_{interface}$ should be around <u>100</u> Ohms.cm^2. We believe that by understanding the underlying mechanisms that govern

interface transport, $R_{interface}$ could be controlled and reduced to enable facile charge transport across the PEO-LiTFSI/LLZTO interface.

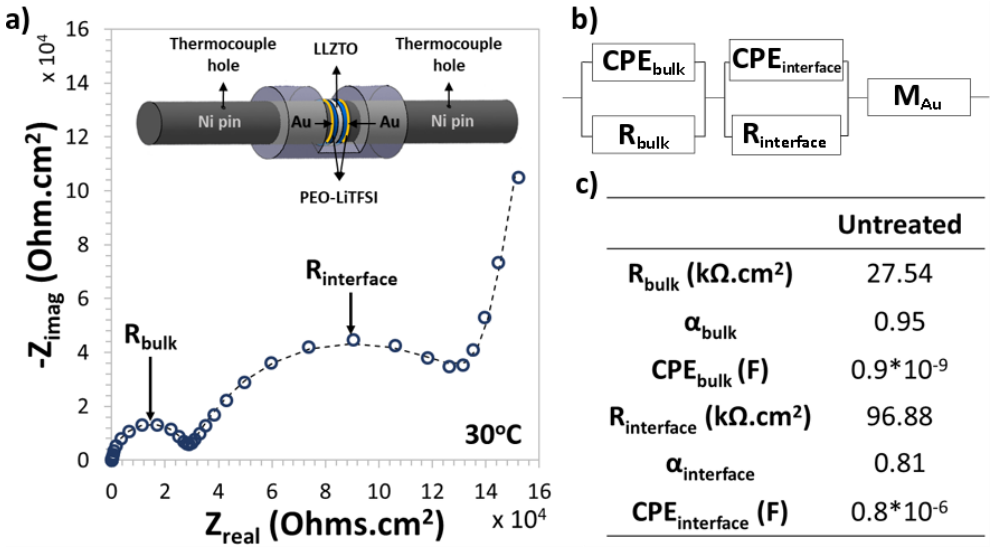

	Untreated
R_{bulk} (kΩ.cm²)	27.54
α_{bulk}	0.95
CPE_{bulk} (F)	$0.9*10^{-9}$
$R_{interface}$ (kΩ.cm²)	96.88
$\alpha_{interface}$	0.81
$CPE_{interface}$ (F)	$0.8*10^{-6}$

Figure 5.4 *(a) Impedance plot of an Au/PEO-LiTFSI/LLZTO/PEO-LiTFSI/Au symmetric cell at 30°C; inset shows the schematic of a trilaminar cell configuration (b) equivalent circuit for the trilaminar cell consisting of three elements- the bulk impedance, R_{bulk}, (total of PEO-LiTFSI and LLZTO), the interfacial impedance from two PEO-LiTFSI and LLZTO interfaces, $R_{interface}$, and the capacitive behavior from the Au blocking electrode (M_{Au}) (c) Impedance parameters obtained by fitting the impedance plot using the equivalent circuit*

5.3.2. Factors affecting the interfacial impedance between PEO-LiTFSI and LLZTO

In this study it was hypothesized that two factors which largely affect the $R_{interface}$ are LLZTO surface impurities and the abrupt change in Li-ion concentration between the electrolytes. Other factors such as chemical interactions between the two electrolytes,[135] surface roughness of the LLZTO surface,[132] and external factors such as temperature and stack pressure might also influence $R_{interface}$.

5.3.2.1. Surface impurities on the LLZTO surface

Sharafi *et al.* reported that a Li_2CO_3 surface layer on LLZTO exposed to air resulted in a high Li-LLZO $R_{interface}$.[90] Figure 5.5 depicts the PEO-LiTFSI/LLZTO phase with three layers

representing PEO-LiTFSI, Li_2CO_3 and LLZTO. We believe there are a few ways in which the Li_2CO_3 (Figure 5.5) layer can impede the interfacial kinetics. First, Li_2CO_3 is highly resistive and does not allow for facile charge transfer. The presence of the highly resistive Li_2CO_3 layer on LLZTO would result in a high $R_{interface}$ (Figure 5.4 a). Secondly, it can be observed in Figure 5.5 that the presence of Li_2CO_3 likely increases the oxygen density on LLZTO surface. The increased oxygen density could increase electrostatic repulsion between the oxygen in PEO where Li-ion is attached and LLZTO.[135] Due to the repulsion, the Li-ion hopping distance from PEO to LLZTO would increase, thus, impeding charge transfer kinetics. Heat-treatment of the LLZTO was shown to be successful in removing the Li_2CO_3 surface layer. Sharafi *et al*. reported that heat-treating the LLZTO at 400^{o}C resulted in lowering of Li-LLZTO $R_{interface}$.[28] Li *et al*. prescribed heat-treatment at 700^{o}C, in the presence of carbon, to eliminate the carbonate layer for pairing liquid electrolyte with LLZTO.[134] Building upon previous work, in this study the effect of heat-treatment temperature on PEO-LiTFSI/LLZTO interface was systematically studied. The optimum heat-treatment temperature was determined to remove the Li_2CO_3 while minimizing Li loss from the LLZTO. Essentially, we believe that removal of the impurity layer through heat-treatment reduces the $R_{interface}$ for two reasons. First, it eliminates the resistive Li_2CO_3 layer. Second, elimination of the Li_2CO_3 reduces the electrostatic repulsion between the LLZTO surface and PEO-LiTFSI, thus decreasing the Li-ion hopping distance between electrolytes, thereby facilitating transport across the interface.

5.3.2.2. Li-ion concentration disparity between PEO-LiTFSI and LLZTO

Figure 5.5 illustrates the large disparity in Li-ion concentration between PEO-LiTFSI and LLZTO; the Li-ion concentration in LLZTO was much higher than in PEO and hence, LLZTO was referred to as the higher Li-ion concentration phase (HLIC) and PEO as the lower Li-ion

concentration phase (LLIC). The Li ion concentration was found to be 46 times higher in LLZTO than 27:1 PEO-LiTFSI, Table 5.2. We believe that charge transfer kinetics are dependent on the direction of Li-ion transfer which can be opposite to the chemical gradient. To homogenize the Li-ion concentration at the PEO-LiTFSI/LLZTO interface, the Li-ion concentration in PEO can be easily modulated by increasing the Li salt concentration. Hence, we studied the effect of Li-ion concentration in PEO on the $R_{interface}$.

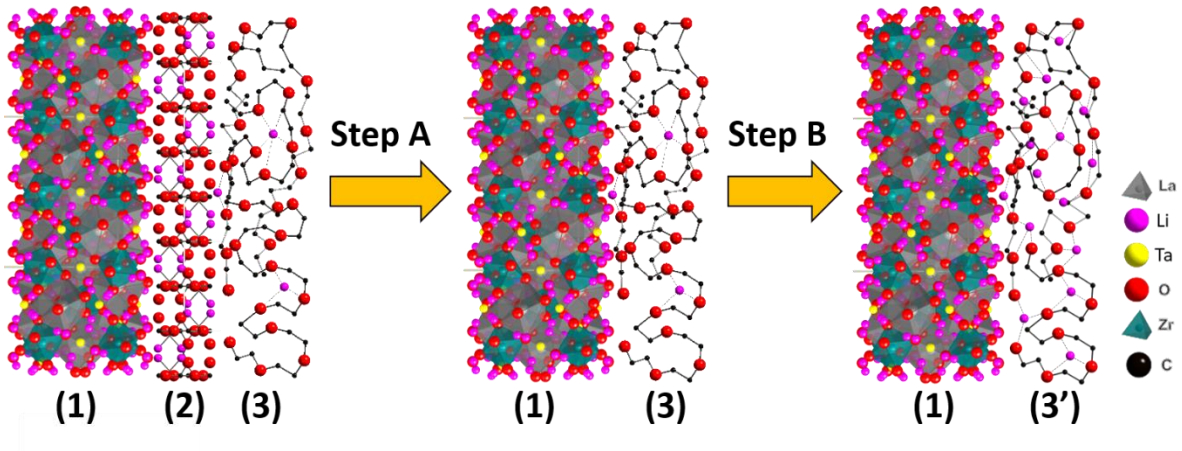

Figure 5. 5 *Schematic of a PEO-LiTFSI and LLZTO interface (to atomic scale). (1) LLZTO; (2) Impurity layer (Li_2CO_3); (3) PEO-LiTFSI (3') PEO-LiTFSI (higher salt concentration); Step A – Removal of the impurity layer; Step B – Increase in the salt concentration of PEO-LiTFSI*

We believe that by carefully studying the effects of interfacial chemistry and electrolyte concentration the PEO-LiTFSI/LLZTO $R_{interface}$ can be reduced to 100 Ohms.cm^2; or comparable to Li-ion cell impedance. A low $R_{interface}$ would allow for facile ionic transfer across the interface and hence, enabling systems benefitting from PEO/LLZO interfaces.

5.3.3. Effect of Heat-treatment temperature of LLZTO on the interfacial impedance

To study the effect of heat-treatment temperature of LLZTO on $R_{interface}$, trilaminar cells were used. The heat-treatment temperature ranged from untreated to a temperature where evidence of Li loss was observed. To minimize storage time, thereby minimizing the chance of

contamination in the glove box, the trilaminar cells were assembled immediately after heat-treatment. The $R_{interface}$ was measured as a function of heat-treatment temperature. Three trilaminar cells were characterized at 30°C for each HT; the average and standard deviations are shown in Figure 5.6a.

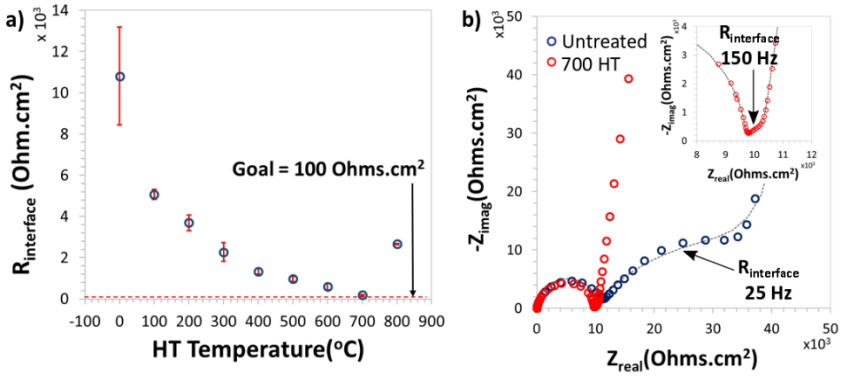

	Untreated	700 HT
R_{bulk} (kΩ.cm²)	11.24	9.16
α_{bulk}	0.86	1
CPE_{bulk} (F/cm²)	$0.63*10^{-9}$	$0.17*10^{-9}$
$R_{interface}$ (kΩ.cm²)	14.57	0.20
$\alpha_{interface}$	0.73	0.84
$CPE_{interface}$ (F/cm²)	$2.84*10^{-6}$	$4.09*10^{-6}$

Figure 5.6 *(a) Effect of LLZTO HT temperature on the interfacial impedance between PEO-LiTFSI and LLZTO at 30°C (b) Nyquist plots comparing two Au/PEO-LiTFSI/LLZTO/PEO-LiTFSI/Au symmetric cells at 30°C; one with untreated LLZTO and the other with LLZTO heat treated at 700°C (b) Impedance parameters obtained by fitting the Nyquist plot using the equivalent circuit in Figure 5.4 b*

Multiple observations were made from Figure 5.6a. First, it was observed that $R_{interface}$ was the highest for untreated LLZTO samples. The high resistance was likely due to the presence of a Li_2CO_3 surface layer which acts as a barrier for charge transfer between PEO-LiTFSI and LLZTO. Also, for untreated samples, because the initial thickness of the impurity layer cannot be controlled precisely, the variability (2.38 kOhms) in $R_{interface}$ was highest for these samples. Second, the higher the heat-treatment temperature (closer to the decomposition temperature of Li_2CO_3; 730-1270°C), the lower was the $R_{interface}$ of the cell. Thus, with increasing heat-treatment temperature some Li_2CO_3 was removed, leading to a thinner insulating layer, which then resulted in lower $R_{interface}$. Lastly, the $R_{interface}$ decreased with increasing heat-treatment temperature reaching a minimum at 700°C. Above 700°C the resistance increased for cells with LLZTO heat-treated at

800°C. It has been further discussed that 800°C was the temperature where LLZTO starts to decompose.

The change in $R_{interface}$ with cell temperature for LLZTO heat-treated at different temperatures was also studied (Figure 5.7). It was observed that the improved interfacial kinetics with increasing cell temperature for each heat-treatment temperature led to a decrease in $R_{interface}$. It was also observed that the temperature-dependent transport was linear for all heat-treatments between 30 and 80°C. This result has an important implication. Typically, PEO-LiTFSI has two temperature-dependent conductivity regimes (low temperature and high temperature) attributed to its melting point. Thus, the absence of two regimes indicates that $R_{interface}$ does not have a strong dependence on PEO-LiTFSI ionic conductivity.

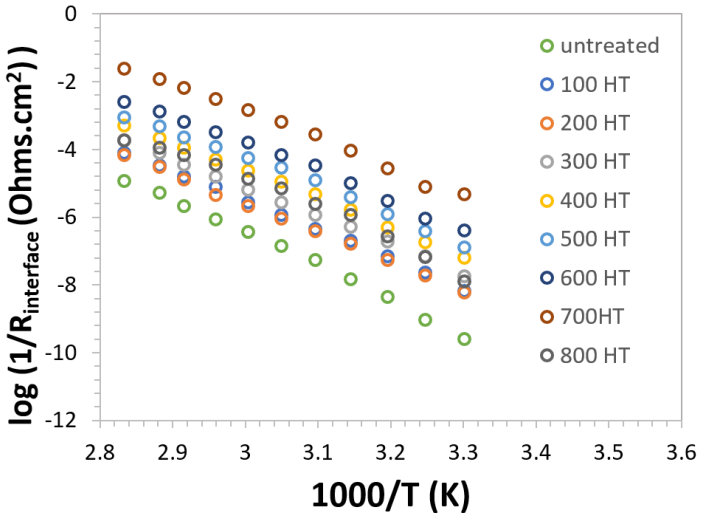

Figure 5.7 *Effect of temperature on the interfacial resistance between PEO-LiTFSI and LLZTO*

Figure 5.6b compares the impedance behavior of trilaminar cells consisting of untreated and 700HT LLZTO. It was observed that the $R_{interface}$ semi-circle, clearly visible for the untreated LLZTO, was not apparent for 700HT LLZTO. Removal of the surface impurity layer from LLZTO

led to the reduction in $R_{interface}$. Because there was no decomposition of LLZTO by the heat-treatment, the bulk impedance did not dramatically change. The average $R_{interface}$ at 30^{o}C was 180 Ohms.cm^2. This value is the lowest PEO-LiTFSI/LLZTO $R_{interface}$, which has been reported in literature. By carefully studying the effect of heat-treatment temperature of LLZTO on $R_{interface}$ we were able to reduce the impedance by a factor of ~250 from our initial results.

Because a change in behavior was observed above 700^{o}C, X-ray diffraction (XRD) and scanning electron microscopy (SEM) were used to characterize LLZTO. Figure 5.8a shows XRD data for representative cubic LLZTO, 700HT and 800HT LLZTO. The absence of any impurity peaks in the XRD pattern for 700HT LLZTO indicated that there was no apparent chemical decomposition of the sample at that temperature. However, a peak at $2\theta=29^{o}$, corresponding to $La_2Zr_2O_7$, was observed for the 800HT LLZTO indicating Li loss from the LLZTO.

Although the XRD analysis indicated that Li loss was observed for 800HT LLZTO, it does not provide information about how that affects the LLZTO surface. SEM was used to analyze the effect of Li loss on the LLZTO surface. For the SEM analysis three polished samples were analyzed – untreated, 700HT and 800HT LLZTO (Figure 5.2a, 5.8b and 5.8c). The untreated sample had a few pores, but overall the surface was smooth and uniform. Compared to the untreated sample, the 700HT LLZTO showed some evidence of growth on its surface, but no significant change was observed. However, unlike the untreated and 700HT LLZTO samples, a significant change in morphology was observed for the 800HT LLZTO (Figure 5.8c). We believe the change in morphology was primarily due to Li loss, which is consistent with the formation of $La_2Zr_2O_7$ as observed in the XRD analysis. The increase in $R_{interface}$ with an 800HT LLZTO was likely caused by the formation of a resistive layer of $La_2Zr_2O_7$. Thus, the XRD and SEM analysis

confirmed that 700°C was the highest temperature at which LLZTO could be heat-treated without any deleterious effect on LLZTO.

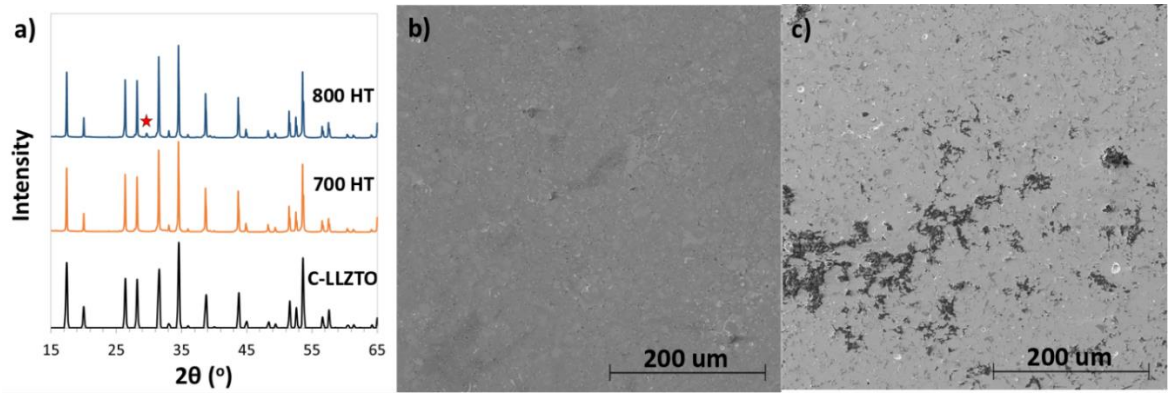

Figure 5.8 (*a) X-ray diffraction (XRD) on LLZTO heat-treated at different temperatures – cubic-LLZTO, 700°C and 800°C; Unknown impurity peak for 800°C indicated by a star; Scanning electron microscopy using for polished LLZTO pellets heat-treated at (b) 700°C (c) 800°C*

5.3.4. Effect of salt concentration in PEO ([EO]:[Li] ratio) on the interfacial resistance between LLZTO and PEO-LiTFSI

As discussed earlier, by increasing the Li-salt concentration in PEO, the abrupt change in Li-ion concentration gradient can be reduced, which should facilitate transport. To study the effect of Li-ion concentration of PEO-LiTFSI on the PEO-LiTFSI/LLZTO interfacial kinetics, $R_{interface}$ was characterized as a function of Li-salt concentration. PEO-LiTFSI with different salt concentrations; [EO]:[Li] 3:1, 6:1, 9:1, 12:1, 18:1, 27:1, were prepared. Three membranes of each composition were tested using the trilaminar cell configuration.

Table 5.2 shows change in the mass density of Li (g/cm^3) in PEO-LiTFSI with increasing LiTFSI concentration. As expected, the Li-ion concentration in the electrolyte increases with increasing salt concentration in the polymer. The increase in Li-ion concentration in the polymer would decrease the difference in Li-ion concentration between LLZTO and PEO-LiTFSI

electrolyte and perhaps lead to a reduction in $R_{interface}$. However, it is important to remember, as mentioned the section 5.2.1.2, that at higher Li salt concentrations the salt starts to precipitate in the polymer and does not participate in the Li-ion conduction. This is not reflected in the calculated density since it does include the precipitated Li.

Figure 5.9a shows the variation in $R_{interface}$ at 30^{o}C with salt concentration. It was observed that with increasing salt concentration from 27:1 to 3:1, the $R_{interface}$ first decreased reaching a minimum value at 15:1 salt concentration and then increased again. When the salt concentration increased from 27:1 to 15:1, the Li-ions participating in Li-ion transport in PEO increased and thus the $R_{interface}$ decreased. Beyond 15:1 concentration towards higher salt concentration, the $R_{interface}$ increased again. Ideally, by increasing the salt concentration the carrier concentration disparity should decrease and thus the $R_{interface}$ should decrease, but that was not the case. We believe this could be explained by the precipitation of Li-salt in the PEO. The Li-ions in the precipitated salt do not participate in ionic conduction and instead acts as inactive filler or worse. It is possible that the LLZTO surface promoted heterogeneous nucleation causing the LiTFSI to precipitate and passivate the interface. Subsequent studies could analyze this, but clearly the $R_{interface}$ does increase above the 15:1 [EO]:[Li] ratio. Thus 15:1 was the optimum salt concentration for minimizing the $R_{interface}$.

Figure 5.9b shows the decrease in $R_{interface}$ achieved by optimizing the salt concentration in PEO. Two impedance plots are shown for PEO with salt concentration of 27:1 (which was used for the heat-treatment study) and 15:1. It was observed that the $R_{interface}$, was smaller for the cell with 15:1 compared to 27:1 salt concentration. The average PEO-LiTFSI/LLZTO $R_{interface}$ at 30^{o}C was 421 Ohms.cm^{2} for the 15:1 sample (Figure 6.c). Thus, by carefully studying the effect of Li-

ion concentration in PEO-LiTFSI on the PEO-LiTFSI/LLZTO $R_{interface}$ we were reduced the impedance by a factor of ~4 from the heat-treatment study results for 400HT LLZTO.

Table 5. 2 *Mass density of Li (g/cm^3) in LLZTO and PEO-LiTFSI*

Mass density of Li (g/cm^3)	
LLZTO ($Li_{6.5}La_3Zr_{1.5}Ta_{0.5}O_{12}$)	0.276
PEO-LiTFSI (EO:Li - 27:1)	0.006
PEO-LiTFSI (EO:Li - 18:1)	0.008
PEO-LiTFSI (EO:Li - 15:1)	0.009
PEO-LiTFSI (EO:Li - 12:1)	0.011
PEO-LiTFSI (EO:Li - 9:1)	0.013
PEO-LiTFSI (EO:Li - 6:1)	0.016
PEO-LiTFSI (EO:Li - 3:1)	0.022

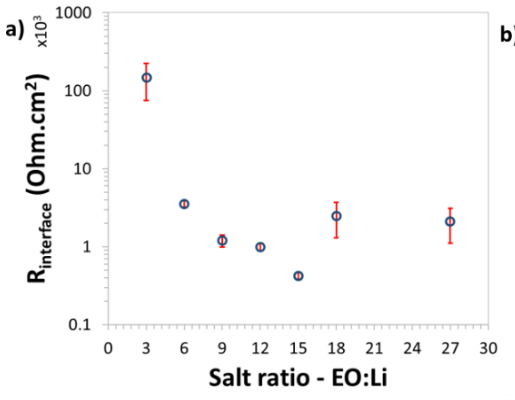

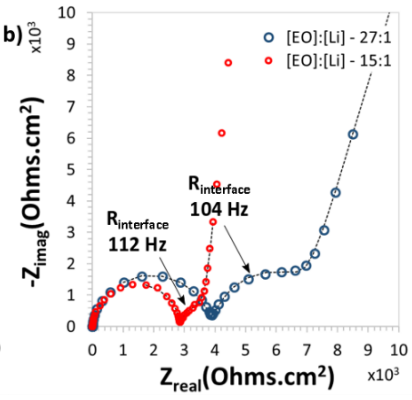

c)	27:1	15:1
R_{bulk} (kΩ.cm²)	3.82	2.84
α_{bulk}	0.89	0.99
CPE_{bulk} (F/cm²)	$3.16*10^{-9}$	$0.63*10^{-9}$
$R_{interface}$ (kΩ.cm²)	1.48	0.44
$\alpha_{interface}$	0.90	0.87
$CPE_{interface}$ (F/cm²)	$1.26*10^{-6}$	$4.50*10^{-6}$

Figure 5.9 *(a) Effect of salt concentration in the PEO-LiTFSI electrolyte on the interfacial resistance between PEO-LiTFSI and LLZTO electrolytes (b) Nyquist plots comparing two Au/PEO-LiTFSI/LLZTO/PEO-LiTFSI/Au symmetric cells at 30^{o}C; one with 27:1 salt concentration and the other with 15:1 salt concentration in the PEO-LiTFSI electrolyte (c) Impedance parameters obtained by fitting the Nyquist plots using the equivalent circuit in Figure 5.4b.*

5.4. Implications

In section 5.1 it was shown that Li-ion transport in a hybrid electrolyte configuration was likely to be limited by the high PEO/LLZTO $R_{interface}$. In addition, to achieve parity with state-of-the-art Li-ion cell resistance, transport through the PEO/LLZO interface should be < 100 Ohms.cm^2. The results of this study show that by addressing the root cause behind the high $R_{interface}$ (surface impurities and abrupt change in Li-ion concentration at the interface) the goal of 100 Ohms.cm^2 interfacial resistance was nearly achieved (180 Ohms.cm^2). The progress made in this work will have implications for a hybrid electrolyte approach. A low $R_{interface}$ allows for facile ionic transfer across the model polymer and LLZTO interface. Thus, the systematic approach used to study the model polymer system in this work, can provide guidelines for engineering a GPE/LLZTO interface with facile charge transport kinetics.

5.5. Conclusion

In this study, it was shown that high PEO-LiTFSI/LLZTO $R_{interface}$ (~95 kOhm.cm^2) limits the total conductivity of CPE. This study focused on understanding transport across the PEO-LiTFSI/LLZTO interface with the goal of enabling systems that benefit from facile charge transport across polymer-LLZTO interfaces like CPEs and bilaminar/hybrid electrolyte configurations. The PEO/LLZO interface kinetics was analyzed using a trilaminar cell configuration that accurately measured impedance across each interface. First, it was shown that LLZTO surface impurities and abrupt change in Li-ion concentration between PEO-LiTFSI and LLZTO were the underlying causes of the high $R_{interface}$ between the two electrolytes. The effect of the heat-treatment temperature of the LLZTO on the $R_{interface}$ was studied to remove surface impurities. It was observed that $R_{interface}$ was inversely proportional to LLZTO heat-treatment temperature up to 800^{o}C at which Li loss occurred causing an increase in $R_{interface}$. By optimizing

the LLZTO surface, the $R_{interface}$ was reduced to 180 Ohms.cm^2 at 30^{o}C (700HT), which is the lowest reported in literature. Second, the disparity in Li-ion concentration between PEO and LLZTO was reduced by increasing the salt concentration in PEO. By carefully studying the effect of salt concentration on PEO-LiTFSI/LLZTO interface an optimal salt concentration (15:1) was determined. The $R_{interface}$ was reduced by a factor of four compared to 27:1 salt concentration. We believe that by combining the results from the heat-treatment and the salt concentration study and using the optimized conditions from both the studies, we can achieve $R_{interface}$ values, which could enable total cell resistance comparable to Li-ion (~ 10-100 Ohms.cm^2). Thus, to achieve the lowest $R_{interface}$ it would be recommended to heat-treat the LLZTO samples at 700^{o}C and use 15:1 [EO]:[Li] salt concentration for the PEO-LiTFSI electrolyte membranes. The results of this study are valuable to achieve the objectives of this thesis and provides an important framework for the successful development of kinetically favorable GPE/LLZTO interfaces for hybrid electrolyte configurations.

5.6. Acknowledgement

We would like to acknowledge the support from Robert Bosch LLC, Research and Technology Center, Sunnyvale, California, USA for this project.

Chapter 6 Electrochemical and Surface Chemistry Analysis of Lithium Lanthanum Zirconium Tantalum Oxide (LLZTO)/Liquid Electrolyte (LE) Interfaces

6.1. Introduction

The need for high-energy-density Li-ion batteries has provided the impetus to replace graphite anodes with Li metal anodes.[12] However, as mentioned in Chapter 1, the conventional liquid electrolytes [LE] utilized with graphite anodes form an unstable solid electrolyte interphase (SEI) with Li metal, which leads to cycling instabilities and safety issues.[13,15–17,118] To overcome the challenges faced with conventional LE, fast-ion conducting ceramic electrolytes have emerged as promising alternatives, since they provide high ionic conductivities, compatibility with Li metal and safety.[62,136] In particular, there has been considerable progress made in reducing the interfacial resistance ($R_{interface}$) and improving stability between solid electrolytes (SEs) and Li metal.[20,54] However, the implementation of SEs in all solid-state batteries leads to formation of solid-solid interfaces within composite cathodes and at the interface of the composite cathode and the solid electrolyte. These interfaces can lead to rapid capacity fade and high resistance due to chemical instabilites, contact loss, and uncompensated volumetric changes in the cathode.[64,65]

The approach suggested in this thesis to overcome the incompatibility between SE and cathode is the introduction of a GPE, a hybrid electrolyte approach. Since the Li-ion conduction in a GPE in through the LE entrapped in the polymer matrix, it is important to study the stability of the SE with the LEs present in the GPE. Thus, this chapter is dedicated to studying the (electro)chemical stability and kinetics of the SE and LE interface.

Recently, in literature, the performance of cells with small quantities of LE at the SE/cathode interface have been evaluated. In that configuration the SE would protect the Li metal and LE eliminates the challenges at the solid electrolyte and cathode interface.[137,138] Unfortunately, previous reports in literature show that the SE/LE interface poses challenges due to the (electro)chemical instability at that interface. First, it has been reported that the $La_{0.55}Li_{0.35}TiO_3$ (LLT) SE/various LEs interface resistance is high (10,000 Ohms.cm^2 for 1 M $LiClO_4$ in PC), which is related to the slow desolvation kinetics of the LE from the solvent.[139] Second, Busche *et al*[137] have reported the formation of a solid-liquid electrolyte interphase (SLEI) when the studying the compatibility between the SE $Li_{1+x}Al_xGe_{2-x}(PO_4)_3$ (LAGP) and an LE, which indicates possible chemical reactions causing increasing interfacial resistances. In this work the hybrid electrolyte scheme using the promising SE based on Li-garnet was investigated. Here, we explore the promising $Li_{6.5}La_3Zr_{1.5}Ta_{0.5}O_{12}$ (LLZTO) SE due to its high ionic conductivity at room temperature (RT), and its ultra-low interfacial resistance and stability with metallic Li.[28,94] Recently, three studies[86,87,140] have reported the formation of an unstable SLEI between LLZTO and different LEs leading to similar cycling instability and high resistance.[137,139] In particular Liu *et al*[86] reported growth of LLZTO/LE interfacial resistance with time due to the formation of an interphase composed of LiF and other decomposition products. While the study by Liu *et al* was the first to uncover this incompatibility, the underlying source of instability and associated solutions to address the chemical reactions are still unknown. From the outcomes of these studies, it is clear that for a stable SE/LE interface there is a need to understand the factors that affect SE/LE interface stability.

The goal of this study is to identify the specific component of the LE that reacts with the SE. By understanding the reactions between the SE and LE, it is possible to develop approaches

to limit or eliminate chemical side reactions at the interface. First, this study aims to identify the chemical interactions and reactive species between LLZTO and an state-of-the-art (SOA) liquid electrolyte. The second goal is to apply the knowledge gained on the cause of LE/SE instability to demonstrate a stable LE/SE interface. To achieve this, we attempted to isolate the effects of organic solvents and Li salts. The results indicate that although organic solvents do form a carbon compound on LLZTO, this layer does not significantly affect the electrochemical performance of the cell. Conversely, it was determined that the chemical reactions and high $R_{interface}$ between the LE and LLZTO are highly sensitive to the Li salt. $LiPF_6$ and LiBOB exhibit unstable behavior against LLZTO, whereas LiTFSI was shown to be dramatically more stable (as will be discussed in section 6.3.3). This further confirms that the Li salt plays a more important role in the LE and LLZTO interfacial reaction than the organic solvents.

Overall, by understanding the reaction pathways between the LE and LLZTO SE, we identified a compatible LE solvent/salt combination to achieve a stable interface with $R_{interface}$ less than 50 Ohms.cm^2, which is comparable to electrode interfaces in Li-ion technology. We further demonstrate preliminary full-cell cycling utilizing the dual electrolyte with a Li metal anode, which exhibits minimal capacity fade. We demonstrate that by carefully studying the possible chemical interactions between the LE and SE, it is possible to effectively eliminate the instability between the two electrolytes. The knowledge gained in this chapter can then be used for the implementation of the hybrid electrolyte approach to enable batteries with Li metal anodes.

6.2. Experimental Methods

6.2.1 LLZTO (Ta-doped LLZO) preparation.

A solid-state synthesis method was used to synthesize the $Li_{6.5}La_3Zr_{1.5}Ta_{0.5}O_{12}$ (LLZTO) powder.[141] The powder was then sintered using rapid induction hot-pressing at 1225^{o}C for 40min

at 47 MPa.[89] The high-density pellet produced by hot-pressing was then cut into 1-1.2 mm electrolyte membranes using a diamond saw. The membranes were then faced and wet polished using an auto polisher to 0.1 μm surface finish. For the full cells (Li/LLZTO/LE/cathode) a thin pellet was hot-pressed and cut to give two membranes of 1.5-1.7 mm thickness. Before any electrochemical testing, the LLZTO electrolyte membranes were heat-treated at 400^{o}C in an inert atmosphere to eliminate the impurities on the surface of LLZTO.[28]

6.2.2 Liquid electrolyte preparation.

For the conventional liquid electrolyte, a dried 1M $LiPF_6$ in 1,3-dioxolan-2-one (EC)/ethyl methyl carbonate (EMC) (50:50 v%) liquid electrolyte from Soulbrain MI was used. To study the stability of LLZTO with LEs of varying compositions, anhydrous organic solvent and Li salts were used to synthesize the LEs. The stability of LLZTO was tested with five different anhydrous solvents - 4-methyl-1,3-dioxolan-2-one (PC), dimethyl carbonate (DMC), acetonitrile (ACN), 1,2-dimethoxyethane (DME) and 1,3-dioxolane (DOL) (Sigma Aldrich). All the solvents were stored in an Ar-filled glovebox. The stability of LLZTO was also evaluated with LE prepared with different anhydrous Li salts [Lithium hexafluorophosphate ($LiPF_6$) (Sigma Aldrich), Lithium bis(oxalate)borate (LiBOB) (Alfa Aesar), and Lithium bis(trifluoromethanesulfonyl)imide (LiTFSI) (Sigma Aldrich)]. The Li salts were dried ($LiPF_6$ at 60^{o}C, LiBOB and LiTFSI at 120^{o}C) under vacuum for 24 hours before the electrolyte preparation. For the preparation of the LE with a required molarity, a measured amount of Li salt was mixed with the solvent for 24 hours. All the LE preparation was performed in an Ar-filled glovebox.

6.2.3 Electrochemical testing.

6.2.3.1 H-cell configuration

An H-cell configuration (graphite foil/LE/LLZTO/LE/graphite foil) was used to measure the LLZTO/LE $R_{interface}$ (Figure 6.1). The H-cell consists of two 5 ml glass compartments (filled with LEs) separated by the LLZTO membrane. Viton rings were used on each side of the LLZTO to prevent leakage. Two graphite strips were used as electrodes (0.4 cm^2), one in each compartment. The electrodes were dried under vacuum for 24 hours before cell assembly to ensure that there was no moisture contamination. All the materials in the H-cell configuration were inert to the solvent in use (ACN). Electrochemical Impedance Spectroscopy (EIS: Biologic VMP-300 galvanostat/potentiostat) was used to track cell resistance at room temperature from 0.5 Hz to 7 MHz, with a perturbation voltage of 100mV. The EIS analysis was performed every ½ hour for 48 hours to track the LLZTO/LE $R_{interface}$. Control cells were tested in the same configuration without LLZTO for reference. It was observed from the EIS measurements on the control cell that there was no additional resistance contribution from the graphite foil/LE interface (Figure 6.2).

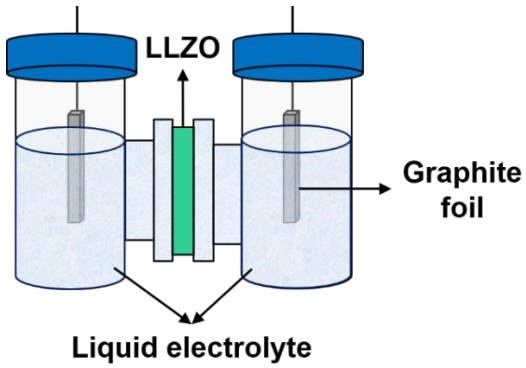

Figure 6.1 *H-cell configuration: graphite foil/LE/LLZTO/LE/graphite foil*

6.2.3.2 Full cell configuration

Full cells with the configuration Li/LLZTO/LE/NCA (Lithium nickel cobalt aluminum oxide) cathode were assembled in a Swagelok® cell (Figure 6.11 a). The first step in preparing the cells was integration of the Li metal on LLZTO (on the polished surface), followed by heat

conditioning.[111] A 700um thick Li foil (Alfa Aesar) was used, which was cleaned by scraping the oxide impurities from the surface immediately before integrating with LLZTO. The Li was integrated on masked LLZTO with a contact area of 0.5 cm^2. The LLZTO disk with Li was then assembled between two Ni pins, which were aligned using PTFE fixtures. The cells were heated at 170^0C overnight on a hotplate and insulated using quartz wool. The temperature was tracked using two type-K thermocouples attached to the Ni pins. After conditioning, the LLZTO disk was transferred into a polyetherimide (PEI) sleeve that sits in the body of a Swagelok® cell. The edge of the sample was sealed using a glue (compatible with the LE), to the walls of the sleeve, in order to ensure that there was no risk of side leakage of the LE to the Li electrode. A 2M LiTFSI in PC LE was prepared for the full cell. After the addition of the LE/GF-D (Glass fiber filter) and NCA cathode (3 mAh/cm^2 loading) an Al pin was placed on top of the cathode and the end caps were screwed on the body of the Swagelok® under a 3 MPa stack pressure (using a load cell from Imada Inc.). All electrochemical testing was done on a Biologic VMP-300 galvanostat/potentiostat. Galvanostatic cycling was performed by polarizing the NCA cathode between 2.5 and 4.2 V versus Li/Li+ at a C/20 rate (current density – 0.15 mA/cm^2).

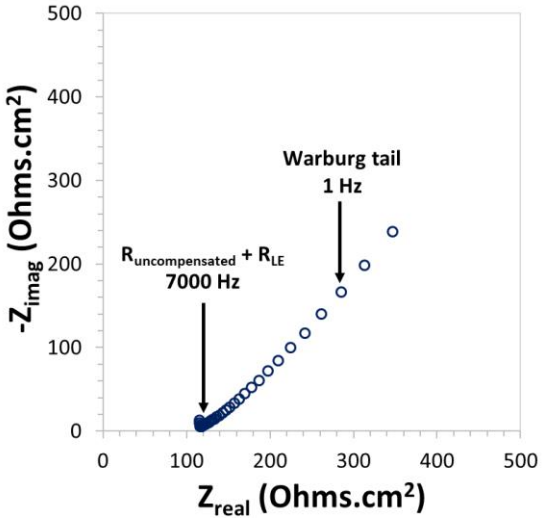

Figure 6.2 *EIS analysis of control H-cells without LLZTO: graphite foil/LE/graphite foil. There was no additional resistance contribution oberved for the graphite foil/LE interface which was confirmed by the absence of a semi-circle at lower frequencies*

6.2.4 *Materials' surface and structural characterization*.

The purity of LLZTO samples was confirmed with X-ray diffraction (XRD) (Rigaku Miniflex 600) using Cu Kα radiation. X-ray diffraction (XRD) data for a densified LLZTO electrolyte and representation cubic LLZTO (JCPDS 45-1109) in shown in Figure 6.3a. It was observed that there were no impurities peaks present in the XRD pattern for densified LLZTO, showing that it was pure cubic-LLZTO. Before the characterization, the LLZTO electrolytes were first heat-treated and then exposed to different organic solvents and liquid electrolytes for 48 hours. Scanning electron microscopy (SEM) (TESCAN RISE) was used to characterize the surface of LLZTO on exposure to organic solvents and LEs. The heat treated LLZTO sample had an overall smooth and dense surface with a few pores observed in the Scanning electron microscopy (SEM) image in Figure 6.3b.

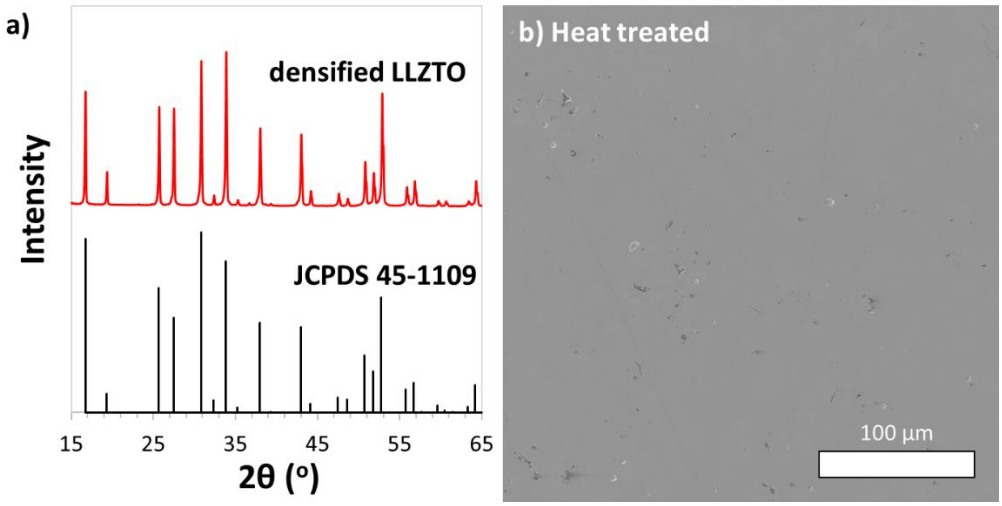

Figure 6.3 *a) X-ray diffraction (XRD) of cubic-LLZTO (JCPDS 45-1109) and densified LLZTO b) Scanning electron microscopy (SEM) image of heat treated LLZTO electrolyte*

X-ray photoelectron spectroscopy (XPS) was performed to study the effects of organic solvents and liquid electrolytes on the surface of LLZTO. The XPS spectra were collected on a Kratos Axis Ultra 8-channel detector system. A monochromated Al x-ray source was used, along with a pass energy of 160 eV for survey scans and 20 eV for core scans. Samples were transferred into the UHV chamber of the XPS ($<1*10^{-9}$ torr) through a connected Ar glovebox, thereby completely avoiding air exposure. Sputtering was performed using a Minibeam III ion gun with an accelerating voltage of 4 kV and an extractor current of 150 µA. All the compositions reported in this study were after 110 s of sputtering to remove most of the adventitious C layer and enable comparison with the stoichiometric composition of the LLZTO. Spectra were analyzed using CasaXPS and fit with Tuoguaard backgrounds. All spectra were calibrated to the C-C bonding peak in the C 1s core scan at 284.8 eV.

The La 3d core scans at the surface were used to avoid any artifacts or bonding environment changes due to the Ar sputtering. The LiF standard spectra were collected from an LiF film

deposited via atomic layer deposition using lithium tert-butoxide and titanium tetrafluoride.[142] The LiF reference was used to establish the peak locations and relative intensities for the Fluorine auger peak that overlaps with the La 3d when using an AL x-ray source. These peak locations were constrained to within 0.1 eV of the values measured for pure LiF, and the relative peak intensities were fixed at the measured values from the standard when fitting the electrolyte exposed LLZTO sample. The bulk LLZTO spectra was also fitted using 3 pairs of peaks, representing the multiplet splitting and spin-orbit coupling behavior of the La 3d peak, as has been observed previously.[143] The component peak locations and relative intensities were again constrained to the measured values when using those components to fit the electrolyte exposed sample for Figure 6.4. The peak locations for each of the standard samples are shown in Table 6.1.

Table 6.1 *The peak locations for each of the standard samples in the XPS analysis*

Material	Peak #	Component	Peak Position (eV)
LiF	1	F KLL - 1	831.5±0.2
	2	F KLL - 2	834.2±0.2
	3	F KLL - 3	857.5±0.2
	4	F KLL - 4	837±0.2
	5	F KLL - 5	849.7±0.2
	6	F KLL - 6	841±0.2
	7	F KLL - 7	828.6±0.2
LLZO	1	La 3d 5/2	833.2±0.2
	2	La 3d 3/2	850±0.2
	3	La 3d 5/2 L bonding	837.8±0.2
	4	La 3d 3/2 L bonding	854.7±0.2
	5	La 3d 5/2 plasmon	847.2±0.2
	6	La 3d 5/2 L antibonding	835±0.2
	7	La 3d 3/2 L antibonding	851.5±0.2
LaF_3	1	La 3d 5/2	838±0.2
	2	La 3d 3/2	854.4±0.2
	3	La 3d 5/2	840.4±0.2
	4	La 3d 3/2	856.8±0.2
	5	F KLL	830±0.2

6.3. Results and Discussion

6.3.1 *Chemical instability between LLZTO and 1 M $LiPF_6$ in EC:EMC.*

EIS was performed to characterize the interfacial resistance between LLZTO and a conventional LE (1 M $LiPF_6$ in EC:EMC 50:50 vol%) ($R_{interface}$). For this, an H-cell configuration (graphite foil/LE/LLZTO/LE/graphite foil) with graphite electrodes was used (Figure 6.4a). Immediately after cell assembly, $R_{interface}$ was measured at 407 Ohms.cm^2, which is significanly higher than what is typically considered to be an acceptable limit (~ 100 Ohms.cm^2). To determine if $R_{interface}$ changed with time, the cell was analyzed every half hour using EIS over a period of 24 hours. It can be observed from Figure 6.4a that the Nyquist plot consisted of two semi-circles that correspond to two distinct frequency-dependent physical phenomena, and a Warburg tail from the graphite electrodes. From the capacitance values of the two semi-circles it was confirmed that the higher frequency semi-circle corresponded to bulk impedance (R_{bulk}) (10^{-10} F) from LLZTO and the lower frequency semi-circle corresponded to interfacial impedance (10^{-6} F).[91] The Warburg element does not affect measurement of the interface impedances as addressed in the experimental section. The EIS measurements on the control cell (graphite foil/LE/graphite foil) show that there was no additional resistance contribution from the graphite foil/LE interface (Figure 6.2). Thus, the lower frequency semi-circle solely corresponds to LLZTO/LE interfacial resistance ($R_{interface}$). The high-frequency intercept on the x-axis represents the ohmic drop from the LE and uncompensated resistance. Additionally, a dramatic increase in $R_{interface}$ was observed in Figure 6.4a after 24 hours (from 407 Ohms.cm^2 to 830 Ohms.cm^2), whereas the R_{bulk} for LLZTO remains constant. The constant R_{bulk} indicates that the bulk LLZTO was unaffected. On the other hand, the increase in $R_{interface}$ indicates a chemical instability between LLZTO and LE (surface layer formation or chemical reaction). This agrees with previous reports that show similar instability

between LLZTO and conventional LEs.[86,87] The nature of the instability can not be established alone from EIS, which motivated an in-depth surface characterization of the LLZTO after exposure to LE.

To investigate the LLZTO-LE interfacial instability, SEM analysis was conducted for an LLZTO electrolyte membrane exposed to 1M $LiPF_6$ in EC:EMC LE for 24 hours. The surface was then rinsed with ethanol for cleaning before loading it in the SEM. As a point of reference, SEM images of a heat-treated sample (Figure 6.3) and a heat-treated rinsed sample (Control) (Figure 6.6) were used. There were no distinct features observed in the SEM analysis of the heat-treated and control samples. However, upon exposure to conventional LE, there were two distincts features observed in the SEM (Figure 1.b); surface growth and surface degradation. Surface growth features were aprroximately < 20 um diameter and were present all over the LLZTO surface. The surface degradation was less prominent, and it appeared to be a result of etching the LLTZO due to chemical reaction or dissolution in the LE. Clearly, the results from the EIS analysis are corroborated by the instability observed in the SEM between LLZTO and LE, which manifested as surface growth and degradation.

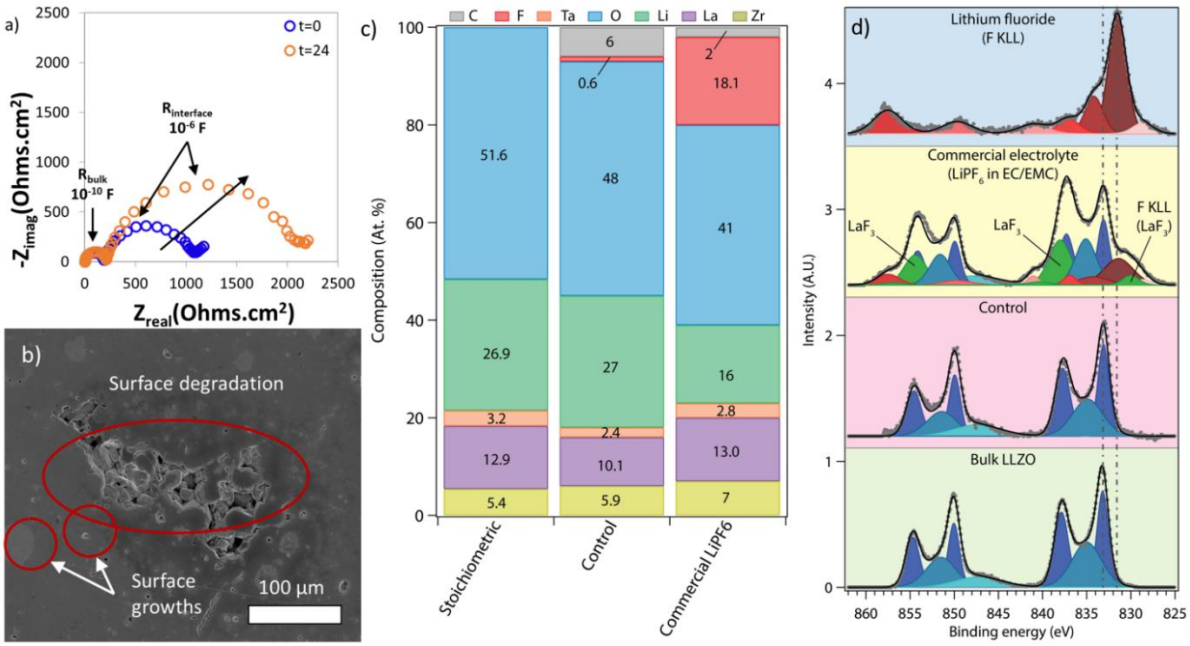

Figure 6.4 *a) EIS analysis of a graphite foil/LE/LLZTO/LE/graphite foil cell b) SEM image of LLZTO exposed to LE showing surface growth and degradation c) Composition of LLZTO before and after exposure to LE measured using XPS after 110s Ar sputtering d) Surface La 3d core spectra of bulk, control, commercial electrolyte exposed LLZTO and LiF showing the formation of* LaF_3

X-ray photoelectron spectroscopy (XPS) was used to characterize the LLZTO and LE interphase to understand the chemical interactions and compositional changes of the LLZTO surface. Figure 6.4c shows the LLZTO surface composition from the XPS anlaysis before (control) and after exposure to LE (1M $LiPF_6$ in EC:EMC LE). It was observed that the surface composition of fluorine increased from <1.0 at% to 19 at% after exposure to the LE. Since the only source of fluorine was $LiPF_6$, this provides direct evidence that the $LiPF_6$ salt participates in the reaction. However, it was difficult to determine the initiation mechanism of the reaction – whether from residual moisture, organic solvent, or reaction with the Li salt itself. The absence of a P signal confirmed that the source of F was not salt precipitation on the surface of LLZTO.

The changes in the La 3d core spectra after exposure to the 1M $LiPF_6$ in EC:EMC LE also provide insight into the nature of the reaction between the liquid electrolyte and the LLZTO. There are several possible F-containing compounds that could form and lead to the observed increase in F content, including compounds with Li, La, and Zr. As shown in Figure 6.4d, the La 3d core spectra after exposure to the $LiPF_6$ electrolyte cannot be fit using only the La 3d peaks from bulk LLZTO (blue) and the F auger peaks from LiF. As the survey scans suggested a decrease in Li content and increases in the La:Zr ratio and F content, LaF_3 species were identified as a potential additional constituent required to achieve a satisfactory fit of the experimental spectra. Peak locations for LaF_3 were established using previously-reported values for both peaks in the La 5/2 and 3/2, and also for the F KLL auger peak at 830 eV.[144] Once these component peaks were added, the improved fit shown in Figure 6.4 was achieved. The fluorine from $LiPF_6$ reacts to form compounds with both Li (red peaks) and the La (green) from LLZTO. Further evidence for multiple F-containing species is observed as additional component peaks in the F 1s and Zr 3d core spectra, as shown in Figure 6.5. The LiF, LaF_3 and other F-containing species are likely formed by the decomposition products of $LiPF_6$ and further reaction with LLZTO. Liu et al[86] have previously reported instability and interphase formation when LLZTO is exposed to SOA $LiPF_6$-based LE, however, no formation of F-compounds with La or Zr was reported. Instead, the interphase was reported to be predominantly composed of Li_2CO_3, LiF, Li_2O, and organic carbonates. The interfacial resistance was shown to increase over time due to formation of the solid electrolyte interphase as is observed in this work. Thus, through complimentary EIS, SEM and XPS analysis it could be confirmed that LLZTO was unstable against the conventional LE. This implies that an hybrid electrolyte system based on this SE/LE combination might have poor interfacial kinetics which will have a detrimental effect on the rate capability. Therefore, for the

development of a viable hybrid electrolyte approach there is a need to systematically study the chemical interactions and sources of instability between the two electrolytes.

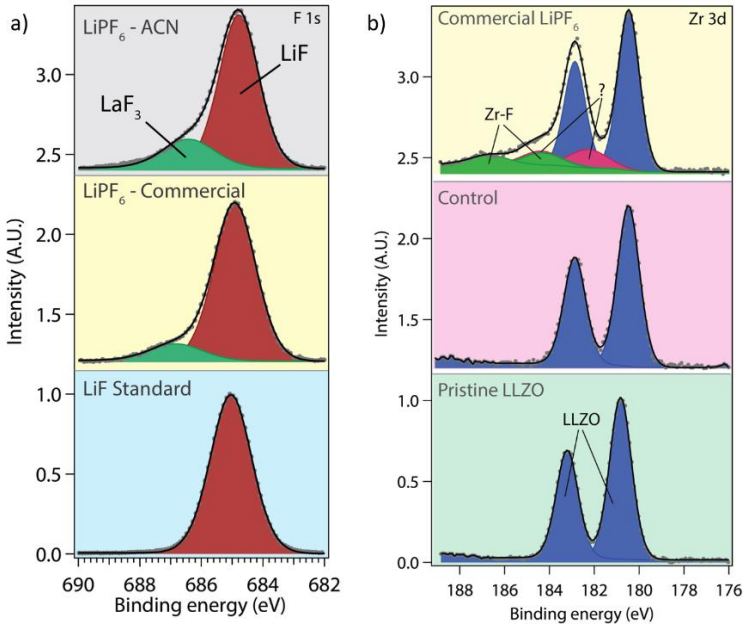

Figure 6.5 *a) Surface F 1s core spectra of standard LiF, commercial electrolyte exposed and 0.2 M $LiPF_6$ in acetonitrile exposed LLZTO b) Surface Zr 3d core spectra of bulk, control, commercial electrolyte exposed LLZTO*

6.3.2 *Evaluation of the stability of LLZTO in organic solvents.*

To provide further insight into the reaction mechanism, we performed a set of experimnets to first isolate and study the effects of different organic solvents on LLZTO, and then to study the effects of the Li salts. SEM and XPS were used to characterize the effects of organic solvents on the surface of LLZTO. For the SEM analysis, LLZTO was exposed to five relevant organic solvents (PC, DMC, ACN, DME and DOL) for 48 hours. The samples were cleaned with ethanol before SEM to ensure that there was no residual organic solvent. Figure 6.6.a shows the SEM image of LLZTO (cleaned with ethanol), which was not exposed to any organic solvent (control). From the SEM images in Figure 6.6, surface growth features were observed on the samples that were exposed to the different organic solvents. The surface growth on the LLZTO in contact with

DMC and DOL was worse than for PC, ACN and DME; however, all solvents tested showed signs of surface growth features.

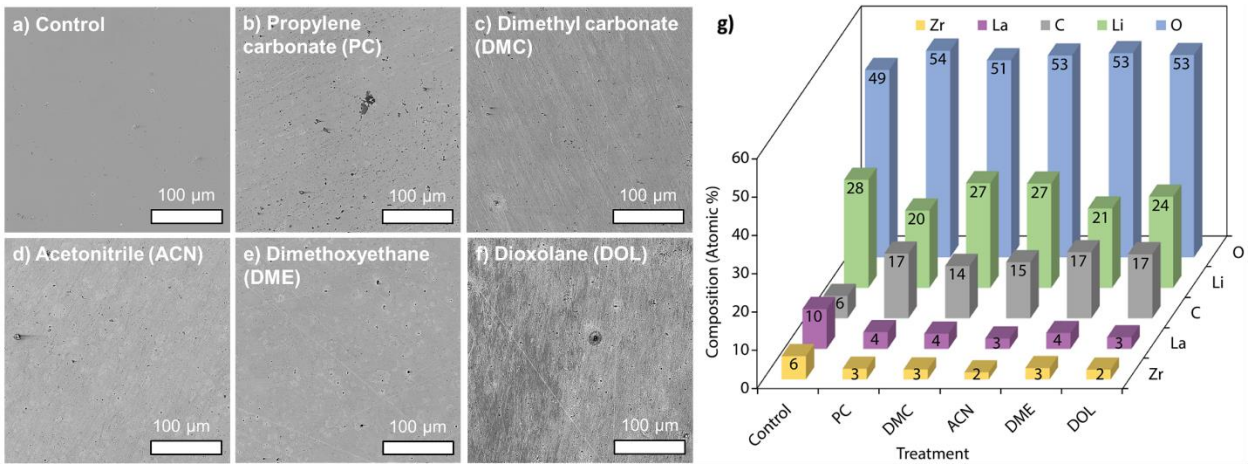

Figure 6.6 *a) SEM image of a heat-treated LLZTO samples rinsed with ethanol before SEM (control) b) c) d) e) and f) SEM images of LLZTO samples exposed to PC, DMC, and ACN, DME and DOL, respectively for 48 hours showing surface growth features g). Surface composition of LLZTO showing increase in C content before and after exposure to different organic solvent measured using XPS.*

XPS was used to characterize the surface composition of LLZTO electrolyte membrane after exposure to solvents. It can be noted from the XPS analysis that the carbon content on the surface of LLZTO was ~8-11% higher after exposure for all solvents, which displaced La, Zr and some Li. From C 1s core scans, this layer consists predominently of C-C bonding, with a small amount of lithium carbonate (Figure 6.7). The increase in carbon indicates the formation of a carbon compound upon exposure to the solvents. Since, the LLZTO surface layer composition for all the organic solvents was similar, it was concluded that LLZTO shows comparable stability with the different organic solvents. However, it is not possible to determine whether the presence of the surface layer would affect the cell resistance and the cycling performance of the cell since we could not conduct meaningful electrochemical testing without the Li salt.

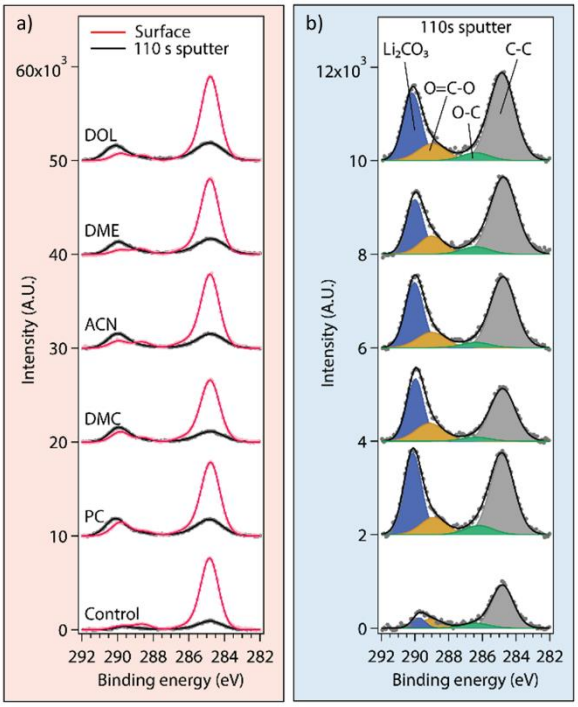

Figure 6.7 *C 1s core scans predominently of a) C-C bonding at the surface with a small amount of lithium carbonate b) C-C bonding and carbonate after 110 s sputtering*

6.3.3 *Evaluation of the stability of LLZTO with different Li salts.*

We further show that the interaction between LLZTO electrolyte and LEs are specific to the Li salt in the LE. To evaluate the interactions between different Li salts and LLZTO, three different salts were used – a) $LiPF_6$ – A fluorinated Li salt with a smaller and more reactive anion b) LiTFSI - A fluorinated Li salt with a larger and less reactive anion c) LiBOB – A non-fluorinated Li salt. The purpose of evaluating three different salts was to understand whether the instabilities were due to fluorinated salts or were salt-specific.

The first step was to use a common organic solvent for comparing the behavior of the different Li salts. Since the different solvents in the previous section seemed to have a similar effect on LLZTO, ACN was selected as the solvent maintain a single solvent system. ACN

exhibits facile desolvation kinetics for Li ions (relatively low donor number[145]), and it also exhibits a sufficiently high solubility for each Li salts and different concentration used in the study.

Separate solutions of 0.2 M $LiPF_6$, LiTFSI, and LiBOB, were prepared in ACN. These solutions were used to study the LLZTO (heat-treated at 400^{o}C) and LE interfacial kinetics and stability under static conditions. This molarity was selected to ensure that the concentration was below the solubility limit of the different salts in ACN.[146,147] The LLZTO/LE $R_{interface}$ was studied over a 48 hour period for each of the salts at room temperature in an H-cell configuration.

The EIS data for three cells of the same configuration show the average $R_{interface}$ values with the respective standard deviations (Figures 6.8 a, b). It can be observed from resistance measurements taken immediately after cell assembly that the $R_{interface}$ between LLZTO and 0.2 M LiBOB in ACN was unexpectedly high. It was also shown that $LiPF_6$ and LiTFSI initially have a relatively low $R_{interface}$ with LLZTO (28 Ohms.cm^2 and 22 Ohms.cm^2, respectively). However, it was observed that the $R_{interface}$ increases with time for all the three salts, and stabilization was only observed for LiTFSI (Figure 6.8 a, b). The resistance continually increases for LiBOB and $LiPF_6$ and was 20 times larger for LiBOB than with $LiPF_6$. In contrast, the rate of increase in resistance with LiTFSI is significantly lower than $LiPF_6$ and begins to level off after 40 hours at 55 Ohms.cm^2. Thus, from the EIS analysis LiTFSI is the most stable salt against LLZTO, which is further confirmed via XPS analysis below.

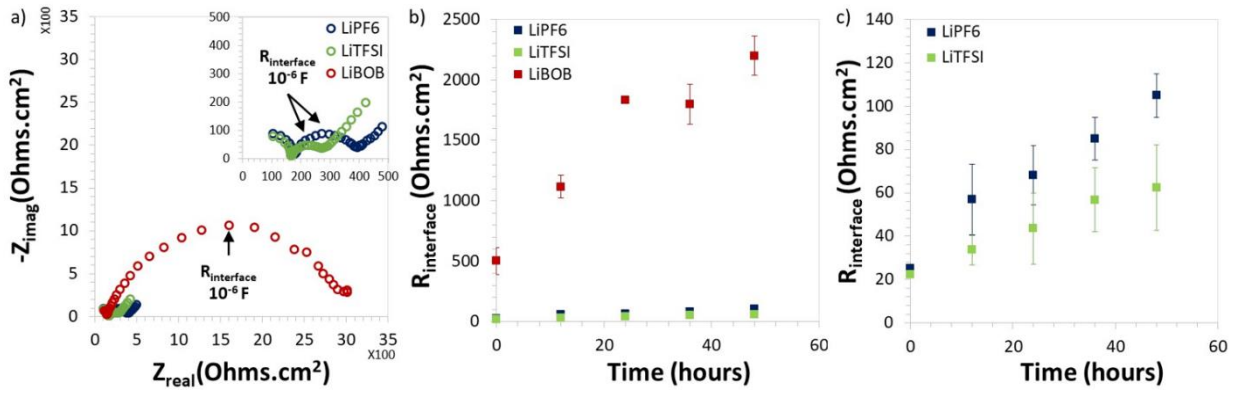

Figure 6.8 *a) Nyquist plots showing the LLZTO/LE $R_{interface}$ in an H-cell configuration (graphite foil/LE/LLZTO/LE/graphite foil) for three different salt compositions after 48 hours of assembly b)&c) LLZTO-LE $R_{interface}$ measured with time for 0.2M LE for three different salts, $LiPF_6$, LiTFSI and LiBOB in ACN; n=3 for each Li salt*

XPS analysis was performed to identify changes in composition and bonding environment on the LLZTO surface. Heat-treated LLZTO samples were exposed to the three LE for 48 hours and then rinsed with ethanol to remove residual LE on the surface of LLZTO. The composition of a heat-treated LLZTO sample rinsed with ethanol (control) was also analyzed to confirm that the changes in the surface composition were not related to exposure to the ethanol that was used to clean the surface. Figure 6.9 a shows the compositional analysis of bulk, control, and LLZTO samples exposed to pure ACN and a 0.2 M solution of $LiPF_6$, LiTFSI and LiBOB in ACN. From Figure 6.9, it can be confirmed that the surface composition of the control sample was very similar to stoichiometric LLZTO, with a slight (2-3%) decrease in La and Zr, displaced by C and O from an adventitious surface layer. Thus, it was concluded that there was no significant change in the composition of LLZTO due to ethanol cleaning. Similarly, from the effects of pure ACN on LLZTO it was concluded that there was formation of carbon and oxygen enriched layer, but no other significant changes. (Figure 6.9 b).

After evaluating the baseline samples, changes in the surface compositions of the samples exposed to the different LEs were observed using XPS. First, it was observed that upon exposure to an LE containing $LiPF_6$, the surface composition of LLZTO changed significantly with 43.9% increase in F and 10% decrease Li (Figure 6.9 b & 6.9 c). This was consistent with what was observed for the $LiPF_6$ SOA electrolytes above (Section 6.3.1). Thus, it was concluded that a similar reaction occurs here forming LiF, LaF_3, and possibly ZrF_4 on the surface leading to increasing resistances as observed in the EIS measurements. The sample exposed to the LiBOB LE exhibited no F (as expected), but a decrease in the Li content by 10% was observed. This reduced Li content may be responsible for the dramatic increase in interface resistance observed by EIS above. Additionally, the La and Zr content (Figure 6.9 e) was slightly higher than in samples exposed to ACN alone, more closely matching to the bulk LLZTO composition. This indicates that the presence of the salt reduces the interaction between the solvent and LLZTO. In contrast to the $LiPF_6$ and LiBOB, LLZTO exposed to LE with LiTFSI does not exhibit any significant change in composition. Samples exposed to LiTFSI also show La and Zr (Figure 6.9 e) concentrations higher than samples exposed to ACN alone and closer bulk LLZTO composition. Overall, LiTFSI exhibits significantly higher stability and low $R_{interface}$ against LLZTO. The XPS data are consistent with the results from the EIS analysis on LEs with the different salts, and support our hypothesis that the interactions between LLZTO and liquid electrolytes are salt specific.

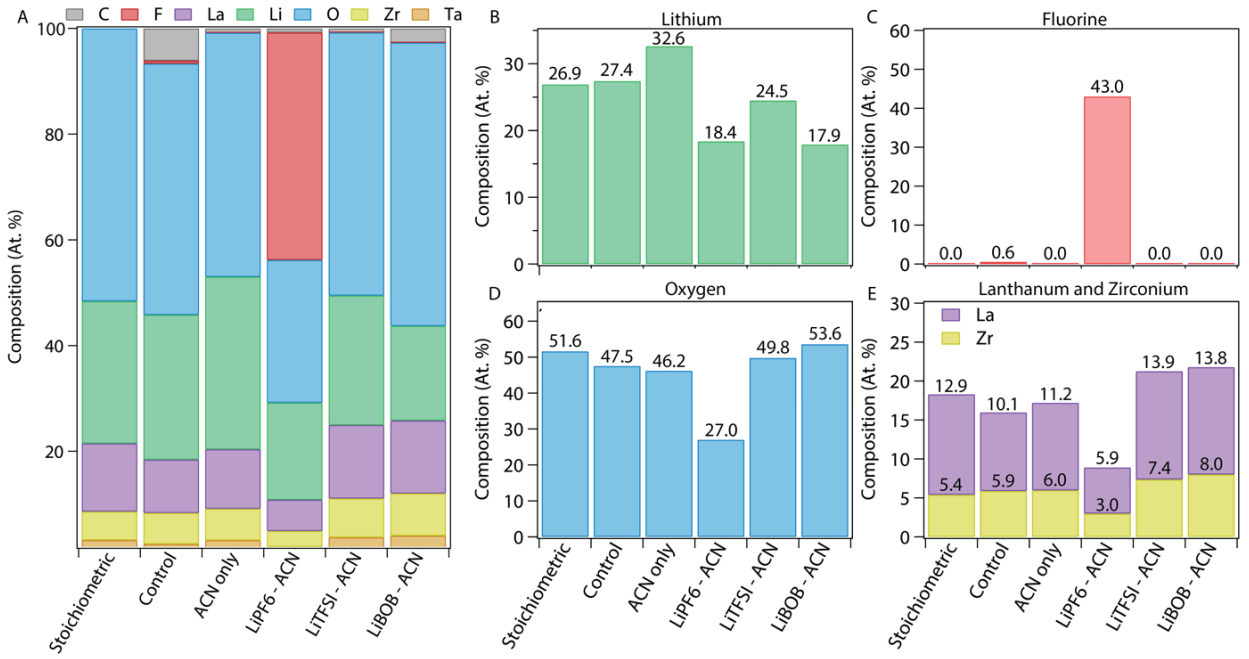

Figure 6.9 *a) Compositional analysis after 110 s of Ar sputtering for baseline LLZTO and LLZTO exposed to LE with different Li salts b) c) d) & e) Composition of different elements (Li, F, O, La, and Zr) on baseline LLZTO and LLZTO post exposure to LE with different Li salts*

6.3.4 *The effect of LiTFSI salt concentration on LLZTO/LE interfacial resistance.*

After evaluating the stability of LLZTO with different Li salts, it was concluded that LLZTO shows improved stability and lower interfacial resistance against LiTFSI under open circuit conditions. However, the resistance did grow over 48 hours to 55 Ohms.cm^2. We hypothesized that the concentration of the LiTFSI salt in the solvent may affect both the kinetics and stability of LLZTO against the LE, and thus optimizing salt concentration could further lead to reduction in $R_{interface}$. This hypothesis is motivated by following reasons: a) The effect on interfacial kinetics - i) As mentioned in section 1, the charge transfer kinetics at this interface are dependent on the de-solvation of the Li ion from the organic solvent which is dependent upon salt concentration;[139] ii) The wettability of LE to LLZTO surface and cathode could be impacted by increasing the concentration of the LE (higher concentrations would lead to poor wettability)[148],

b) The effect of interfacial stability - the voltage stability and reactivity of the LE is negatively impacted by the fraction of solvent molecules that are not coordinated to any salt species.[149,150] Clearly, the stability and kinetics of the interface is complex and affected by numerous factors. Therefore, we performed a series of experiments to test whether an optimal concentration exists to minimize the SE/LE interfacial resistance.

To investigate the effects of salt concentration, an H-cell configuration was used with LEs composed of varying concentrations of LiTFSI in ACN. From Figure 6.10 a it was observed that the $R_{interface}$ decreased from 50 Ohms.cm^2 (0.2 M LiTFSI) to <30 Ohms.cm^2 (3 M LiTFSI) as the salt concentration increased. We believe that this is due to increasing charge carrier concentration and lower free solvent concentration. However, there was an exception at 1 M LiTFSI in ACN (the reason is not well understood) where the $R_{interface}$ was observed to be higher than other concentrations. Another observation was the increase in $R_{interface}$ for 4 M concentration, which close to the solubility limit of LiTFSI in ACN. This might be due to the compromised wettability at such high concentrations.

As a general trend, it was observed that higher salt concentrations lead to a lower and more stable $R_{interface}$. The lowest $R_{interface}$ of around 20 Ohms.cm^2 was observed for a 3 M LiTFSI in ACN. The stability of LLZTO with a 3 M LiTFSI in ACN was evaluated for 7 days and it was observed that the $R_{interface}$ stabilizes within the first 2 days of assembly to 28 Ohms.cm^2. Overall, by systematically studying the effect of various organic solvents and salts, the LLZTO/LE $R_{interface}$ was reduced to 20-35 Ohms.cm^2 at RT for both 2M and 3M LiTFSI in ACN LE. It is important to note that for full cells, the utilization of a 2 M LiTFSI LE would be beneficial over 3M LiTFSI LE since a higher molarity would lead to increased polarization in the cell and negatively affect the

wettability of the LE. Note that the slight fluctuations in the $R_{interface}$ over time were likely due to the changes in ambient temperature.

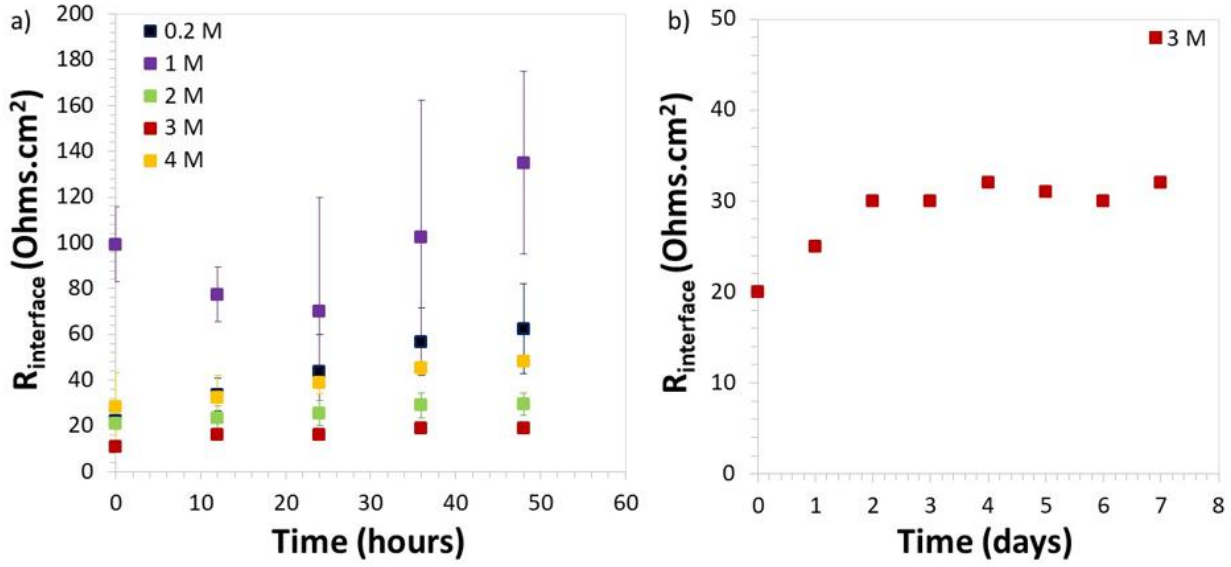

Figure 6.10 *a) LLZTO-LE $R_{interface}$ measured with time for different LiTFSI concentration in LE: n=3 for each molarity, b) LLZTO-LE $R_{interface}$ measured with time over a period of 7 days for a 3M LiTFSI in ACN*

6.3.5 *Galvanostatic cycling of Li/LLZTO/LE/Cathode cells using LiTFSI based LE.*

In the previous sections, the LLZTO/LE interface was systematically studied, and the $R_{interface}$ was successfully minimized to practical values (20-30 Ohms.cm^2) under static open circuit conditions. The next step was to evaluate the stability and performance of the LLZTO/LE interface during cycling. As a proof-of-concept demonstration, cycling was performed of a full Li/LLZTO/LE-GF/D/NCA cell in the configuration shown in Figure 6.a. A Swagelok® cell was utilized for the full cell assembly (details are given in the experimental section (Section 6.2.3.2)). Up to this point in the study, ACN was used as solvent for studying the effect of different Li salt composition and salt concentration on interfacial resistance, due to its sufficiently high solubility for the respective salt and different concentrations used (as mentioned in Section 6.3.3). However,

ACN posed two main challenges when we attempted to use it as a solvent in a full cell configuration – a) ACN reacted with the components of a Swagelok® configuration and the seal used to isolate the liquid from the Li electrode; b) Due to its high vapor pressure, there was a loss of electrolyte observed over time from the cell. Thus, PC was chosen over ACN as the solvent for full cells due to its low vapor pressure, compatibility with the Swagelok® similar solvation/desolvation kinetics to ACN.[151]

The cell was galvanostatically cycled for 10 cycles between 2.5 and 4.2 V versus Li/Li+ at a C/20 rate (0.15 mA/cm^2 current density). Figure 6.11 b shows the EIS measurement of full-cell impedance after the 1st and 10th cycle. $R_{interface}$ grows by a factor of 2 after 10 cycles. However, in a two-electrode configuration it was difficult to determine whether the increase in resistance is due the Li/LLZTO, LLZTO/catholyte, or LE/cathode interface. Figure 6.11 c shows the voltage profile for the 1st, 2nd and the 10th cycle. It was observed from Figure 6.11 c that there was an irreversible capacity loss in the 1st cycle, which we commonly observe for NCA cathodes. After the 1st cycle, the utilization of the cathode was approximately 100%, with a capacity retention of 98.5% over 10 cycles and minimal overpotentials. Although the overall capacity retention and Coulombic efficiency were high, there was some deviation in the voltage profile at high voltages during a few charge cycles (Figure 6.11 d). These deviations led to excess capacity for those charge cycles and low Coulombic efficiencies. However, the performance was recovered in consequent cycles. We believe that the deviations in the voltage profile may be related to the stability of the LLZTO/LE interface under cycling conditions. From these data it can be concluded that higher concentration LiTFSI based electrolytes are compatible with LLZTO and could provide a viable route for the successful implementation of the LE in the GPE used for hybrid electrolytes.

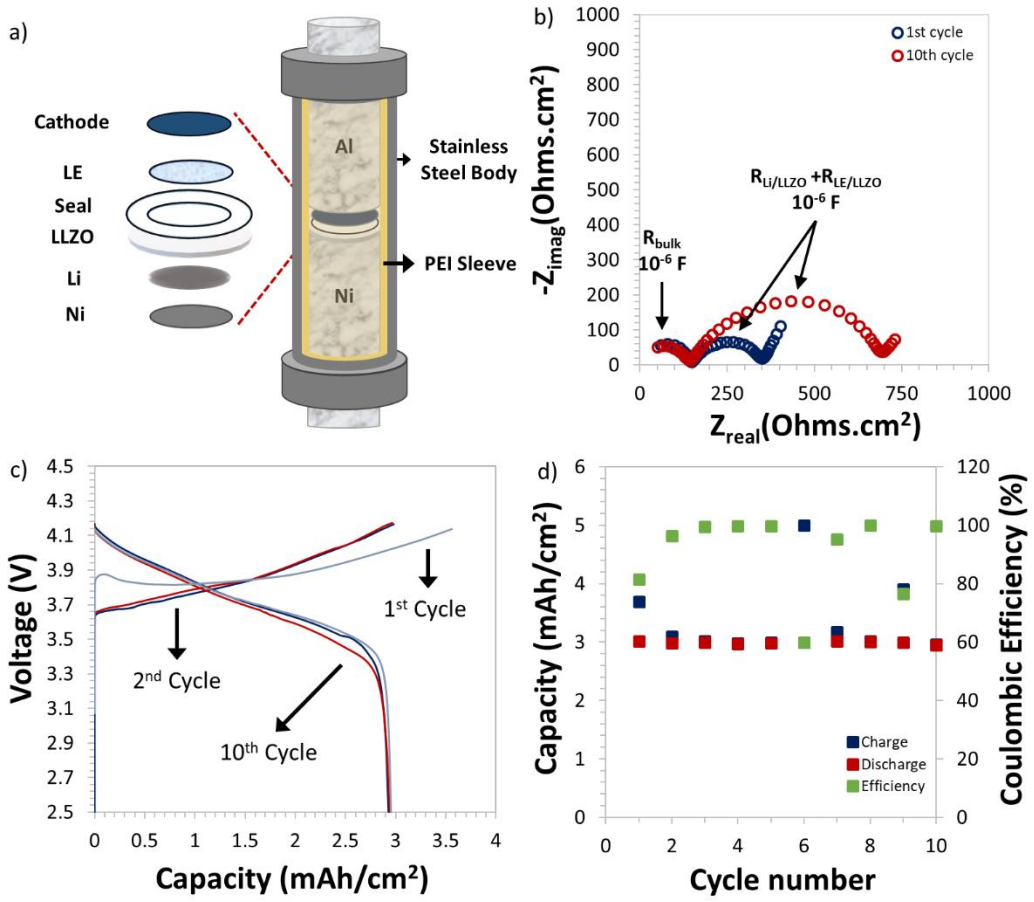

Figure 6.11 *a) Schematic of a Swagelok® cell for full cell cycling b) EIS plots of a full cell after 1st and 10th cycle step c) Voltage profile of a cell with capacity for three cycles d) Evolution of capacity and coulombic efficiency with cycle number for a full cell configuration.*

6.4. Implications

There are several important implications of the formation of an intermediate surface layer between LLZTO and the LE. First, the reaction between the LLZTO and the LEs was spontaneous and took place under open circuit conditions; it occurred even on exposing the LLZTO sample to the LE alone. Also, in contrast to previous studies, we observed a direct reaction between bulk LLZTO and a 1M $LiPF_6$ EC/EMC LE , which led to the formation of LaF_3 and Zr-F side products in addition to LiF. Second, from the observations of this study, it is clear that the Li salts are what leads to propogation of a reaction between LLZTO and LE, and not the solvent alone. This was

concluded from the varying interaction of LLZTO with LEs containing different Li salts and the same organic solvent. If the interfacial layer were instead formed as a result of reactivity between LLZTO and the solvent, then instability should be observed for all of the salts tested, which was not the case. Thus, by selecting the Li salts that exhibit stable behavior with LLZTO, it could be possible to successfully implement the hybrid electrolyte approach. Third, from the experimental data and chemical characterization, it is possible to propose a potential reaction pathway between the LLZTO and the LEs. However, further study is required to elucidate the exact mechanism of initiation. Further insights into the reaction mechanism could be gained through theoretical modelling. Finally, there are still both scientific and engineering challenges to overcome, however, this study provided promising results which demonstrate stability between LLZTO and LE. Thus, it is crucial to consider the results of this work while selecting an LE for a gel polymer electrolyte since the LE would be in contact with the LLZTO at the interface even though most of it would be entrapped in the GPE.

6.5. Conclusion

In this study we first validated the instability between LLZTO and SOA LE (1M $LiPF_6$ EC/EMC), which was observed in previous reports.[86,87] However, the goal of this study was to identify the constituent of the LE that causes the instability. To do this, the effects of each constituent were isolated for a range of solvents and salts. It was found that upon exposure to organic solvents, LLZTO forms a C-rich layer on its surface, which may have benign effects on the electrochemical performance. Most importantly, it was found that the stability of LLZTO was highly dependent on the Li salt. The least compatible salts were $LiPF_6$ and LiBOB, resulting in a high resistance that increased over time ($R_{interface}$ with (a) $LiPF_6$- 120 Ohms.cm^2 and (b) LiBOB – 2000 Ohms.cm^2). Conversely, the greatest stability was achieved using LiTFSI (0.2 M) ($R_{interface}$,55 Ohms.cm^2).

The range of reactiviy between LLZTO and the Li salts (all in the same organic solvent) provides further evidence that the solvent alone does not play a major role in the chemical reactions. Having identified a compatible salt, the effect of molarity on interface stability and kinetics was studied. It was determined that the 3 M LiTFSI minimized the interfacial resistance to < 30 Ohm.cm^2 and maximized stability with LLZTO. Stable preliminary cycling performance of a Li/LLZTO/LE/NCA cathode cell was demonstrated using a 2M LiTFSI LE. The cell was cycled at a C/20 rate for ten cycles at room temperature with close to 100% cathode utilization and minimal capacity fade. While these cycling data demonstrate progress in stabilizing the LE/SE interfae, further efforts to better understand the interface are needed. Specifically, computational modeling is needed to better understand reaction pathways. Overall, it was shown that through the rational selection of the LE composition, it is possible to achieve low and stable interface resistance for LLZTO and LE which can then be used in hybrid electrolytes for enabling metallic Li anodes.

6.6. Acknowlegdement

The authors would like to acknowledge the support from LG Chem Ltd. N025470 and ARPA-E DE-AR0000653 for this project. Arushi Gupta and Jeff Sakamoto would like to acknowledge Dr. Jeongbeom Lee at LG Chem Ltd. for their helpful insights for this work. Arushi Gupta: Conceptualization, Data curation, Methodology, Resources, Writing - original draft, Formal analysis, Investigation, Writing - review & editing. Eric Kazyak: Resources, Writing – original draft, Data curation, Formal analysis, and Investigation of XPS data, Writing - review & editing. Neil P. Dasgupta: Resources, Formal analysis of XPS data, Writing - review & editing. Jeff Sakamoto: Conceptualization, Methodology, Funding acquisition, Supervision, Writing - original draft, Formal analysis, Writing - review & editing.

Chapter 7 Conclusions and Future Work

7.1. Conclusions

The primary objective of this thesis was to investigate and resolve the possible challenges which might arise in Li metal batteries employing a hybrid electrolyte. To do so, the underlying assumptions for the successful implementation of the hybrid electrolyte approach were studied. The two main assumptions considered were – a) the electrochemical properties of the GPE will comply with the cathode with any changes in temperature and pressure; b) the LLZTO would have favorable kinetics and be (electro)chemically stable against the GPE interface. To evaluate the validity of these assumptions, first, a comprehensive understanding of the (electro)chemical behavior of a model polymer electrolyte was developed and then the transport kinetics and (electro)chemical performance of the LLZTO/GPE interface that arises in a hybrid electrolyte approach was investigated. Since the GPE is composed of a polymer and an LE, the interfacial properties of LLZTO with both the electrolytes were evaluated independently. With the knowledge gained from this approach, guidelines and engineering approaches can be provided for the successful implementation of the hybrid electrolyte in Li metal batteries.

Specifically the goals of this dissertation were laid out in three separate Chapters which constitute the Chapters 4, 5 and 6 of this thesis document - Chapter 4) Studying the effects of temperature and pressure on electrochemical performance of a polymer electrolyte (PEO-LiTFSI); Chapter 5) Understanding the factors controlling the polymer/LLZTO interfacial kinetics; Chapter 6) Electrochemical and Surface Chemistry Analysis of Lithium Lanthanum Zirconium Tantalum

Oxide (LLZTO)/Liquid Electrolyte (LE) Interfaces. There were several important conclusions made from these studies which have been discussed below.

7.1.1. Studying the effects of temperature and pressure on electrochemical performance of a polymer electrolyte

As discussed, for the implementation of GPEs in a cathode it is important to understand the external variables (temperature and pressure), which may govern the electrochemical performance of the GPE. The approach used in this thesis was to first study the effects of external variables on the kinetics and stability of a model polymer electrolyte (PEO-LiTFSI) and then this knowledge can be further used to select and successfully integrate a GPE with appropriate properties for the catholyte. A symmetric cell configuration Li/PEO-LiTFSI/Li was used in the study. From the results it was concluded that the bulk and interfacial kinetics were strongly dependent on temperature and stack pressure. First, the bulk conductivity of the polymer improved by three order of magnitude (10^{-6} to 10^{-3} S cm^{-1}) with increasing temperature from 30 to 80°C, with a sharp decrease in activation energy around the melting temperature (55°C). This is because, above the melting point the lower conductivity crystalline domains in the polymer melt thus, leading to a higher conductivity amorphous polymer. This also compromises the elastic properties of a polymer due to the loss of the hard-crystalline domains. In contrast, the Li/PEO-LiTFSI interfacial kinetics did improve with temperature, however, there was no sharp change in activation energy observed. Thus, from these results it was concluded that while selecting a gel polymer electrolyte it would be important to consider the temperatures for thermal transitions of the GPE. Second, it was observed that a critical stack pressure (pressure at and above which the interfacial impedance is invariant with increasing pressure) was required to establish a good electrode/electrolyte interfacial contact. Since the cathode undergoes volumetric expansion and

contraction during cycling, it is possible to lose the interfacial contact between the GPE and cathode particles. Thus, a similar approach can be used to evaluate a critical stack pressure required to maintain a good interfacial contact between the GPE and cathode particles during cycling. We believe the correlations and observations made in this study would provide guidance for the successful implementation of the gel polymer catholytes.

7.1.2. Understanding the factors controlling the GPE/LLZTO interfacial kinetics

The new interfaces formed between the ionic conductors in a hybrid electrolyte can result in significant charge transfer resistances, limiting the kinetics at those interfaces. Thus, it is critical to evaluate the factors that control the LLZTO/GPE interface kinetics, chemical and electrochemical stability, for the viability of a hybrid electrolyte approach. In this thesis the approach was to study the interface of LLZTO with each of the constituent of the GPE – polymer electrolyte and LE. This would enable us to identify and mitigate the challenges and limitations of each the interfaces. The knowledge gained by studying the factors that control the polymer/LLZTO interface and the LLZTO/LE interface can then be used to improve the LLZTO/GPE charge transfer kinetics.

7.1.2.1. Understanding the factors controlling the polymer/LLZTO interfacial kinetics

A low interfacial resistance (<~100 Ohms cm^2) is required for facile charge transport across a polymer electrolyte/LLZTO interface. However, it has been previously reported that the polymer electrolyte/LLZTO $R_{interface}$ was high.[125,152,153] Thus, the goal in Chapter 5 was to validate the results of the previous reports and investigate the origin of this high $R_{interface}$. Using a model polymer electrolyte (PEO-LiTFSI, 27:1 [EO]:[Li] ratio) in trilaminar cell configuration, the PEO-LiTFSI/LLZTO $R_{interface}$ was evaluated to be 95 kOhms.cm^2. It was determined that LLZTO

surface impurities and abrupt changes in Li-ion concentration between the PEO-LiTFSI/LLZTO electrolyte contributes to the high resistance. On removing surface impurities using heat-treatment of LLZO, the $R_{interface}$ was reduced to 180 Ohms.cm^2 at 30°C. Optimization of Li salt concentration in PEO to 15:1, resulted in reduction of $R_{interface}$ from 1.6 kOhms.cm^2 to 421 Ohms.cm^2. Thus, by systematically studying the polymer/LLZTO interface and understanding the underpinning mechanisms that govern that interface the charge transfer kinetics were significantly improved. We believe that the comprehensive knowledge gained in this study, provides guidelines for the successful implementation of a GPE with LLZTO SE in a Li metal battery.

7.1.2.2. Electrochemical and Surface Chemistry Analysis of Lithium Lanthanum Zirconium Tantalum Oxide (LLZTO)/Liquid Electrolyte (LE) Interfaces

The stability of the LLZTO/LE interface is essential to enable hybrid electrolytes, since the LE in the GPE would be in contact with the LLZTO SE. However, it has been previously shown that the LLZTO reacts with $LiPF_6$-based SOA LEs.[86] The goal in Chapter 6 was to identify the source of this instability, and to propose approaches to ameliorate the incompatibility. This was achieved by studying and isolating the effects of organic solvents and Li salts present in the LE on LLZTO. The results indicated that Li salts lead to propogation of a reaction between LLZTO and LE, and not the solvent alone. This was concluded from the varying interaction of LLZTO with LEs containing different Li salts and the same organic solvent. If the interfacial layer were instead formed as a result of reactivity between LLZTO and the solvent, then instability should be observed for all of the salts tested, which was not the case. Thus, by selecting the Li salts that exhibit stable behavior with LLZTO, the charge transport at the LLZTO/LE interface can be significantly improved. For example, $LiPF_6$ salt reacts with LLZTO to form LiF, LaF_3 and ZrF_4, which leads to an increased SE/LE interfacial resistance ($R_{interface}$). The $R_{interface}$ after reacting with

$LiPF_6$ and LiBOB salts were ~120 and 2000 Ohms.cm^2, respectively. However, LiTFSI salt is compatible with LLZTO with $R_{interface}$ ~55 Ohms.cm^2. Further, optimization of the LiTFSI salt concentration (3M) resulted in an $R_{interface}$ of ~30 Ohms.cm^2. Thus, from these results we believe that LiTFSI is compatible with LLZTO. We also demonstrate preliminary cycling of Li/LLZTO/LiTFSI-basedLE/NCA cells with ~100% utilization and 98.5% capacity retention over 10 cycles.

The results of Chapter 5 & 6 show a significant progress of the charge transfer kinetics of the new interfaces that will be formed in a hybrid electrolyte approach and thus, are a step towards the successful implementation of hybrid electrolytes in Li metal batteries.

7.2. Future work

Overall, with the methodology, results and conclusions of this thesis a fundamental understanding of the effects of external variables, surface treatment, charge carrier concentration and chemical reactions on the electrochemical performance of the different components which will be employed in a hybrid electrolyte cells were developed. With this comprehensive knowledge gained on the different aspects of a hybrid electrolyte approach in this thesis, there are several future steps proposed, with the support of preliminary data, for the implementation of GPE with LLZTO SE.

7.2.1. GPE-based Catholyte development

Since in a GPE, the major charge transport is through the LE entrapped in the gel polymer matrix – we suggest selecting a polymer electrolyte with a high melting point (> 100°C) and suitable elastomeric properties to maintain good interfacial contact with the cathode particles. Additionally, the GPE should have a high ionic conductivity (~10^{-4} S cm^{-1}) at room temperature,

excellent ion solvating ability, a high Li ion transference number and a high resistance to oxidative degradation. The compatibility of the GPE with LLZTO SE should then be evaluated. For example, an LiTFSI based LE would be preferred in the GPE based on the results of Chapter 6. Based on our preliminary results, Polyacrylonitrile (PAN)-based catholyte composed of PAN, LiTFSI Li salt and propylene carbonate (PC) and ethylene carbonate (EC) liquids immobilized in the PAN gel looks promising.

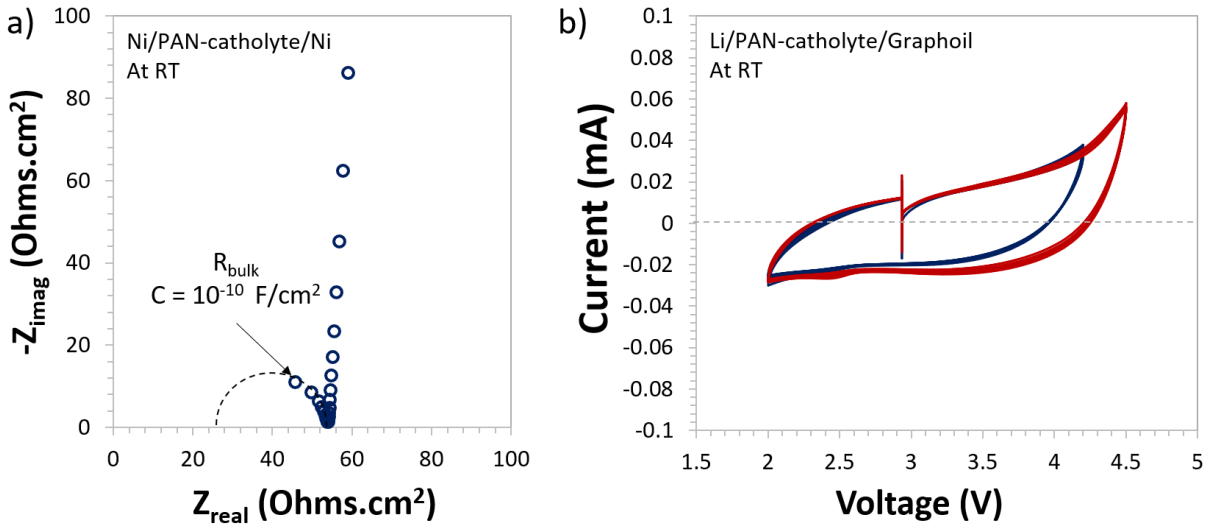

Figure 7.1 *a) Nyquist plot for PAN-based catholyte at RT. The conductivity measurements were conducted over five samples. b) Voltage stability of PAN-based catholyte evaluated over to voltage ranges – 2 to 4.2 V, 10 cycles and 2 to 4.5 V, 10 cycles*

The PAN-based catholyte was fabricated by mixing the precursors at a 100^{o}C and then cast. Then, preliminary results for the room temperature conductivity and voltage stability of the catholyte were evaluated. The conductivity of the PAN-based catholyte was 2.1*10^{-3} S.cm^{-1} at RT (Figure 7.1 a). The cell configuration used for evaluating the voltage stability was Li/PAN-based catholyte/Graphoil. From Figure 7.1 b it was observed that the catholyte was stable up to 4.2V however, at 4.5 V we start to observe a reduction peak. The origin of the peak was unclear and

might be pertaining to impurities. Further analysis to determine the origin of the reduction peak is required. However, since the cut-off for operating voltages for NCA cathode in a full cell was 4.2 V, the catholyte should be stable in that range.

After evaluating the ionic conductivity and voltage stability, next the interfacial kinetics between the catholyte and LLZTO were evaluated. A trilaminar cell configuration with blocking electrodes (Ni/catholyte/LLZO/catholyte/Ni) was used for measuring the $R_{interface}$ between the two. The LLZTO samples were heat treated at 700°C to eliminate surface impurities before cell assembly and the composition of the catholyte was evaluated by studying the ionic conductivity as a function of salt concentration (methodology used from Chapter 5). The cells were then tested in a Swagelok® using electrochemical impedance spectroscopy at RT to minimize the loss of LE from the gel. The $R_{interface}$ starts around 60 Ohms.cm^2 and then increases (Figure 7.2 a) to stabilize at around 68 Ohms.cm^2. From these results the $R_{interface}$ between LLZTO and the catholyte shows stable behavior as can be observed in Figure 7.2 b. Slight variation in the bulk and the interfacial impedances can be due to the temperature changes in the environment.

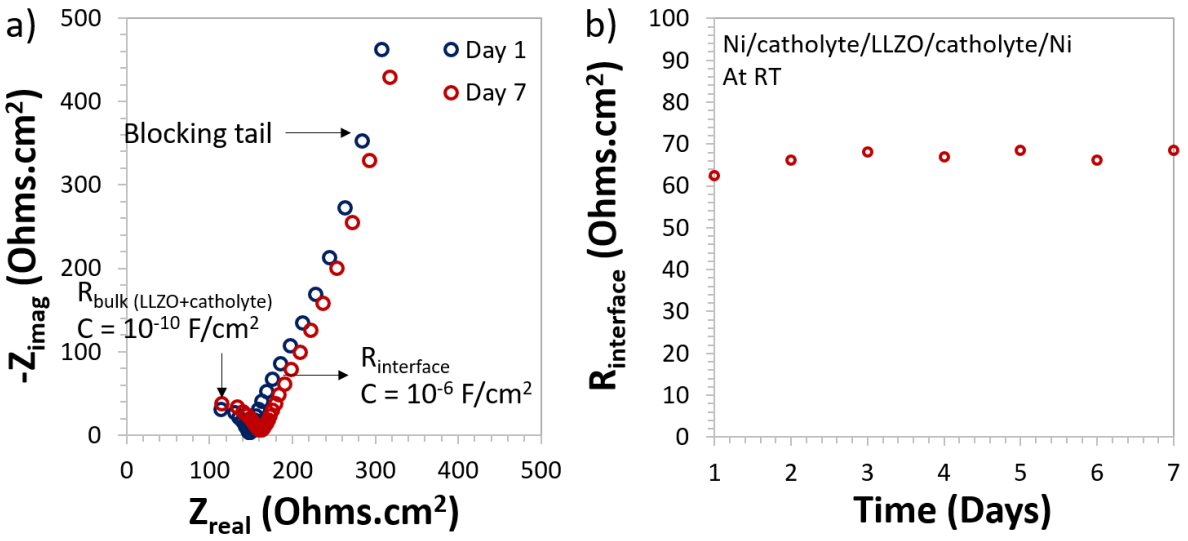

Figure 7.2 *a) Nyquist plot showing the interfacial impedance ($R_{interface}$) between the catholyte and LLZO in a trilaminar cell configuration with blocking electrodes. b) Interfacial impedance measured using EIS over a period of 7 days*

The preliminary results of the PAN-based catholyte's ionic conductivity, electrochemical stability and interfacial kinetics are promising. However, a comprehensive study should be done to further characterize the performance PAN-based catholytes. A few important studies would include a) Since the retention of the LE in the PAN matrix can significantly change with temperature and pressure, it is important to study the rate at which the LE is lost from the polymer matrix with temperature and pressure and how does that impact the electrochemical performance of the catholyte; b) An electrochemical voltage stability up to 4.7 V would allow for the utilization of high voltage cathodes. Thus, due to the instability observed in CV, the cause for the electrochemical instability of the catholyte should be evaluated.

7.2.2. Composite Cathode development

After showing the promising results with the PAN-based catholyte we wanted to demonstrate the steps for the development of a composite cathodes employing PAN-based

catholytes. First, the composite cathodes were fabricated by infiltration of a PAN-based catholyte in commercial NCA cathode by hot calendaring at 100°C.

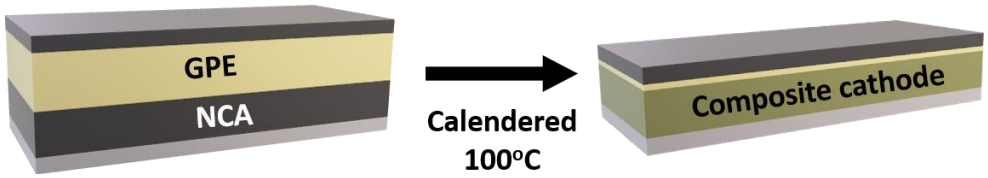

Figure 7.3 *Schematic showing fabrication of composite cathode by infiltrating GPE in cast commercial NCA cathode*

After the fabrication of the composite cathode the next step was to study its interfacial resistance ($R_{interface}$) against LLZTO to evaluate the viability of the hybrid electrolyte approach. EIS measurement were recorded at room temperature over a week using a trilaminar configuration Al/infiltrated-cathode/LLZO/infiltrated-cathode/Al (Figure 7.4). We found that $R_{interface}$ increases with time (Figure 7.4 b) from around 30 Ohms.cm^2 to around 80 Ohms.cm^2 after a week for different samples. The data here has error bars representing the lowest and the highest resistance for different samples since in our experience the $R_{interface}$ is sensitive to the sample preparation. The change in the bulk resistance can be related to variation in ambient temperature. Although the $R_{interface}$ is still within the target resistance of <100 Ohms cm^2, the increase in resistance over time shows some incompatibility. Thus, with the systematic approach used in Chapter 6, there is a need to evaluate the cause for the increase in resistance.

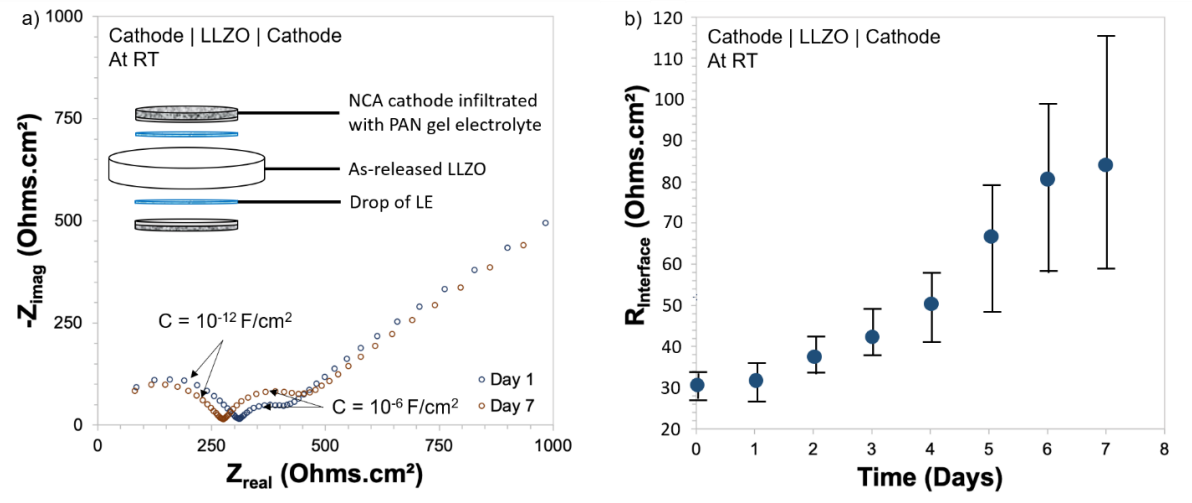

Figure 7.4 *a) Nyquist plot for infiltrated cathode/LLZO thin film/infiltrated cathode at RT. The $R_{interface}$ was measured over 3 cells. b) Infiltrated cathode-LLZO thin film average $R_{interface}$ over 7 days.*

After the optimization of composite cathode/LLZTO interface the next steps towards the implementation of hybrid electrolytes would include evaluating – a) the stability of the composite cathode using cyclic voltammetry b) the cycling performance of a composite cathode half-cell, with the configuration Li/GPE/composite cathode, using galvanostatic cycling at relevant C-rates (C/10 to 1C) at room temperature; c) the effects of infiltration of GPE in the cathode on capacity utilization and fade using SEM and galvanostatic cycling; d) the cycling performance of a full cell employing the hybrid electrolyte approach, with the configuration Li/LLZTO/composite cathode, using galvanostatic cycling at relevant C-rates (C/10 to 1C) at room temperature.

References

(1) Zedalis, R. J. International Energy Law. *Int. Energy Law* **2017**. https://doi.org/10.4324/9781315252056.

(2) Energy, G. CO_2 Status Report. *IEA (International Energy Agency) Paris, Fr.* **2019**.

(3) U.S. Energy Information Administration. Annual Energy Outlook 2020 - Industry. **2020**.

(4) Btu, Q. U . S . Primary Energy Consumption by Source and Sector , 2007. **2007**, *2007* (April), 2007.

(5) Grid Integration Tech Team and Summary Report on EVs at Scale and the U . S . Electric Power System. No. November 2019.

(6) Srinivasan, V. Batteries for Vehicular Applications. *Batter. Manuf. Electr. Hybrid Veh.* **2011**, *283* (September 2008), 135–152.

(7) DOE, U. Batteries 2018 Annual Progress Report. *J. Chem. Inf. Model.* **2018**, *53* (9), 1689–1699. https://doi.org/10.1017/CBO9781107415324.004.

(8) Barak, M. *Electrochemical Power Sources: Primary and Secondary Batteries*; IET, 1980.

(9) Goodenough, J. B.; Park, K.-S. The Li-Ion Rechargeable Battery: A Perspective. *J. Am. Chem. Soc.* **2013**, *135* (4), 1167–1176.

(10) Goodenough, J. B. How We Made the Li-Ion Rechargeable Battery: Progress in Portable and Ubiquitous Electronics Would Not Be Possible without Rechargeable Batteries. John B. Goodenough Recounts the History of the Lithium-Ion Rechargeable Battery. *Nat. Electron.* **2018**, *1* (3), 204. https://doi.org/10.1038/s41928-018-0048-6.

(11) Huggins, R. *Advanced Batteries: Materials Science Aspects*; Springer Science & Business

Media, 2008.

(12) Van Noorden, R.; Richard Van Noorden. A Better Battery. *Nature* **2014**, *507* (7490), 26–28. https://doi.org/10.1038/507026a.

(13) Bruce, D.; Haresh, K.; Jean-Marie, T. Electrical Energy Storage for the Grid: A Battery of Choices. *Science (80-.).* **2011**, *334* (6058), 928–935.

(14) Etacheri, V.; Marom, R.; Elazari, R.; Salitra, G.; Aurbach, D. Challenges in the Development of Advanced Li-Ion Batteries: A Review. *Energy Environ. Sci.* **2011**, *4* (9), 3243–3262. https://doi.org/10.1039/c1ee01598b.

(15) Wood, K. N.; Noked, M.; Dasgupta, N. P. Lithium Metal Anodes: Toward an Improved Understanding of Coupled Morphological, Electrochemical, and Mechanical Behavior. *ACS Energy Lett.* **2017**, *2* (3), 664–672. https://doi.org/10.1021/acsenergylett.6b00650.

(16) Bruce, P. G.; Freunberger, S. A.; Hardwick, L. J.; Tarascon, J. M. Li-O_2 and Li-S Batteries with High Energy Storage. *Nat. Mater.* **2012**, *11* (1), 19–29. https://doi.org/10.1038/nmat3191.

(17) Dudney, N. J.; Li, J. Using All Energy in a Battery. *Science (80-.).* **2015**, *347* (6218), 131–132. https://doi.org/10.1126/science.aaa2870.

(18) Albertus, P.; Babinec, S.; Litzelman, S.; Newman, A. Status and Challenges in Enabling the Lithium Metal Electrode for High-Energy and Low-Cost Rechargeable Batteries. *Nat. Energy* **2018**, *3* (1), 16–21. https://doi.org/10.1038/s41560-017-0047-2.

(19) Garcia-Mendez, R.; Smith, J. G.; Neuefeind, J. C.; Siegel, D. J.; Sakamoto, J. Correlating Macro and Atomic Structure with Elastic Properties and Ionic Transport of Glassy Li_2S-P_2S_5 (LPS) Solid Electrolyte for Solid-State Li Metal Batteries. *Adv. Energy Mater. n/a* (n/a), 2000335. https://doi.org/doi:10.1002/aenm.202000335.

(20) Ma, C.; Cheng, Y.; Yin, K.; Luo, J.; Sharafi, A.; Sakamoto, J.; Li, J.; More, K. L.; Dudney, N. J.; Chi, M. Interfacial Stability of Li Metal-Solid Electrolyte Elucidated via in Situ Electron Microscopy. *Nano Lett.* **2016**, *16* (11), 7030–7036. https://doi.org/10.1021/acs.nanolett.6b03223.

(21) Murugan, R.; Thangadurai, V.; Weppner, W. Fast Lithium Ion Conduction in Garnet-Type Li7La 3Zr2O12. *Angew. Chemie - Int. Ed.* **2007**, *46* (41), 7778–7781. https://doi.org/10.1002/anie.200701144.

(22) Imanishi, N.; Yamamoto, O. Polymer Electrolytes for Lithium-Air Batteries. *Lithium Batter.* **2013**, No. 6, 217–232. https://doi.org/10.1002/9781118615515.ch10.

(23) Quartarone, E.; Mustarelli, P. Electrolytes for Solid-State Lithium Rechargeable Batteries: Recent Advances and Perspectives. *Chem. Soc. Rev.* **2011**, *40* (5), 2525–2540. https://doi.org/10.1039/C0CS00081G.

(24) Manthiram, A.; Yu, X.; Wang, S. Lithium Battery Chemistries Enabled by Solid-State Electrolytes. *Nat. Rev. Mater.* **2017**, *2* (4), 16103. https://doi.org/10.1038/natrevmats.2016.103.

(25) Munshi, M. Z. A. *Handbook of Solid State Batteries and Capacitors*; World Scientific, 1995.

(26) Thompson, T.; Yu, S.; Williams, L.; Schmidt, R. D.; Garcia-Mendez, R.; Wolfenstine, J.; Allen, J. L.; Kioupakis, E.; Siegel, D. J.; Sakamoto, J. Electrochemical Window of the Li-Ion Solid Electrolyte $Li_7La_3Zr_2O_{12}$. *ACS Energy Lett.* **2017**, *2* (2), 462–468.

(27) *United States Advanced Battery Consortium LLC; USABC Goals for Advanced High-Performance Batteries for Electric Vehicle (EV) Applications. 2019*.

(28) Sharafi, A.; Kazyak, E.; Davis, A. L.; Yu, S.; Thompson, T.; Siegel, D. J.; Dasgupta, N.

P.; Sakamoto, J. Surface Chemistry Mechanism of Ultra-Low Interfacial Resistance in the Solid-State Electrolyte $Li_7La_3Zr_2O_{12}$. *Chem. Mater.* **2017**, *29* (18), 7961–7968. https://doi.org/10.1021/acs.chemmater.7b03002.

(29) Fenton, D. E.; Parker, J. M.; Wright, P. V. Complexes of Alkali Metal Ions with Poly(Ethylene Oxide). *Polymer (Guildf).* **1973**, *14* (11), 589. https://doi.org/10.1016/0032-3861(73)90146-8.

(30) Armand, M. B. J. m. Chabagno, MJ Duclot. In *Second International Meeting on Solid Electrolytes*; 1978; pp 20–22.

(31) Di Noto, V.; Lavina, S.; Giffin, G. A.; Negro, E.; Scrosati, B. Polymer Electrolytes: Present, Past and Future. *Electrochim. Acta* **2011**, *57* (1), 4–13. https://doi.org/10.1016/j.electacta.2011.08.048.

(32) Pesko, D. M.; Timachova, K.; Bhattacharya, R.; Smith, M. C.; Villaluenga, I.; Newman, J.; Balsara, N. P. Negative Transference Numbers in Poly (Ethylene Oxide)-Based Electrolytes. *J. Electrochem. Soc.* **2017**, *164* (11), E3569--E3575.

(33) Doyle, M.; Fuller, T. F.; Newman, J. The Importance of the Lithium Ion Transference Number in Lithium/Polymer Cells. *Electrochim. Acta* **1994**, *39* (13), 2073–2081. https://doi.org/10.1016/0013-4686(94)85091-7.

(34) Handbook of Solid State Batteries. *Materials and Energy*. WORLD SCIENTIFIC January 12, 2015, p 836. https://doi.org/doi:10.1142/9487.

(35) Dias, F. B.; Plomp, L.; Veldhuis, J. B. J. Trends in Polymer Electrolytes for Secondary Lithium Batteries. *J. Power Sources* **2000**, *88* (2), 169–191. https://doi.org/10.1016/S0378-7753(99)00529-7.

(36) Zhou, D.; Shanmukaraj, D.; Tkacheva, A.; Armand, M.; Wang, G. Polymer Electrolytes

for Lithium-Based Batteries: Advances and Prospects. *Chem* **2019**, *5* (9), 2326–2352. https://doi.org/10.1016/j.chempr.2019.05.009.

(37) Yue, L.; Ma, J.; Zhang, J.; Zhao, J.; Dong, S.; Liu, Z.; Cui, G.; Chen, L. All Solid-State Polymer Electrolytes for High-Performance Lithium Ion Batteries. *Energy Storage Mater.* **2016**, *5*, 139–164. https://doi.org/10.1016/j.ensm.2016.07.003.

(38) Xu, K. Electrolytes and Interphases in Li-Ion Batteries and Beyond. *Chem. Rev.* **2014**, *114* (23), 11503–11618. https://doi.org/10.1021/cr500003w.

(39) Mindemark, J.; Törmä, E.; Sun, B.; Brandell, D. Copolymers of Trimethylene Carbonate and ε-Caprolactone as Electrolytes for Lithium-Ion Batteries. *Polymer (Guildf).* **2015**, *63*, 91–98. https://doi.org/10.1016/j.polymer.2015.02.052.

(40) Lin, Y.; Li, J.; Lai, Y.; Yuan, C.; Cheng, Y.; Liu, J. A Wider Temperature Range Polymer Electrolyte for All-Solid-State Lithium Ion Batteries. *RSC Adv.* **2013**, *3* (27), 10722–10730. https://doi.org/10.1039/C3RA40306H.

(41) Xue, Z.; He, D.; Xie, X. Poly(Ethylene Oxide)-Based Electrolytes for Lithium-Ion Batteries. *J. Mater. Chem. A* **2015**, *3* (38), 19218–19253. https://doi.org/10.1039/C5TA03471J.

(42) Stephan, A. M. Review on Gel Polymer Electrolytes for Lithium Batteries. *Eur. Polym. J.* **2006**, *42* (1), 21–42. https://doi.org/10.1016/j.eurpolymj.2005.09.017.

(43) Devaux, D.; Bouchet, R.; Glé, D.; Denoyel, R. Mechanism of Ion Transport in PEO/LiTFSI Complexes: Effect of Temperature, Molecular Weight and End Groups. *Solid State Ionics* **2012**, *227*, 119–127. https://doi.org/10.1016/j.ssi.2012.09.020.

(44) Cheng, X.; Pan, J.; Zhao, Y.; Liao, M.; Peng, H. Gel Polymer Electrolytes for Electrochemical Energy Storage. *Adv. Energy Mater.* **2018**, *8* (7), 1–16.

https://doi.org/10.1002/aenm.201702184.

(45) Capuano, F. Composite Polymer Electrolytes. *J. Electrochem. Soc.* **1991**, *138* (7), 1918. https://doi.org/10.1149/1.2085900.

(46) Yap, Y. L.; Cheang, P. L.; You, A. H.; Teo, L. L. Modelling of Temperature Dependence on PEO Electrolyte with Al_2O_3. *Comput. Mater. Sci.* **2015**, *106*, 59–63. https://doi.org/10.1016/j.commatsci.2015.04.045.

(47) Liu, S.; Imanishi, N.; Zhang, T.; Hirano, A.; Takeda, Y.; Yamamoto, O.; Yang, J. Effect of Nano-Silica Filler in Polymer Electrolyte on Li Dendrite Formation in Li/Poly(Ethylene Oxide)-Li$(CF_3SO_2)_2N$/Li. *J. Power Sources* **2010**, *195* (19), 6847–6853. https://doi.org/10.1016/j.jpowsour.2010.04.027.

(48) Xia, S.; Wu, X.; Zhang, Z.; Cui, Y.; Liu, W. Practical Challenges and Future Perspectives of All-Solid-State Lithium-Metal Batteries. *Chem* **2019**, *5* (4), 753–785. https://doi.org/10.1016/j.chempr.2018.11.013.

(49) Bachman, J. C.; Muy, S.; Grimaud, A.; Chang, H.-H.; Pour, N.; Lux, S. F.; Paschos, O.; Maglia, F.; Lupart, S.; Lamp, P.; et al. Inorganic Solid-State Electrolytes for Lithium Batteries: Mechanisms and Properties Governing Ion Conduction. *Chem. Rev.* **2016**, *116* (1), 140–162. https://doi.org/10.1021/acs.chemrev.5b00563.

(50) Zhao, Y.; Wu, C.; Peng, G.; Chen, X.; Yao, X.; Bai, Y.; Wu, F.; Chen, S.; Xu, X. A New Solid Polymer Electrolyte Incorporating $Li_{10}GeP_2S_{12}$ into a Polyethylene Oxide Matrix for All-Solid-State Lithium Batteries. *J. Power Sources* **2016**, *301*, 47–53. https://doi.org/10.1016/j.jpowsour.2015.09.111.

(51) Chen, L.; Li, Y.; Li, S.-P.; Fan, L.-Z.; Nan, C.-W.; Goodenough, J. B. PEO/Garnet Composite Electrolytes for Solid-State Lithium Batteries: From “Ceramic-in-Polymer” to

"Polymer-in-Ceramic." *Nano Energy* **2017**. https://doi.org/10.1016/j.nanoen.2017.12.037.

(52) Mizuno, F.; Hayashi, A.; Tadanaga, K.; Tatsumisago, M. High Lithium Ion Conducting Glass-Ceramics in the System Li_2S-P_2S_5. *Solid State Ionics* **2006**, *177* (26-32 SPEC. ISS.), 2721–2725. https://doi.org/10.1016/j.ssi.2006.04.017.

(53) Tatsumisago, M.; Hayashi, A. Electrolytes : Glass. **2009**, 138–144.

(54) Garcia-Mendez, R.; Mizuno, F.; Zhang, R.; Arthur, T. S.; Sakamoto, J. Effect of Processing Conditions of $75Li_2S$-$25P_2S_5$ Solid Electrolyte on Its DC Electrochemical Behavior. *Electrochim. Acta* **2017**, *237*, 144–151. https://doi.org/10.1016/j.electacta.2017.03.200.

(55) Seino, Y.; Ota, T.; Takada, K.; Hayashi, A.; Tatsumisago, M. A Sulphide Lithium Super Ion Conductor Is Superior to Liquid Ion Conductors for Use in Rechargeable Batteries. *Energy Environ. Sci.* **2014**, *7* (2), 627–631. https://doi.org/10.1039/c3ee41655k.

(56) Kanno, R.; Murayama, M. Lithium Ionic Conductor Thio-LISICON: The Li_2S-GeS_2-P_2S_5 System. *J. Electrochem. Soc.* **2001**, *148* (7), A742. https://doi.org/10.1149/1.1379028.

(57) Zhu, Y.; He, X.; Mo, Y. First Principles Study on Electrochemical and Chemical Stability of Solid Electrolyte–Electrode Interfaces in All-Solid-State Li-Ion Batteries. *J. Mater. Chem. A* **2016**, *4* (9), 3253–3266. https://doi.org/10.1039/C5TA08574H.

(58) Belous, A. G. Study of Complex Oxides with the Composition $La_{2/3-x}Li_{3x}TiO_3$. *Inorg. Mater.* **1987**, *23* (3), 412.

(59) Aono, H.; Sugimoto, E.; Sadaoka, Y.; Imanaka, N.; Adachi, G. ya. Electrical Property and Sinterability of $LiTi_2(PO_4)_3$ Mixed with Lithium Salt (Li_3PO_4 or Li_3BO_3). *Solid State Ionics* **1991**, *47* (3–4), 257–264. https://doi.org/10.1016/0167-2738(91)90247-9.

(60) Mariappan, C. R.; Gellert, M.; Yada, C.; Rosciano, F.; Roling, B. Grain Boundary

Resistance of Fast Lithium Ion Conductors: Comparison between a Lithium-Ion Conductive Li-Al-Ti-P-O-Type Glass Ceramic and a $Li_{1.5}Al_{0.5}Ge_{1.5}P_3O_{12}$ Ceramic. *Electrochem. commun.* **2012**, *14* (1), 25–28. https://doi.org/10.1016/j.elecom.2011.10.022.

(61) Hyooma, H.; Hayashi, K. Crystal Structures of $La_3Li_5M_2O_{12}$ (M=Nb, Ta). *Mater. Res. Bull.* **1988**, *23* (10), 1399–1407. https://doi.org/10.1016/0025-5408(88)90264-4.

(62) Murugan, R.; Thangadurai, V.; Weppner, W. Fast Lithium Ion Conduction in Garnet-Type $Li_7La_3Zr_2O_{12}$. *ChemInform* **2007**, *38* (50). https://doi.org/10.1002/chin.200750009.

(63) Thompson, T.; Wolfenstine, J.; Allen, J. L.; Johannes, M.; Huq, A.; David, I. N.; Sakamoto, J. Tetragonal vs. Cubic Phase Stability in Al – Free Ta Doped $Li_7La_3Zr_2O_{12}$ (LLZO). *J. Mater. Chem. A* **2014**, *2* (33), 13431–13436. https://doi.org/10.1039/C4TA02099E.

(64) Koerver, R.; Aygün, I.; Leichtweiß, T.; Dietrich, C.; Zhang, W.; Binder, J. O.; Hartmann, P.; Zeier, W. G.; Janek, J. Capacity Fade in Solid-State Batteries: Interphase Formation and Chemomechanical Processes in Nickel-Rich Layered Oxide Cathodes and Lithium Thiophosphate Solid Electrolytes. *Chem. Mater.* **2017**, *29* (13), 5574–5582. https://doi.org/10.1021/acs.chemmater.7b00931.

(65) Zhang, W.; Richter, F. H.; Culver, S. P.; Leichtweiss, T.; Lozano, J. G.; Dietrich, C.; Bruce, P. G.; Zeier, W. G.; Janek, J. Degradation Mechanisms at the $Li_{10}GeP_2S_{12}$/LiCoO2 Cathode Interface in an All-Solid-State Lithium-Ion Battery. *ACS Appl. Mater. Interfaces* **2018**, *10* (26), 22226–22236. https://doi.org/10.1021/acsami.8b05132.

(66) Gao, Z.; Sun, H.; Fu, L.; Ye, F.; Zhang, Y.; Luo, W.; Huang, Y. Promises, Challenges, and Recent Progress of Inorganic Solid-State Electrolytes for All-Solid-State Lithium Batteries. *Adv. Mater.* **2018**, *30* (17), 1–27. https://doi.org/10.1002/adma.201705702.

(67) Kim, K. H.; Iriyama, Y.; Yamamoto, K.; Kumazaki, S.; Asaka, T.; Tanabe, K.; Fisher, C. A. J.; Hirayama, T.; Murugan, R.; Ogumi, Z. Characterization of the Interface between $LiCoO_2$ and $Li_7La_3Zr_2O_{12}$ in an All-Solid-State Rechargeable Lithium Battery. *J. Power Sources* **2011**, *196* (2), 764–767. https://doi.org/10.1016/j.jpowsour.2010.07.073.

(68) Park, K.; Yu, B.-C.; Jung, J.-W.; Li, Y.; Zhou, W.; Gao, H.; Son, S.; Goodenough, J. B. Electrochemical Nature of the Cathode Interface for a Solid-State Lithium-Ion Battery: Interface between $LiCoO_2$ and Garnet-$Li_7La_3Zr_2O_{12}$. *Chem. Mater.* **2016**, *28* (21), 8051–8059. https://doi.org/10.1021/acs.chemmater.6b03870.

(69) Miara, L. J.; Richards, W. D.; Wang, Y. E.; Ceder, G. First-Principles Studies on Cation Dopants and Electrolyte|Cathode Interphases for Lithium Garnets. *Chem. Mater.* **2015**, *27* (11), 4040–4047. https://doi.org/10.1021/acs.chemmater.5b01023.

(70) Mukhopadhyay, A.; Sheldon, B. W. Deformation and Stress in Electrode Materials for Li-Ion Batteries. *Prog. Mater. Sci.* **2014**, *63* (February), 58–116. https://doi.org/10.1016/j.pmatsci.2014.02.001.

(71) Koyama, Y.; Chin, T. E.; Rhyner, U.; Holman, R. K.; Hall, S. R.; Chiang, Y.-M. Harnessing the Actuation Potential of Solid-State Intercalation Compounds. *Adv. Funct. Mater.* **2006**, *16* (4), 492–498. https://doi.org/10.1002/adfm.200500633.

(72) Koerver, R.; Zhang, W.; De Biasi, L.; Schweidler, S.; Kondrakov, A. O.; Kolling, S.; Brezesinski, T.; Hartmann, P.; Zeier, W. G.; Janek, J. Chemo-Mechanical Expansion of Lithium Electrode Materials-on the Route to Mechanically Optimized All-Solid-State Batteries. *Energy Environ. Sci.* **2018**, *11* (8), 2142–2158. https://doi.org/10.1039/c8ee00907d.

(73) Kondrakov, A. O.; Schmidt, A.; Xu, J.; Geßwein, H.; Mönig, R.; Hartmann, P.; Sommer,

H.; Brezesinski, T.; Janek, J. Anisotropic Lattice Strain and Mechanical Degradation of High- and Low-Nickel NCM Cathode Materials for Li-Ion Batteries. *J. Phys. Chem. C* **2017**, *121* (6), 3286–3294. https://doi.org/10.1021/acs.jpcc.6b12885.

(74) De Biasi, L.; Kondrakov, A. O.; Geßwein, H.; Brezesinski, T.; Hartmann, P.; Janek, J. Between Scylla and Charybdis: Balancing among Structural Stability and Energy Density of Layered NCM Cathode Materials for Advanced Lithium-Ion Batteries. *J. Phys. Chem. C* **2017**, *121* (47), 26163–26171. https://doi.org/10.1021/acs.jpcc.7b06363.

(75) Mukhopadhyay, A.; Tokranov, A.; Xiao, X.; Sheldon, B. W. Stress Development Due to Surface Processes in Graphite Electrodes for Li-Ion Batteries: A First Report. *Electrochim. Acta* **2012**, *66*, 28–37. https://doi.org/10.1016/j.electacta.2012.01.058.

(76) Tokranov, A.; Sheldon, B. W.; Lu, P.; Xiao, X.; Mukhopadhyay, A. The Origin of Stress in the Solid Electrolyte Interphase on Carbon Electrodes for Li Ion Batteries. *J. Electrochem. Soc.* **2014**, *161* (1), A58–A65. https://doi.org/10.1149/2.009401jes.

(77) Janek, J.; Zeier, W. G. A Solid Future for Battery Development. *Nat. Energy* **2016**, *1* (9), 1–4.

(78) Zhang, W.; Schröder, D.; Arlt, T.; Manke, I.; Koerver, R.; Pinedo, R.; Weber, D. A.; Sann, J.; Zeier, W. G.; Janek, J. (Electro) Chemical Expansion during Cycling: Monitoring the Pressure Changes in Operating Solid-State Lithium Batteries. *J. Mater. Chem. A* **2017**, *5* (20), 9929–9936.

(79) Meethong, N.; Huang, H.-Y. S.; Carter, W. C.; Chiang, Y.-M. Size-Dependent Lithium Miscibility Gap in Nanoscale $Li_{1-x}FePO_4$. *Electrochem. Solid State Lett.* **2007**, *10* (5), A134.

(80) Shearing, P. R. Batteries: Imaging Degradation. *Nat. Energy* **2016**, *1* (11), 1–2.

(81) Sun, G.; Sui, T.; Song, B.; Zheng, H.; Lu, L.; Korsunsky, A. M. On the Fragmentation of Active Material Secondary Particles in Lithium Ion Battery Cathodes Induced by Charge Cycling. *Extrem. Mech. Lett.* **2016**, *9* (March), 449–458. https://doi.org/10.1016/j.eml.2016.03.018.

(82) Kerman, K.; Luntz, A.; Viswanathan, V.; Chiang, Y.-M.; Chen, Z. Review—Practical Challenges Hindering the Development of Solid State Li Ion Batteries. *J. Electrochem. Soc.* **2017**, *164* (7), A1731–A1744. https://doi.org/10.1149/2.1571707jes.

(83) Liu, L.; Qi, X.; Ma, Q.; Rong, X.; Hu, Y.-S.; Zhou, Z.; Li, H.; Huang, X.; Chen, L. Toothpaste-like Electrode: A Novel Approach to Optimize the Interface for Solid-State Sodium-Ion Batteries with Ultralong Cycle Life. *ACS Appl. Mater. Interfaces* **2016**, *8* (48), 32631–32636. https://doi.org/10.1021/acsami.6b11773.

(84) Liu, B.; Gong, Y.; Fu, K.; Han, X.; Yao, Y.; Pastel, G.; Yang, C.; Xie, H.; Wachsman, E. D.; Hu, L. Garnet Solid Electrolyte Protected Li-Metal Batteries. *ACS Appl. Mater. Interfaces* **2017**, *9* (22), 18809–18815. https://doi.org/10.1021/acsami.7b03887.

(85) Langer, F.; Palagonia, M. S.; Bardenhagen, I.; Glenneberg, J.; La Mantia, F.; Kun, R. Impedance Spectroscopy Analysis of the Lithium Ion Transport through the $Li_7La_3Zr_2O_{12}$/$P(EO)_{20}$ Li Interface. *J. Electrochem. Soc.* **2017**, *164* (12), A2298–A2303. https://doi.org/10.1149/2.0381712jes.

(86) Liu, J.; Gao, X.; Hartley, G. O.; Alex, W.; Johnson, L. R.; Bruce, P. G.; Liu, J.; Gao, X.; Hartley, G. O.; Rees, G. J.; et al. The Interface between $Li_{6.5}La_3Zr_{1.5}Ta_{0.5}O_{12}$ and Liquid Electrolyte. 1–8. https://doi.org/10.1016/j.joule.2019.10.001.

(87) Naguib, M.; Sharafi, A.; Self, E. C.; Meyer, H. M.; Sakamoto, J.; Nanda, J. Interfacial Reactions and Performance of $Li_7La_3Zr_2O_{12}$-Stabilized Li-Sulfur Hybrid Cell. *ACS Appl.*

Mater. Interfaces **2019**. https://doi.org/10.1021/acsami.9b11439.

(88) Stolwijk, N. A.; Heddier, C.; Reschke, M.; Wiencierz, M.; Bokeloh, J.; Wilde, G. Salt-Concentration Dependence of the Glass Transition Temperature in PEO-NaI and PEO-LiTFSI Polymer Electrolytes. *Macromolecules* **2013**, *46* (21), 8580–8588. https://doi.org/10.1021/ma401686r.

(89) Rangasamy, E.; Wolfenstine, J.; Sakamoto, J. The Role of Al and Li Concentration on the Formation of Cubic Garnet Solid Electrolyte of Nominal Composition $Li_7La_3Zr_2O_{12}$. *Solid State Ionics* **2012**, *206*, 28–32. https://doi.org/10.1016/j.ssi.2011.10.022.

(90) Sharafi, A.; Yu, S.; Naguib, M.; Lee, M.; Ma, C.; Meyer, H. M.; Nanda, J.; Chi, M.; Siegel, D. J.; Sakamoto, J. Impact of Air Exposure and Surface Chemistry on Li-$Li_7La_3Zr_2O_{12}$ Interfacial Resistance. *J. Mater. Chem. A* **2017**, *5* (26), 13475–13487.

(91) Irvine, J. T. S.; Sinclair, D. C.; West, A. R. Electroceramics: Characterization by Impedance Spectroscopy. *Adv. Mater.* **1990**, *2* (3), 132–138. https://doi.org/10.1002/adma.19900020304.

(92) Tarascon, J. M.; Armand, M. Issues and Challenges Facing Rechargeable Lithium Batteries. *Nature*. 2001. https://doi.org/10.1038/35104644.

(93) Tikekar, M. D.; Choudhury, S.; Tu, Z.; Archer, L. A. Design Principles for Electrolytes and Interfaces for Stable Lithium-Metal Batteries. *Nat. Energy* **2016**, *1* (9), 1–7.

(94) David, I. N.; Thompson, T.; Wolfenstine, J.; Allen, J. L.; Sakamoto, J. Microstructure and Li-Ion Conductivity of Hot-Pressed Cubic $Li_7La_3Zr_2O_{12}$. *J. Am. Ceram. Soc.* **2015**, *98* (4), 1209–1214. https://doi.org/10.1111/jace.13455.

(95) Odian, G. *Principles of Polymerization*; John Wiley & Sons, 2004.

(96) Ferry, J. D. *Viscoelastic Properties of Polymers*; John Wiley & Sons, 1980.

(97) Rey, I.; Lassègues, J. C.; Grondin, J.; Servant, L. Infrared and Raman Study of the PEO-LiTFSI Polymer Electrolyte. *Electrochim. Acta* **1998**, *43* (10–11), 1505–1510. https://doi.org/10.1016/S0013-4686(97)10092-5.

(98) Prosini, P. P.; Passerini, S. A Lithium Battery Electrolyte Based on Gelled Polyethylene Oxide. *Solid State Ionics* **2002**, *146* (1–2), 65–72.

(99) Appetecchi, G. B.; Passerini, S. Poly (Ethylene Oxide)-LiN $(SO_2CF_2CF_3)_2$ Polymer Electrolytes II. Characterization of the Interface with Lithium. *J. Electrochem. Soc.* **2002**, *149* (7), A891--A897.

(100) Bouchet, R.; Lascaud, S.; Rosso, M. An EIS Study of the Anode Li/PEO-LiTFSI of a Li Polymer Battery. *J. Electrochem. Soc.* **2003**, *150* (10), A1385--A1389.

(101) Appetecchi, G. B.; Scaccia, S.; Passerini, S. Investigation on the Stability of the Lithium-Polymer Electrolyte Interface. *J. Electrochem. Soc.* **2000**, *147* (12), 4448–4452.

(102) Croce, F.; Scrosati, B. Interfacial Phenomena in Polymer-Electrolyte Cells: Lithium Passivation and Cycleability. *J. Power Sources* **1993**, *43* (1–3), 9–19.

(103) Marzantowicz, M.; Dygas, J. R.; Krok, F.; Tomaszewska, A.; Żukowska, G. Z.; Florjańczyk, Z.; Zygadło-Monikowska, E. Phase Segregation Phenomena in Poly (Ethylene Oxide): $LiN(CF_3SO_2)_2$ Electrolyte Studied by Local Raman Spectroscopy. *Electrochim. Acta* **2010**, *55* (19), 5446–5452.

(104) Marzantowicz, M.; Dygas, J. R.; Krok, F. Impedance of Interface between PEO: LiTFSI Polymer Electrolyte and Blocking Electrodes. *Electrochim. Acta* **2008**, *53* (25), 7417–7425.

(105) Caruso, T.; Capoleoni, S.; Cazzanelli, E.; Agostino, R. G.; Villano, P.; Passerini, S. Characterization of PEO-Lithium Triflate Polymer Electrolytes: Conductivity, DSC and

Raman Investigations. *Ionics (Kiel).* **2002**, *8* (1–2), 36–43.

(106) Brissot, C.; Rosso, M.; Chazalviel, J. N.; Lascaud, S. Dendritic Growth Mechanisms in Lithium/Polymer Cells. *J. Power Sources* **1999**, *81*, 925–929. https://doi.org/10.1016/S0378-7753(98)00242-0.

(107) Rosso, M.; Brissot, C.; Teyssot, A.; Dollé, M.; Sannier, L.; Tarascon, J. M.; Bouchet, R.; Lascaud, S. Dendrite Short-Circuit and Fuse Effect on Li/Polymer/Li Cells. *Electrochim. Acta* **2006**, *51* (25), 5334–5340. https://doi.org/10.1016/j.electacta.2006.02.004.

(108) Wang, M.; Sakamoto, J. Correlating the Interface Resistance and Surface Adhesion of the Li Metal-Solid Electrolyte Interface. *J. Power Sources* **2018**, *377* (November 2017), 7–11. https://doi.org/https://doi.org/10.1016/j.jpowsour.2017.11.078.

(109) Yu, S.; Schmidt, R. D.; Garcia-Mendez, R.; Herbert, E.; Dudney, N. J.; Wolfenstine, J. B.; Sakamoto, J.; Siegel, D. J. Elastic Properties of the Solid Electrolyte $Li_7La_3Zr_2O_{12}$ (LLZO). *Chem. Mater.* **2016**, *28* (1), 197–206.

(110) Kelly, T.; Ghadi, B. M.; Berg, S.; Ardebili, H. In Situ Study of Strain-Dependent Ion Conductivity of Stretchable Polyethylene Oxide Electrolyte. *Sci. Rep.* **2016**, *6* (1), 1–9.

(111) Sharafi, A.; Meyer, H. M.; Nanda, J.; Wolfenstine, J.; Sakamoto, J. Characterizing the Li-$Li_7La_3Zr_2O_{12}$ Interface Stability and Kinetics as a Function of Temperature and Current Density. *J. Power Sources* **2016**, *302*, 135–139. https://doi.org/10.1016/j.jpowsour.2015.10.053.

(112) Monroe, C.; Newman, J. The Impact of Elastic Deformation on Deposition Kinetics at Lithium/Polymer Interfaces. *J. Electrochem. Soc.* **2005**, *152* (2), A396--A404.

(113) Samsonov, G. V. *Handbook of the Physicochemical Properties of the Elements*; Springer Science & Business Media, 2012.

(114) Marzantowicz, M.; Dygas, J. R.; Krok, F.; Nowiński, J. L.; Tomaszewska, A.; Florjańczyk, Z.; Zygadło-Monikowska, E. Crystalline Phases, Morphology and Conductivity of PEO:LiTFSI Electrolytes in the Eutectic Region. *J. Power Sources* **2006**, *159* (1 SPEC. ISS.), 420–430. https://doi.org/10.1016/j.jpowsour.2006.02.044.

(115) Appetecchi, G. B.; Passerini, S. PEO-Carbon Composite Lithium Polymer Electrolyte. *Electrochim. Acta* **2000**, *45* (13), 2139–2145.

(116) Wang, M.; Wolfenstine, J. B.; Sakamoto, J. Temperature Dependent Flux Balance of the Li/$Li_7La_3Zr_2O_{12}$ Interface. *Electrochim. Acta* **2019**, *296*, 842–847. https://doi.org/10.1016/j.electacta.2018.11.034.

(117) Wood, K. N.; Kazyak, E.; Chadwick, A. F.; Chen, K.-H.; Zhang, J.-G.; Thornton, K.; Dasgupta, N. P. Dendrites and Pits: Untangling the Complex Behavior of Lithium Metal Anodes through Operando Video Microscopy. *ACS Cent. Sci.* **2016**, *2* (11), 790–801.

(118) Etacheri, V.; Marom, R.; Elazari, R.; Salitra, G.; Aurbach, D. Challenges in the Development of Advanced Li-Ion Batteries: A Review. *Energy and Environmental Science*. 2011. https://doi.org/10.1039/c1ee01598b.

(119) Schmedt auf der Günne, J.; Johansson, S.; Dehnen, S.; Bron, P.; Roling, B.; Zick, K. $Li_{10}SnP_2S_{12}$: An Affordable Lithium Superionic Conductor . *J. Am. Chem. Soc.* **2013**, *135* (42), 15694–15697. https://doi.org/10.1021/ja407393y.

(120) Kamaya, N.; Homma, K.; Yamakawa, Y.; Hirayama, M.; Kanno, R.; Yonemura, M.; Kamiyama, T.; Kato, Y.; Hama, S.; Kawamoto, K.; et al. A Lithium Superionic Conductor. *Nat. Mater.* **2011**, *10* (9), 682–686. https://doi.org/10.1038/nmat3066.

(121) Aono, H.; Sugimoto, E.; Sadaaka, Y.; Imanaka, N.; Adachi, G. Y. Ionic Conductivity of the Lithium Titanium Phosphate ($Li_{1+x}M_xTi_{2-x}(PO_4)_3$, M= Al, Sc, Y, and La) Systems. *J.*

Electrochem. Soc. **1989**, *136* (2), 590.

(122) Hallinan Jr, D. T.; Balsara, N. P. Polymer Electrolytes. *Annu. Rev. Mater. Res.* **2013**, *43*, 503–525.

(123) Long, L.; Wang, S.; Xiao, M.; Meng, Y. Polymer Electrolytes for Lithium Polymer Batteries. *J. Mater. Chem. A* **2016**, *4* (26), 10038–10069.

(124) Chen, F.; Yang, D.; Zha, W.; Zhu, B.; Zhang, Y.; Li, J.; Gu, Y.; Shen, Q.; Zhang, L.; Sadoway, D. R. Solid Polymer Electrolytes Incorporating Cubic $Li_7La_3Zr_2O_{12}$ for All-Solid-State Lithium Rechargeable Batteries. *Electrochim. Acta* **2017**, *258*, 1106–1114. https://doi.org/10.1016/j.electacta.2017.11.164.

(125) Chen, L.; Li, Y.; Li, S. P.; Fan, L. Z.; Nan, C. W.; Goodenough, J. B. PEO/Garnet Composite Electrolytes for Solid-State Lithium Batteries: From "Ceramic-in-Polymer" to "Polymer-in-Ceramic." *Nano Energy* **2018**, *46* (December 2017), 176–184. https://doi.org/10.1016/j.nanoen.2017.12.037.

(126) Keller, M.; Appetecchi, G. B.; Kim, G. T.; Sharova, V.; Schneider, M.; Schuhmacher, J.; Roters, A.; Passerini, S. Electrochemical Performance of a Solvent-Free Hybrid Ceramic-Polymer Electrolyte Based on $Li_7La_3Zr_2O_{12}$ in $P(EO)_{15}LiTFSI$. *J. Power Sources* **2017**, *353*, 287–297. https://doi.org/10.1016/j.jpowsour.2017.04.014.

(127) Tao, X.; Liu, Y.; Liu, W.; Zhou, G.; Zhao, J.; Lin, D.; Zu, C.; Sheng, O.; Zhang, W.; Lee, H. W.; et al. Solid-State Lithium-Sulfur Batteries Operated at 37 °C with Composites of Nanostructured $Li_7La_3Zr_2O_{12}$/Carbon Foam and Polymer. *Nano Lett.* **2017**, *17* (5), 2967–2972. https://doi.org/10.1021/acs.nanolett.7b00221.

(128) Karthik, K.; Murugan, R. Lithium Garnet Based Free-Standing Solid Polymer Composite Membrane for Rechargeable Lithium Battery. *J. Solid State Electrochem.* **2018**, *22* (10),

2989–2998. https://doi.org/10.1007/s10008-018-4010-3.

(129) Langer, F.; Bardenhagen, I.; Glenneberg, J.; Kun, R. Microstructure and Temperature Dependent Lithium Ion Transport of Ceramic – Polymer Composite Electrolyte for Solid-State Lithium Ion Batteries Based on Garnet-Type $Li_7La_3Zr_2O_{12}$. *Solid State Ionics* **2016**, *291*, 8–13. https://doi.org/10.1016/j.ssi.2016.04.014.

(130) Choi, J. H.; Lee, C. H.; Yu, J. H.; Doh, C. H.; Lee, S. M. Enhancement of Ionic Conductivity of Composite Membranes for All-Solid-State Lithium Rechargeable Batteries Incorporating Tetragonal $Li_7La_3Zr_2O_{12}$ into a Polyethylene Oxide Matrix. *J. Power Sources* **2015**, *274*, 458–463. https://doi.org/10.1016/j.jpowsour.2014.10.078.

(131) Kalnaus, S.; Tenhaeff, W. E.; Sakamoto, J.; Sabau, A. S.; Daniel, C.; Dudney, N. J. Analysis of Composite Electrolytes with Sintered Reinforcement Structure for Energy Storage Applications. *J. Power Sources* **2013**, *241*, 178–185.

(132) Abe, T.; Ohtsuka, M.; Sagane, F.; Iriyama, Y.; Ogumi, Z. Lithium Ion Transfer at the Interface between Lithium-Ion-Conductive Solid Crystalline Electrolyte and Polymer Electrolyte. **2004**, 1950–1953. https://doi.org/10.1149/1.1804813.

(133) Tenhaeff, W. E.; Perry, K. A.; Dudney, N. J. Impedance Characterization of Li Ion Transport at the Interface between Laminated Ceramic and Polymeric Electrolytes. *J. Electrochem. Soc.* **2012**, *159* (12), A2118–A2123. https://doi.org/10.1149/2.063212jes.

(134) Li, Y.; Chen, X.; Dolocan, A.; Cui, Z.; Xin, S.; Xu, H.; Park, K.; Goodenough, J. B.; Li, Y.; Chen, X.; et al. Garnet Electrolyte with an Ultra-Low Interfacial Resistance for Li-Metal Batteries Garnet Electrolyte with an Ultra-Low Interfacial Resistance for Li- Metal Batteries. **2018**. https://doi.org/10.1021/jacs.8b03106.

(135) Borodin, O.; Smith, G. D.; Bandyopadhyaya, R.; Byutner, O. Molecular Dynamics Study

of the Influence of Solid Interfaces on Poly (Ethylene Oxide) Structure and Dynamics. *Macromolecules* **2003**, *36* (20), 7873–7883.

(136) Wakihara, M.; Yamamoto, O. *Lithium Ion Batteries: Fundamentals and Performance*; John Wiley & Sons, 2008.

(137) Busche, M. R.; Drossel, T.; Leichtweiss, T.; Weber, D. A.; Falk, M.; Schneider, M.; Reich, M. L.; Sommer, H.; Adelhelm, P.; Janek, J. Dynamic Formation of a Solid-Liquid Electrolyte Interphase and Its Consequences for Hybrid-Battery Concepts. *Nat. Chem.* **2016**, *8* (5), 426–434. https://doi.org/10.1038/nchem.2470.

(138) Xu, B.; Duan, H.; Liu, H.; Wang, C. A.; Zhong, S. Stabilization of Garnet/Liquid Electrolyte Interface Using Superbase Additives for Hybrid Li Batteries. *ACS Appl. Mater. Interfaces* **2017**, *9* (25), 21077–21082. https://doi.org/10.1021/acsami.7b05599.

(139) Abe, T.; Sagane, F.; Ohtsuka, M.; Iriyama, Y.; Ogumi, Z. Lithium-Ion Transfer at the Interface between Lithium-Ion Conductive Ceramic Electrolyte and Liquid Electrolyte-a Key to Enhancing the Rate Capability of Lithium-Ion Batteries. *J. Electrochem. Soc.* **2005**, *152* (11), 2151–2154. https://doi.org/10.1149/1.2042907.

(140) Schleutker, M.; Bahner, J.; Tsai, C. L.; Stolten, D.; Korte, C. On the Interfacial Charge Transfer between Solid and Liquid Li+ Electrolytes. *Phys. Chem. Chem. Phys.* **2017**, *19* (39), 26596–26605. https://doi.org/10.1039/c7cp05213h.

(141) Gupta, A.; Sakamoto, J. Controlling Ionic Transport through the PEO-LITFSi/LLZTO Interface. *Electrochem. Soc. Interface* **2019**, *28* (2), 63–69. https://doi.org/10.1149/2.F06192if.

(142) Xie, J.; Liao, L.; Gong, Y.; Li, Y.; Shi, F.; Pei, A.; Sun, J.; Zhang, R.; Kong, B.; Subbaraman, R.; et al. Stitching H-BN by Atomic Layer Deposition of LiF as a Stable

Interface for Lithium Metal Anode. *Sci. Adv.* **2017**, *3* (11), 1–9. https://doi.org/10.1126/sciadv.aao3170.

(143) Chen, Y. T.; Jena, A.; Pang, W. K.; Peterson, V. K.; Sheu, H. S.; Chang, H.; Liu, R. S. Voltammetric Enhancement of Li-Ion Conduction in Al-Doped $Li_{7-x}La_3Zr_2O_{12}$ Solid Electrolyte. *J. Phys. Chem. C* **2017**, *121* (29), 15565–15573. https://doi.org/10.1021/acs.jpcc.7b04004.

(144) De Marco, R.; Hauser, P. C.; Cattrall, R. W.; Liesegang, J.; Nyberg, G. L.; Hamilton, I. C. XPS Studies of the Fluoride Ion-selective Electrode Membrane LaF_3: Evidence for a Gel Layer on the Surface. *Surf. Interface Anal.* **1989**, *14* (8), 463–468. https://doi.org/10.1002/sia.740140807.

(145) Gutmann, V. Solvent Effects on the Reactivities of Organometallic Compounds. *Coord. Chem. Rev.* **1976**, *18* (2), 225–255. https://doi.org/10.1016/S0010-8545(00)82045-7.

(146) Xin, N.; Sun, Y.; He, M.; Radke, C. J.; Prausnitz, J. M. Solubilities of Six Lithium Salts in Five Non-Aqueous Solvents and in a Few of Their Binary Mixtures. *Fluid Phase Equilib.* **2018**, *461*, 1–7. https://doi.org/10.1016/j.fluid.2017.12.034.

(147) Chen, F.; Hu, J.; Chen, Z.; Yang, Z.; Gu, N. Determination and Correlation of Solubilities of Lithium Bis(Oxalate)Borate in Six Different Solvents from (293.15 to 363.15) K. *J. Chem. Eng. Data* **2014**, *59* (5), 1614–1618. https://doi.org/10.1021/je500068b.

(148) Ren, X.; Chen, S.; Lee, H.; Mei, D.; Engelhard, M. H.; Burton, S. D.; Zhao, W.; Zheng, J.; Li, Q.; Ding, M. S.; et al. Localized High-Concentration Sulfone Electrolytes for High-Efficiency Lithium-Metal Batteries. *Chem* **2018**, *4* (8), 1877–1892. https://doi.org/10.1016/j.chempr.2018.05.002.

(149) Yamada, Y.; Furukawa, K.; Sodeyama, K.; Kikuchi, K.; Yaegashi, M.; Tateyama, Y.;

Yamada, A. Unusual Stability of Acetonitrile-Based Superconcentrated Electrolytes for Fast-Charging Lithium-Ion Batteries. *J. Am. Chem. Soc.* **2014**, *136* (13), 5039–5046. https://doi.org/10.1021/ja412807w.

(150) Lundgren, H.; Scheers, J.; Behm, M.; Lindbergh, G. Characterization of the Mass-Transport Phenomena in a Superconcentrated LiTFSI: Acetonitrile Electrolyte. *J. Electrochem. Soc.* **2015**, *162* (7), A1334–A1340. https://doi.org/10.1149/2.0961507jes.

(151) Hamill, J. C.; Schwartz, J.; Loo, Y. L. Influence of Solvent Coordination on Hybrid Organic-Inorganic Perovskite Formation. *ACS Energy Lett.* **2018**, *3* (1), 92–97. https://doi.org/10.1021/acsenergylett.7b01057.

(152) Langer, F.; Palagonia, S.; Bardenhagen, I.; Glenneberg, J.; Mantia, F. La; Kun, R. Impedance Spectroscopy Analysis of the Lithium Ion Transport through the $Li_7La_3Zr_2O_{12}$/$P(EO)_{20}$ Li Interface. **2017**, *164* (12), 2298–2303. https://doi.org/10.1149/2.0381712jes.

(153) Doriano Brogioli, Frederieke Langer, Robert Kun, and F. L. M. Space-Charge Effects at the LLZO / PEO Interface. **2019**. https://doi.org/10.1021/acsami.8b19237.